Design and Construction of an Injector for an Electron/Positron Linac Optimized for Positron Yield and Minimal Particle Loss

Dissertation

zur Erlangung des Doktorgrades
des Fachbereichs Physik
der Universität Hamburg

vorgelegt von

Clemens Liebig

aus Worms

Hamburg
2014

Gutachter der Dissertation:	Prof. Dr. Jörg Roßbach Dr. Markus Hüning
Gutachter der Disputation:	Prof. Dr. Jörg Roßbach Prof. Dr. Eckhard Elsen
Datum der Disputation:	28.10.2014
Vorsitzender des Prüfungsausschusses:	Dr. Georg Steinbrück
Vorsitzende des Promotionsausschusses:	Prof. Dr. Daniela Pfannkuche
Leiter des Fachbereichs Physik:	Prof. Dr. Peter Hauschildt
Dekan der MIN Fakultät:	Prof. Dr. Heinrich Graener

Abstract

The Linac II is the first part of the accelerator chain supplying PETRA III. Since the start of PETRA III operation, highest reliability is demanded and several updates are required. Part of these is the new injection system. Beam loss at high energies and the associated activation have to be avoided. At energies above 80 MeV particle loss of 20% occurred. Additionally, an alternative to the old gun, operating in an oil bath and for which cathode preparation is not available, is required. The new system will be commissioned while the old bombarder gun injector is kept for redundancy. In order to obtain the space for joining the beam lines of both electron sources, one accelerator section must be removed. Electron pulses of 6 A beam current and 2 to 30 ns length are provided by the new injection system. The gun uses a thermionic cathode, 100 kV voltage for acceleration and is built as a triode. Longitudinal focusing is performed by a prebuncher and a hybrid buncher structure, both operating at 3 GHz. The buncher is a traveling wave structure to which a short cell has been added, operated in π mode with a standing wave. That way, better electron capture is achieved. A magnetic chicane serves for energy filtering.
The design of the injection system, as well as the old injector, have been optimized in simulations and transmission in the linac has been compared. Possible reasons for beam loss are beam loading and misaligned components. For the bombarder gun particle tracking, a loss of 1% at high energies was observed due to beam loading. The additional beam optics and steering options in the beam line allow for compensation of the misalignment of preceding and succeeding components.
The complete new injection system has been operated in a test stand and has undergone extensive tests. After successive enhancement of technically critical components, reliable operation was possible. Investigations of the electron capture and bunching procedure have been carried out by energy measurements in the magnetic chicane. For beam optics measurements, quadrupole scans for different rf settings were executed. Beam loading compensation showed promising results. Bunched beam of up to 3.5 A was transmitted through the buncher structure and 2.6 A through the energy filter to the terminating Faraday cup. The tests revealed an insufficiently focused beam with a beam size of up to 13 mm directly behind the buncher structure. This necessitates a better cooled buncher's solenoid coil in order to achieve a higher magnetic field.
For those reasons, the new injection system is going to replace the second section of the main linac instead of the first. In this manner, the second buncher structure is not needed for the bombarder gun injector and thus its performance is not risked. Since March 2014 the Linac II has been shut down and the installation of the new injection system and commissioning as electron source for the injector complex for PETRA III is ongoing.

Kurzfassung

Der Linac II ist Teil der PETRA III speisenden Beschleunigerkette. Seit PETRA III in Betrieb ist wird höchste Zuverlässigkeit erwartet, was mehrere Umbauten bedingt. Teil der Umbauten ist das neue Injektionssystem. Strahlverluste bei hohen Energien, die zu Aktivierung führen, sollen vermieden werden. Bei Energien von über 80 MeV betrugen diese 20%. Zudem wird eine Alternative zur bestehenden Bombardergun benötigt, die in einem Ölbad betrieben wird, und für die die Kathodenaufbereitung fehlt. Sie wird zwecks Redundanz beibehalten, während die neue Gun sich in der Erprobung befindet. Zur Aufstellung des neuen Injektors und der Zusammenführung mit dem alten System muss ein Beschleunigerabschnitt entfernt werden. Die neue Gun liefert Elektronenpulse von 2 bis 30 ns Länge bei 6 A Strahlstrom. Sie nutzt eine thermionische Kathode, beschleunigt mit 100 kV Hochspannung und ist als Triode aufgebaut. Ein Prebuncher und die Hybridbuncherstruktur prägen dem Strahl seine 3 GHz Struktur auf. Der Buncher ist als Wanderwellenstruktur aufgebaut, an die eine kurze Zelle gekoppelt ist. Diese wird in der π Mode mit einer stehenden Welle betrieben. Dadurch ist ein besserer Elektroneneinfang möglich. Eine magnetische Schikane dient als Energiefilter.

Das neue sowie das alte Injektordesign wurden in Simulationen optimiert und die Transmission durch den Linac verglichen. Als Ursachen für die Strahlverluste wurden Beamloading und Fehljustage ausgemacht. Im Fall der Berechnung für die Bombardergun ergaben sich 1% Verluste bei hohen Energien. Die Justagefehler werden durch Steuerspulen und neue Optionen in der Strahloptik besser kompensiert.

Das neue Injektionssystem wurde in einem Teststand aufgebaut und untersucht. Nach Optimierung anfälliger Komponenten konnte stabiler Strahlbetrieb erreicht werden. Der Bunchingprozess und der Elektroneneinfang wurden durch Energiemessungen in der magnetischen Schikane untersucht. Zur Vermessung der Strahloptik wurden Quadrupolscans bei verschiedenen HF-Einstellungen durchgeführt. Versuche, Beamloading zu kompensieren, zeigten vielversprechende Ergebnisse. Gebunchter Strahl von 3,5 A wurde durch den Buncher geleitet und 2,6 A durch den Energiefilter zum abschließenden Faraday Cup. Die Tests offenbarten die ungenügende Fokussierung des Strahls mit einer Strahlgröße von bis zu 13 mm direkt hinter der Buncherstruktur. Sie erfordert eine neue Solenoidspule mit verbesserter Kühlung, um höhere Magnetfeldstärken zu erreichen.

Daher wird das neue Injektionssystem statt des ersten den zweiten Beschleunigerabschnitt ersetzen. Somit wird die Bombardergun nicht mit der zweiten Buncherstruktur verwendet und ihre Performance wird nicht riskiert. Seit März 2014 befindet sich der Linac II in der Wartungsphase, in der der neue Injektor als Quelle des Injektorkomplexes für PETRA III in Betrieb genommen wird.

Contents

Chapter 1

Introduction

Charged particles which are deflected by magnetic fields emit photons. In case of high particle current, high kinetic energy and low emittance, highly brilliant X-rays can be generated. These are of great importance for a wide range of X-ray diffraction experiments. Since such radiation was first used as a side product of synchrotrons, it is called synchrotron radiation. With the emergence of synchrotron facilities built in the 1950s for nuclear and particle physics experiments, the opportunity for experiments using synchrotron radiation for diffraction arose. Synchrotron radiation causes the loss of a fraction of the kinetic energy, which has to be returned to the particle. Thereby limiting the maximum energy, it was actually undesired. Nowadays, electron storage rings are designed for the specific purpose of generating highly brilliant X-rays, using undulators instead of simple bending magnets for a maximized number of experimental hutches operated simultaneously. PETRA III (Positron Elektron Tandem Ring Anlage), presently the most brilliant storage ring light source in the world, was commissioned in 2010 at DESY (Deutsches Elektronen-Synchrotron).

Except for periods of maintenance and machine study, which are kept to a minimum, the light source operates on a 24 hour basis. Often there are external groups, whose time to carry out a carefully prepared experiment is strictly limited by the operation schedule. Unscheduled downtime can endanger the success of these experiments and ruin the costly preparations. Therefore, it is in the best interest of the PETRA III users to guarantee the highest possible reliability of the X-ray light source and lowest possible likelihood of technical failures.

Being the first part of the accelerator chain which supplies the storage ring, the highest reliability is expected of the Linac II as well. Since PETRA III is operated in top-up mode, even short interruptions of beam delivery cause a reduction of its performance. When the Linac II was commissioned in 1969, other requirements were prioritized until the start of planning for redesigning the former PETRA II ring as a light source for user operation. In order to reduce time for maintenance in future

operation, replacement of fragile components and a set of modifications have been made or are planned. One of these modifications is the new injection system.

For PETRA III operation with electrons and positrons is possible, while DORIS (Doppel Ring Speicher) had to be operated with positrons. Since its final shutdown on January 2nd, 2013 both types of particles can be considered for operation. In order to generate enough positrons at the electron positron converter of the Linac II, a high electron beam power with up to 2 A peak beam current, 20 ns pulse length and 400 MeV energy was necessary. If operation with electrons is requested, which has been successfully tested in 2013, far lower beam current in the Linac II is sufficient.

One requirement for the triode gun of the new injection system was to achieve a beam current as high as the 6 A of the old bombarder gun in order to not lose the option of operation with positrons. A different performance of PETRA III with the other type of particles could not be excluded and DESY will stay attractive as a facility for future experiments needing positrons with an operable positron source available. The new injection system should not limit the performance while operating with positrons. Additionally, a robust and low-maintenance system was desired. The beam loss of approximately 50% from injection to converter should be reduced, particularly at high energies in front of the converter to avoid needless activation. A reasonable degree of beam diagnostics were to be integrated. For operation tests and analysis of its properties, the new injection system was completely installed in a test stand in the Linac II tunnel and operated for several months.

This thesis describes its design process and its components as well as simulations, commissioning, test results and conclusions, divided into seven chapters. Following this introduction, chapter 2 introduces the principles of electron and positron generation and acceleration in particle accelerators. Furthermore, it gives an overview of the accelerator chain at DESY which consists of the Linac II, the positron intensity accumulator PIA, DESY II and PETRA III. The radio frequency (rf) system of the Linac II and its functionality with the SLAC energy doubler (SLED) rf pulse compression is described in detail and its importance for beam loading compensation attempts is discussed. Additionally, the electron positron converter and diagnostics of the Linac II are presented. The third chapter explains the design process and functionality of the new injection system and how all requirements were considered. The physics and technical aspects of its components and infrastructure are also presented. The previously discussed rf pulse usage is transferred for application at the new buncher structure. Necessary relations for beam optics in the new injection system are explained as well. Simulations of the old bombarder gun injection system and the new triode gun injection system are discussed in chapter 4. The simulations include the Linac II primary linac, the electron positron converter and the secondary (positron) linac. The influence of beam loading on the transmission in the linac sections at high energies is discussed for both injection systems.

Chapter 5 explains the commissioning of the new injection system test stand and

its components. It focuses on the tuning process of the buncher structures and the commissioning of the thermionic triode gun. Chapter 6 analyzes the beam properties of the new triode gun injection system that were investigated in the test stand. Efficiency of bunching and electron capture using the prebuncher and the buncher structure is investigated by energy measurements in the magnetic chicane. For beam optics measurements, quadrupole scans for different rf settings were executed. A comparison to expectation from simulations is also given for both types of tests. Chapter 7 summarizes the results and concludes with an outlook about the modification of the Linac II in the shutdown. It includes the modifications of the original plan, to replace accelerator section #2 instead of section #1 with the new injection system, which was derived from test operation.

Chapter 2

The injector complex and the following accelerator chain

The Linac II is part of the injector complex which supplies DESY II with electrons or positrons of 450 MeV energy. It was constructed and commissioned from 1969 by the company Varian, as described in [1]. Firstly, electron pulses are generated and accelerated in the primary linac. The pulse length can be changed between 2 ns and 30 ns at a repetition rate of 50 Hz and 6 A peak beam current. They are accelerated electrostatically to 150 keV and longitudinally focused using the prebuncher, a resonator operating at 2.998 GHz. The acceleration to 400 MeV follows in the five S-band traveling wave structures of 5.2 m length. For transversal focusing solenoid fields are used along the first three sections of the primary linac. The electron positron converter is located behind the fifth accelerator structure. It consists of a 7 mm thick tungsten target and is followed by a pulsed solenoid with a magnetic field of 1.8 T for capture of the positrons, which are scattered in wide angles. Acceleration behind the converter continues with seven further accelerator sections in order to reach the energy of 450 MeV$\pm$ 0.5%, which is required for injection into PIA. For operation with electrons the beam is steered through an aperture in the converter target using bending magnets. Due to the low conversion rate for positrons the maximum beam current of 6 A and the high pulse length of 30 ns are only necessary when positrons are needed, while for operation with electrons usually far smaller total pulse charge is sufficient. This is due to the high divergence and energy spread of the generated positron beam and the associated particle loss.

PIA was commissioned in 1979 and serves for accumulation, damping and compression of the particle pulses [2, 3]. It is the smallest storage ring at DESY with a circumference of 28.8 m. For compression and compensation of energy loss of 3.5 keV due to synchrotron radiation, a first harmonic cavity at 10.4 MHz is used. A 12th harmonic cavity (125 MHz) is used for further compression which suffices the injec-

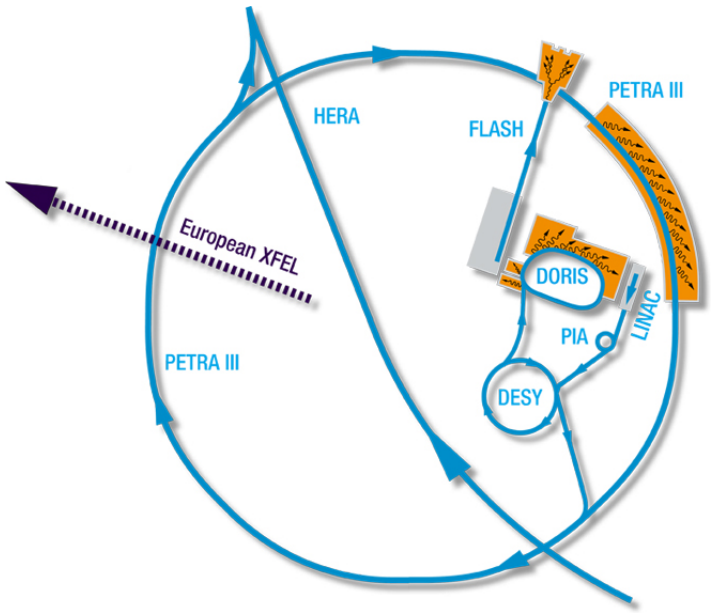

Figure 2.1: Overview of the accelerators operated at DESY [6].

tion into the 500 MHz buckets of the DESY II synchrotron. Recent analysis of beam properties and development of diagnostics in PIA are presented in [4, 5].
An overview of the accelerators operated at DESY is shown in figure 2.1. After acceleration to 6 GeV the electrons are injected into PETRA III, a storage ring of 2304 m circumference, which was originally commissioned in 1978. Later it was used as preaccelerator for HERA (Hadron Elektron Ring Anlage) and after the shutdown of HERA, modified into the presently most brilliant storage ring light source in the world [7, 8] by rebuilding a 300 m long section of the ring, including an experimental hall with 14 undulators and photon beam lines for experiments.

2.1 Synchrotron radiation as an application for electron accelerators

For generation of synchrotron radiation, the fact that any accelerated charge emits photons, is exploited. Because of the dependence of the average power of the emitted radiation on the mass of the particle, heavier particles as for example protons are not practical for operation of light sources and electrons, or, less frequently, positrons are used. The following gives a short overview of how synchrotron radiation parameters are affected by the beam properties and is explained in detail in [9, 10]. In the case of relativistic particles this radiation is approximately uniformly distributed in a frame moving with the speed of the electron $\mathbf{v} = \beta\mathbf{c}$, where $\mathbf{c}$ is the speed of light. Going to the laboratory frame by applying a Lorentz transformation, the radiation

is emitted in the direction of the electron motion with an opening angle $1/\gamma$. The Lorentz factor is given by

$$\gamma = \frac{E}{m_0 c^2}, \tag{2.1}$$

where E is the total energy and m_0 the rest mass of the particle. This angle becomes very small for the ultra-relativistic particles in circular accelerators with $\gamma \gg 1$. In case of a radial acceleration on a circular orbit such as a storage ring with radius R, the power of radiation emitted by a particle of charge e is

$$P_s = \frac{e^2 c}{6\pi\epsilon_0} \frac{1}{(m_0 c^2)^4} \frac{E^4}{R^2}. \tag{2.2}$$

Assuming a circular orbit due to a homogeneous dipole field in the whole ring, this yields by integration over the time for one turn an energy loss per turn of

$$\Delta E = \frac{e^2}{3\epsilon_0 (m_0 c^2)^4} \frac{E^4}{R}. \tag{2.3}$$

The dependency on m_0 shows that energy loss due to synchrotron radiation is irrelevant for proton accelerators, while it strictly limits the maximum energy for electrons in circular machines of reasonable size. In a storage ring light source whose only purpose is generation of X-rays for user operation, undulators are used in addition to bending magnets. An undulator is an insertion device which is commonly used as a source of highly brilliant X-rays. It consists of spatially periodic magnetic fields with periodic length λ_u and forces the particle on a sinusoidal orbit. The maximum intensity of the emitted light lies at the frequency where the emissions of the individual undulator periods are in phase at

$$\omega = \frac{4\pi c \gamma^2}{\lambda_u (1 + \gamma^2 \theta^2)} \tag{2.4}$$

where θ is the maximum deflection angle compared to the injection orbit. It is composed of the harmonics as well. The reduction of particle momentum by synchrotron radiation is also utilized in the injector complex for damping in PIA. That way emittance reduction is achieved for the positron beam. The loss of energy by synchrotron radiation while positrons are deflected is compensated by the rf system, adding momentum only longitudinally. Since this does not happen in transverse direction, the transverse emittance is reduced.

2.2 Linac II

Figure 2.2 shows an overview of the Linac II from gun to PIA. The Linac II is required as an electron and positron source for the PETRA III light source. The

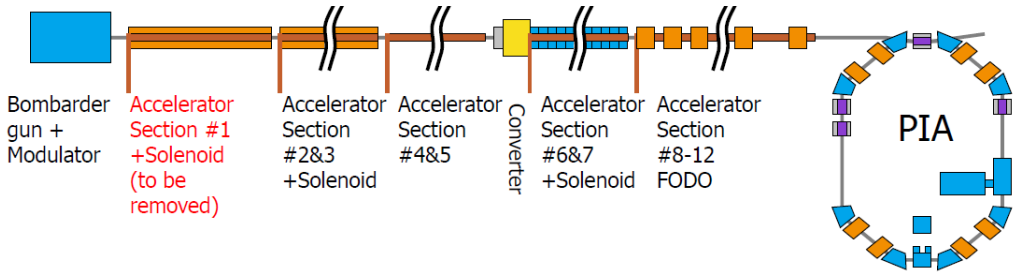

Figure 2.2: Overview of the injector complex, consisting of the primary Linac II, the converter, the secondary Linac II and PIA [11].

electron pulses with a length of 3 μs are generated by the bombarder gun, which accelerates electrostatically to 150 keV. The high voltage applied at the chopper, consisting of two plates and a collimator, cuts out pulses of 2 ns to 30 ns length. A series of seven short solenoid coils serves for transversal focusing between gun and first accelerator section. The 2.998 GHz structure of the beam, preparing it for acceleration in the linac sections, originates from energy modulation by a prebuncher cavity. Afterwards the electrons are accelerated to up to 400 MeV in the five S-band traveling wave structures (TWS) of 5.2 m length each, the first three of which are enclosed by 0.08 T solenoids for focusing.

2.2.1 Electron pulse generation

The simplest way of electron beam generation is the thermionic cathode. It is heated to a temperature where sufficient electrons gain thermal energy such that they overcome the binding potential. The thermally emitted electrons at the cathode's surface are then accelerated by HV potential. The advantages of thermionic cathodes are their simplicity, robustness, long lifetime and high average current. The same method is used in tubes and klystrons. The gun's anode with a hole in the center for the exiting electron beam lies on ground potential, the cathode and the necessary devices for heating are on negative HV potential. The electrons are accelerated by the HV potential from the cathode surface and leave the gun through the hole in the anode.
In case of the bombarder gun a beam current of 6 A is generated by a 150 kV gun whose tungsten cathode is heated via electron bombardment from the rear side to 1600°C. The 400 mA beam for bombardment is accelerated by a voltage of 3 kV. Beam pulses of 3 μs are generated. The high and low potential side of the gun are designed so that no sparcs occur and are separated by an isolating ceramic. Because of dielectric strength and for heat extraction purposes the gun is operated in an oil bath. It is separated from the beam vacuum only by the ceramic, even though its rupture and the consequent oil in the vacuum system can lead to irreparable damage

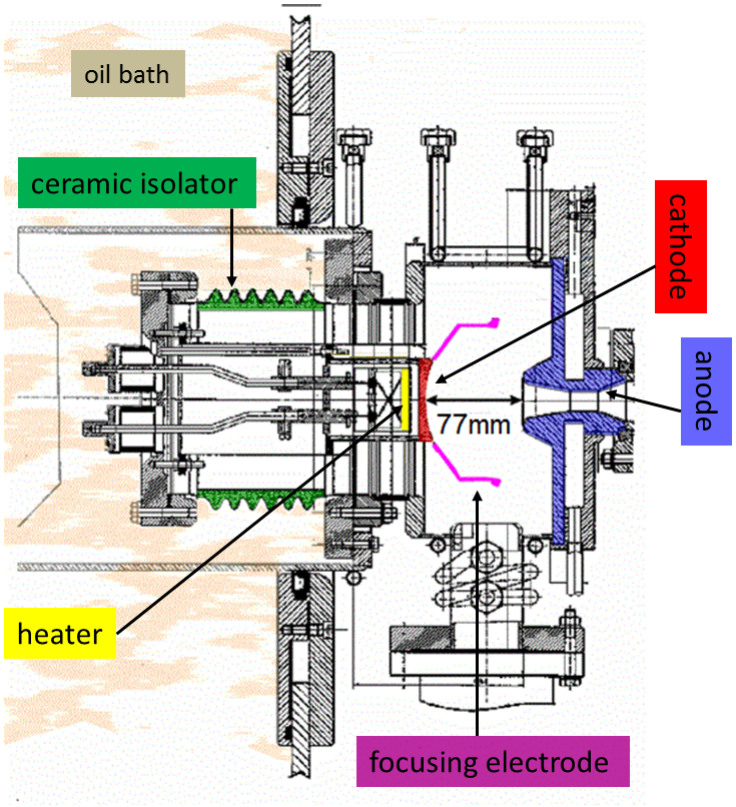

Figure 2.3: Drawing of the bombarder gun [12] operated in its oil bath with the old injection system. The ceramic isolator separates the oil bath from the beam vacuum.

of the linac. A drawing of the bombarder gun can be seen in figure 2.3. The cathode preparation for the existing gun is not trivial so that an alternative for the future had to be found, even though the present cathode reliably delivers electrons for more than ten years. Anyway incidental vacuum break downs occur due to sparks and hence the HV had to be reduced until present in order to stabilize operation. For operation of the injector complex electron pulses of a few ns pulse length are needed, depending on the mode of operation. Thus in case of the bombarder gun the chopper is required in order to cut away the undesired part of the generated electron pulse. It consists of a plate system, deflecting the undesired beam by a high voltage, and a collimator. The electron pulse generation in the triode gun for the new injection system, for which generation of beam current is normally space charge limited, and an overview of other methods for electron pulse generation are given in the next chapter.

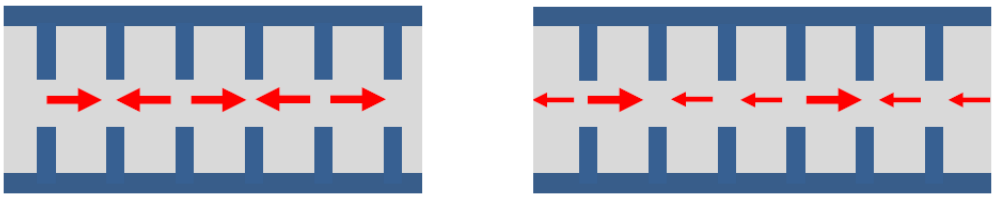

Figure 2.4: Illustration of π mode (left) and $2\pi/3$ mode (right) in a disk loaded traveling wave structure. The arrows indicate the direction of the electric field.

2.2.2 Charged particle acceleration using alternating rf fields

In general longitudinal electric fields are used for particle acceleration. The simplest way to accelerate charged particles is by using a static electric field such as used for the DC (direct current) gun of the Linac II explained above. The gained energy is equal to the product of the particle charge and the applied high voltage between cathode and anode. However the maximum voltage is limited by electrostatic discharge effects such as sparks. In order to reach the particle energies needed for an accelerator based light source the method of choice are alternating electromagnetic fields of high frequency. The achievable peak field is generally higher and the total accelerating voltage is not limited as for static electric fields. The beam can be accelerated to arbitrary kinetic energies by applying the field of any number of subsequent accelerator structures to it and by steering the beam through the rf accelerator structure several times like in synchrotrons and recirculating accelerators, where the maximum energy is limited by magnet field strength limits and the energy loss due to synchrotron radiation mentioned in section 2.1.
Since a longitudinal electric field is needed for particle acceleration, an electromagnetic wave in free space is not capable of particle acceleration. Thus structures are designed for purpose of accelerating particles with rf fields, having a wavelength in the order of magnitude of the structure's size. An electric field with longitudinal direction can be achieved for example by means of the TM_{01} mode in a simple cylindrical waveguide. In order to transfer energy from the rf field to a passing particle it is necessary to adapt the phase velocity to the velocity of the particle. That is for electrons usually the speed of light, while for the cylindrical waveguide the phase velocity is higher $v_{\mathrm{ph}} > c$. Therefore v_{ph} is adapted to the velocity of light by loading the waveguide with disks and therewith dividing it into cells. Different modes of the wave propagating through the disk loaded structure are imaginable for particle acceleration and usually the $2\pi/3$ mode is chosen. This means a phase advance of $2\pi/3$ per cell, such that a forward accelerating field is obtained in each third cell. Figure 2.4 illustrates the π mode and the $2\pi/3$ mode for such a structure. The particle gains energy in one cell and while it travels through the cell at almost the speed of light, the field rebuilds in the following cell with a phase advance of

$2\pi/3$. Thus acceleration continues and the distance between the disks has to be $\frac{1}{3} \cdot c/f_{\mathrm{rf}} = \lambda_{\mathrm{rf}}/3 = 33.33\,\mathrm{mm}$ for the parameters used at the Linac II, where f_{rf} is the frequency and λ_{rf} the wavelength of the applied electromagnetic wave. Basic relations on waveguides and accelerator structures are available for example in [13] and an overview of further rf field acceleration concepts can be obtained in [14].

2.2.3 Prebuncher

The prebuncher is a 2.998 GHz cavity whose accelerating voltage causes energy deviation of about 20 keV. The difference in velocity is sufficient since at 150 keV kinetic energy the velocity of $0.63c$ is not too close to the velocity of light. Lower energy particles drop back while higher energy particles from behind catch up and form a bunch. Acceleration by the first cell of section #1 starts close to the point where the electron density becomes highest. On average no energy is transferred to the electrons by the prebuncher, thus beam loading is not relevant.
For the prebuncher the loaded quality factor is $Q_L = \frac{1}{2}Q_0 \approx 800$ and $R_s/Q_0 = 66\,\Omega$, where R_s is the shunt impedance. Using these values, the accelerating voltage in the prebuncher can be calculated to

$$U_p = \sqrt{2P_{RF}R_s}. \tag{2.5}$$

2.2.4 The S-Band traveling wave structure

The accelerator structures of the Linac II are traveling wave structures which are operated with 2.998 GHz frequency. Their rf stations are equipped with SLED cavities [15], which offer the possibility to increase to rf power. The accelerating field propagates from the rf input at the coupling cell through the structure in direction of the beam and is absorbed partly while propagating through the active length and partly at the last six cells with a coating for absorption. Further parameters are listed in table 2.1.
In order to allow acceleration the phase velocity v_{ph} must be equal to the particle velocity v_p. Therefore compared to a simple waveguide structure the accelerating structures are disk-loaded, which is the most common way to realize accelerating structures for normal conducting electron linear accelerators. The structures of the Linac II consist of a sequence of 150+6 merged copper cells with a central hole which yields a structure with periodic iris apertures for the passage of the particle beam and electromagnetic coupling. Since electrons quickly reach velocities close to the speed of light the whole structure is adapted to that velocity. This arrangement of cells acts like a band pass filter allowing electromagnetic fields of certain frequencies to propagate which are determined by choice of the geometric dimensions [16]. Due to manufacturing tolerances an exact modulation of the frequency has to be done in

Parameters	Symbol	Value
Total length	L_t	5.2 m
Active length	L	5.0 m
Length of the load	L_L	0.2 m
Fill time	T_a	740 ns
Shunt impedance	r_s	51.5 MΩ/m
Attenuation	a	0.5 Np
Shunt impedance of the load	r_L	2.8 MΩ/m
Attenuation of the load	a_L	0.688 Np
Operation frequency	f_0	2.998 GHz
Temperature	T_{str}	40 °C

Table 2.1: Parameters of the Linac II structures [17].

a tuning process which will be described later for the new hybrid buncher structure in chapter 5.
Using the parameters in table 2.1 the total accelerating voltage and the influence of beam loading can be calculated as follows for the operation with a flat rf pulse as well as with a SLED pulse [17]. Because of the rf damping along the structure the diameter of the irises is gradually reduced towards the end of the structure. Thereby the group velocity decreases linearly to obtain a constant gradient in the unloaded structure

$$v_g = v_0 \left(1 - g\frac{z}{L}\right) \tag{2.6}$$

with $g = 1 - \exp(-2a)$ and v_0 the group velocity at the entrance. The time t required for the power to flow from the entrance to a position z along the structure is

$$t = -\frac{T_a}{2a} \ln\left(1 - g\frac{z}{L}\right) \tag{2.7}$$

Assuming that the damping is not influenced by the change of geometry the power is reduced by a constant rate

$$P(t) = P_0 \exp\left(-\frac{2a}{T_a}t\right) \tag{2.8}$$

and using (2.7) one finds

$$P(z) = P_0 \left(1 - g\frac{z}{L}\right). \tag{2.9}$$

The gradient E at a certain position of the structure is related to the energy line density W by

$$W = \frac{P}{v_g} = \frac{P_0}{v_0} = \frac{T_a}{2ar_s}E^2 \tag{2.10}$$

Inserting (2.6) for the total accelerating voltage follows

$$V_{\text{acc}} = \sqrt{r_s L P_0 (1 - \exp(-2a))}. \tag{2.11}$$

2.3 SLED pulse generation

SLED is a pulse compression scheme in which rf energy builds up in resonators of high quality factor Q during most of a klystron pulse's duration and is then largely extracted during the last fraction of the pulse. Reversing the phase of the input gives a great power multiplication and consequently a higher achievable beam energy. The relations presented in this section for acceleration using the compressed rf pulse are taken from [17]. Another detailed description of the SLED pulse compression and its applications can be found in [18]. Increased peak power afforded by SLED is accompanied by a sharp exponential decay, so that the average power within a compressed pulse is generally much lower than the maximum. The rectangular pulse from the klystron with a field amplitude of A_{in} is used to fill the SLED cavity for a certain time t_1. The amplitude inside the cavity is then

$$A_{\text{cav}}(t) = A_{\text{in}} \frac{2\beta}{1+\beta}(1 - e^{-t/T_c}), \tag{2.12}$$

$$T_c = \frac{Q_0}{(\beta+1)\pi f_0}, \tag{2.13}$$

with the coupling coefficient of the cavity β and a time constant T_c. At the time $t = t_1$ the klystron output is switched by 180°, so that for $t > t_1$ the amplitudes in the cavity and at the output respectively are

$$A_{\text{cav}}(t) = A_{\text{in}} \frac{2\beta}{1+\beta}[(1 - e^{-t/T_c}) - 2(1 - e^{-(t-t_1)/T_c})], \tag{2.14}$$

$$A_{\text{out}}(t) = A_{\text{in}} \left[\frac{2\beta}{1+\beta}(2 - e^{-t_1/T_c})e^{-(t-t_1)} - \frac{\beta - 1}{\beta + 1} \right]. \tag{2.15}$$

The emitted wave drops steeply as the cavity attempts to charge up to the opposite voltage, yielding the characteristic spiked output. The incident wave can be turned off after the compressed pulse has reached its desired duration, i.e. the fill time of the traveling-wave accelerator section. The output amplitude then drops by A_{in} and

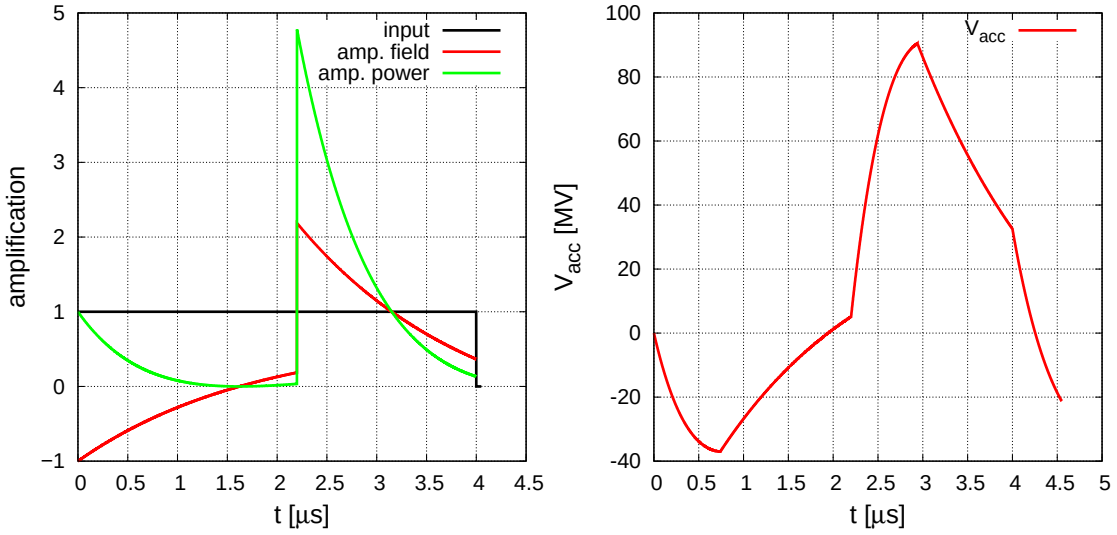

Figure 2.5: Calculated SLED pulse amplification of voltage and power for a flat input pulse and an instantanious phase jump (a). The resulting accelerating field in the structure being filled is shown in (b).

decays toward zero. The left plot in figure 2.5 illustrates the amplification induced to the rf pulse by the SLED cavity before and after the 180° phase jump.
The energy gained by a particle beam in traversing an accelerator structure powered with a SLED pulse is not boosted by as much as the peak field. This is due to the pulse's exponential decrease in amplitude and the finite fill time of the structures. The total accelerating voltage in a structure supplied with a SLED pulse can be calculated as follows

$$V_{\mathrm{acc}}(t) = \int_0^L E_{\mathrm{acc}}(t,z)dz \tag{2.16}$$

In order to calculate the accelerating voltage from the given parameters, the rf pulse must be expressed as a linear combination of three pulses expressing the wave before and after the 180° phase switch and after switching off. The function produced at the input of the structure is

$$E_1(t,0) = E_{\mathrm{in}}\left(\frac{\beta-1}{\beta+1} - \frac{2\beta}{\beta+1}e^{-t/T_c}\right). \tag{2.17}$$

By integration over the length of the structure that is actually filled L^*, the voltage before filling of the whole structure results to

$$V_1(t) = \int_0^{L^*} E_1(t + \frac{T_a}{2a}\ln(1-gz/L), z)dz. \tag{2.18}$$

The length L^* can be calculated from the attenuation coefficient and varying group velocity due to the design as a constant gradient structure

$$L^* = L\frac{1-\exp\left(-2at/T_a\right)}{1-\exp\left(-2a\right)}. \tag{2.19}$$

For $t < T_a$ the integral yields

$$V_1(t) = E_{\text{in}}L\left[\frac{\beta-1}{\beta+1}\cdot\frac{1-e^{-2at/T_a}}{1-e^{-2a}} - \frac{2\beta}{\beta+1}\cdot\frac{e^{-t/T_c}-e^{-2at/T_a}}{(1-e^{-2a})(1-\frac{T_a}{2aT_c})}\right] \tag{2.20}$$

and

$$V_1(t) = E_{\text{in}}L\left[\frac{\beta-1}{\beta+1} - \frac{2\beta}{\beta+1}\cdot\frac{e^{-t/T_c}(1-e^{-2a+T_a/T_c})}{(1-e^{-2a})(1-\frac{T_a}{2aT_c})}\right] \tag{2.21}$$

for $t > T_a$, when integrated over the whole length L. The second pulse, after the phase jump of 180° at t_1, corresponds to twice the negative amplitude of the first pulse

$$V_2(t) = -2V_1(t-t_1). \tag{2.22}$$

The third pulse, after switching off, is of positive sign again

$$V_3(t) = V_1(t-t_e). \tag{2.23}$$

The total accelerating voltage in the structure is expressed by

$$V(t) = V_1(t) - 2V_1(t-t_1) - V_1(t-t_e) \tag{2.24}$$

with an increased accelerating voltage of 90.55 MV at the maximum of $V(t)$ instead of 57.05 MV it is enhanced by a factor of 1.58. Figure 2.5 shows $V(t)$ for the parameters of the Linac II structures. In practice the phase jump is not alway conducted instantaneously, because adaptions of the phase evolution offer the possibility of optimizing the shape of the compressed pulse to the particular requirements [19,20].

2.3.1 Beam loading

If bunched electrons of current I_{beam} pass the structure, they generate rf fields, affecting the following bunches in addition to the rf field generated by the rf station. The result is an undesired multi-bunch energy spread, which can cause various problems such as particle loss. A general description of beam loading in linear accelerators is given in [21]. In case of the Linac II the beam current dependent induced accelerating voltage along the whole structure, adding up to the field generated by the klystron, can be calculated using the relations given in reference [17] to

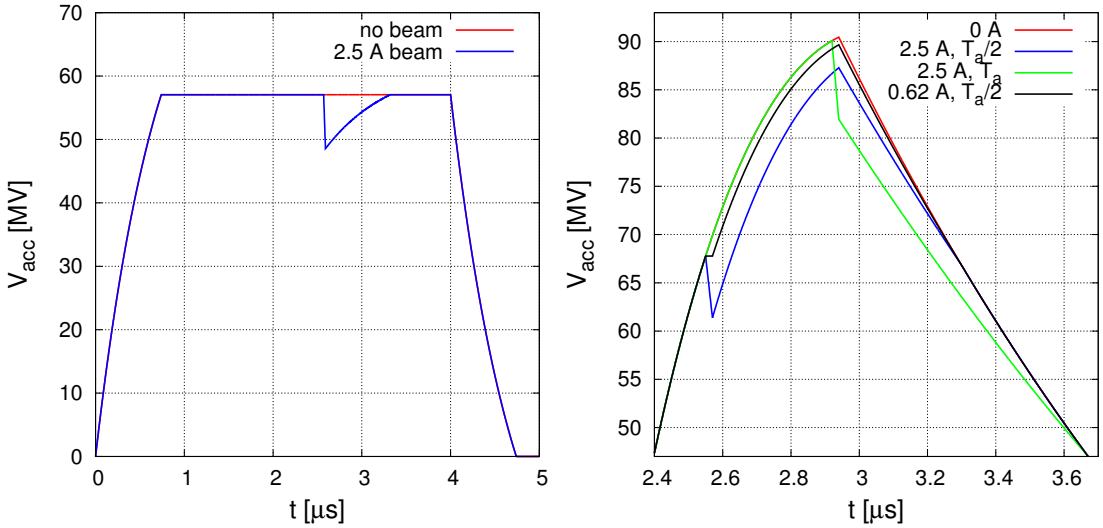

(a) (b)

Figure 2.6: The impact of beam loading on the accelerating voltage in a Linac II section filled with a flat rf pulse is shown in (a). The impact can be compensated using the SLED pulse for low beam current, but only partially for high current, by changing the timing to $t < T_a$, as shown in (b).

$$V_{\mathrm{ind}}(t)|_{t<T_a} = \frac{I_{\mathrm{beam}} r_s L}{2} \cdot \frac{1 - e^{-2at/T_a} - \frac{2at}{T_a} e^{-2a}}{1 - e^{-2a}}, \tag{2.25}$$

$$V_{\mathrm{ind}}(t)|_{t\geq T_a} = \frac{I_{\mathrm{beam}} r_s L}{2} \left(1 - \frac{2ae^{-2a}}{1 - e^{-2a}}\right). \tag{2.26}$$

Summing up these functions as done previously, the total beam induced voltage, adding to the field in the structure is

$$V_{\mathrm{ind}}^{\mathrm{tot}}(t) = V_{\mathrm{ind}}(t - t_{\mathrm{beam}} - t_{\mathrm{inj}}) - V_{\mathrm{ind}}(t - t_{\mathrm{inj}}), \tag{2.27}$$

where t_{beam} is the pulse length and t_{inj} the time when the beam pulse enters the structure.

Figure 2.6 shows the transient accelerating voltage V_{acc} for bunched beam of high current traversing the structure. The accelerating voltage is shown for the case of a 4 μs constant power rf pulse of 20 MW, i.e. a detuned SLED cavity, and for the SLED pulse. In case of the detuned SLED cavity V_{acc} drops to 48.5 MV from 57.1 MV. For the compressed pulse the drop of V_{acc} can be reduced from 8.1 MV for acceleration of 2.5 A beam current using the maximum accelerating voltage induced by the SLED pulse to 6.4 MV if the timing is chosen such that the beam is injected as soon as half the fill time has passed. Further examples are given in table 2.2. Stable energy can

be achieved only for relatively low beam current, for example $I_{\mathrm{beam}} = 620\,\mathrm{mA}$ with $V_{\mathrm{acc}} = 68\,\mathrm{MV}$. With a shorter structure of smaller fill time fields induced by higher beam current can be compensated. Hence that will be possible for the buncher structure, which is discussed in the following chapter.

timing	Q_{beam}	2.5 A·20 ns	2.5 A·50 ns	620 mA·20 ns
T_a	$V_{\mathrm{acc,mean}}$	86 MeV	79 MeV	89 MeV
	ΔE	8.1 MeV	19.5 MeV	1.7 MeV
$T_a/2$	$V_{\mathrm{acc,mean}}$	65 MeV	57 MeV	68 MeV
	ΔE	6.4 MeV	15.0 MeV	0.0 MeV

Table 2.2: Beam loading impact on accelerating voltage, for examples of timing, beam current and pulse length.

2.4 Beam diagnostics at the primary Linac II

In the secondary linac and PIA fluorescent screens and beam position monitors (BPMs) [4] are used as beam diagnostics. But in the primary linac the possibilities of beam properties measurement is very limited. Only three inductive current monitors are available as beam diagnostics. Until the new injection system with its beam diagnostics is installed, only intricate, indirect measurements can give further hints about the beam properties. A beam profile measurement at the converter target is presented in section 2.6.

2.4.1 Inductive beam current monitors

In front of the converter three inductive current monitors are installed, one of which (IMA-gun) measures the beam current generated by the gun in front of the injection into the first accelerator section. The other two are located between section #1 and section #2 (IMA01) and in front of the converter (IMA05) respectively. Thus beam losses can be located insofar that they occur either before or inside the section #1 or while passing one of the four other accelerator sections. Losses on the apertures of the short vacuum chambers between the sections or behind section #5 are improbable, because the iris aperture of the cells is smaller than its inner radius. Transmissions from IMA-gun to the two other current monitors, based on archived current values for an example time period, are shown in figure 2.7. For high beam current of 5 A transmission of up to 80% from IMA01 to the converter is reached. Seen from the gun the losses are much higher and only up to 50% beam current is

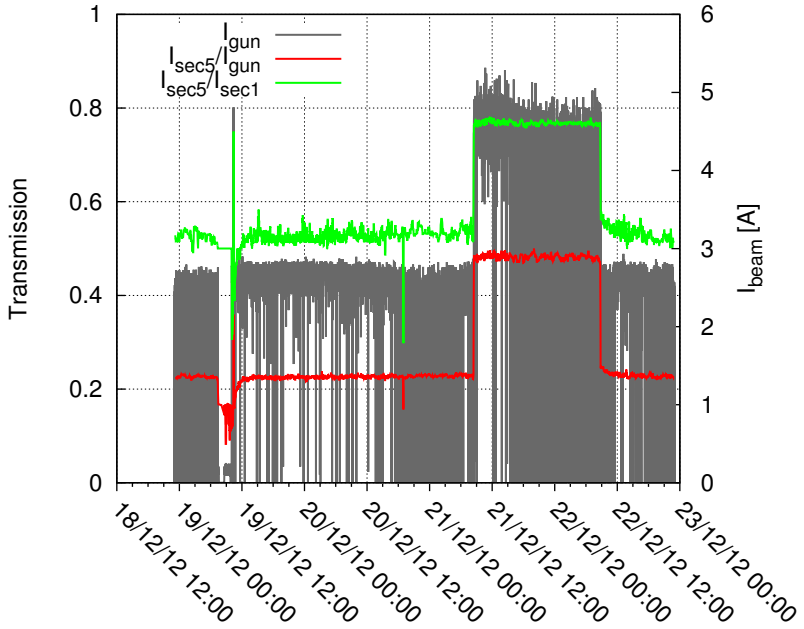

Figure 2.7: Example of archived beam current in the injection system and transmission from the gun and section #1 respectively to section #5 during operation on December 18th-23rd, 2012.

transmitted. Related to the expected emission of 6 A at the cathode the losses add up to above 60%.

2.5 Electron positron converter

The target for conversion from electrons to positrons by pair production is a tungsten plate of 7 mm thickness. Its thickness was chosen for optimum positron yield at an incident kinetic energy of 400 MeV. Because of the high activation, the target and its surroundings are built in a manner that eases maintenance, i.e. no movable parts are used and a permanent shielding is included in the design. For the case that electron transmission into the secondary linac is required, the converter target has an aperture of 5 mm diameter. Electrons can be steered through it by means of the steering coil installed at the beginning of section #5. Figure 2.8 illustrates the geometry of the conversion target. It is directly followed by a short solenoid with a strong pulsed field of 1.8 T for focusing of the positrons, generated in a wide opening angle. Nonetheless most positrons leaving the target are lost. The first two accelerator sections downstream of the converter are equipped with a 0.4 T solenoid magnet.

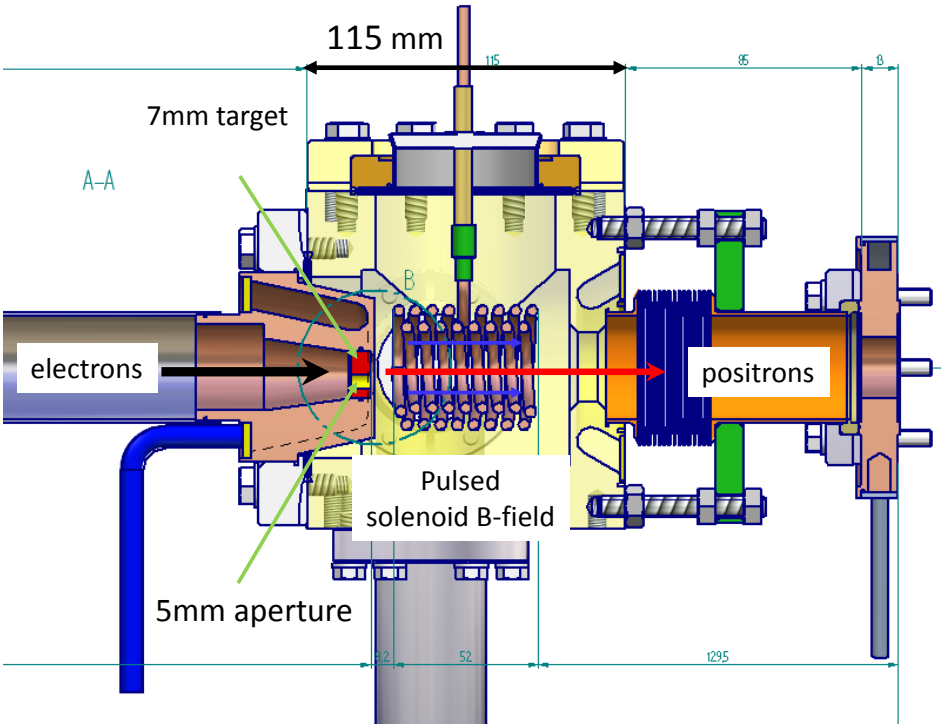

Figure 2.8: Mechanical drawing of the converter. For positron production, the tungsten target is used with the pulsed solenoid behind for focusing. In case of electron operation, the beam is steered through the aperture in the target.

2.6 Beam profile at the converter target

In order to investigate the loss along the Linac II primary accelerator, knowing beam properties as beam size, profile and position is important, but adequate beam diagnostics are missing. This lack has tried to be eluded by scanning the electron beam in horizontal and vertical plane over the aperture in the converter target, while recording the measured current at IMA05 and IMA07. The ratio of the measured beam current values can be plotted depending on the transversal coordinates. The coordinates were calculated from the integrated field of the steering coil and the particle momentum. That has to be calculated from the rf input power of the accelerator sections, since no accurate measurement by sufficiently large deflection is possible. The resulting beam profile at the converter is shown in figure 2.9 together with a profile obtained from simulations, which is anticipated from chapter 4. The origin of the coordinate system corresponds to a zero field in the steering coils. The profile shows no abnormality as beam halos, that would intuitively identify a problem, but a small asymmetry can be observed. The intensity gradient is higher for negative x and y, what can be caused by divergence due to dispersion. Dispersion can originate from a steering coil at significant energy spread. However the linac was used for electron operation at that time and with a current of 200 mA the energy spread due to beam loading must be significantly lower than in positron operation. The obtained beam size is small with regard to the inside diameter of the hole in the tungsten target. No significant loss is to be expected along the linac for a beam of such size. A systematical underestimation of the beam size is possible, because the actual beam energy might be lower than calculated due to off crest acceleration in the linac structures.
The beam spot obtained from simulations is shown as well in figure 2.9. It is smaller than the measurement result due to the aperture influence. Because of the absence of misalignment, asymmetries are only due to the finite number of macro particles, being tracked through the linac. In order to make the simulation result comparable to the measured profile, a convolution has been carried out, and is presented in the figure, too. The resulting profile is bigger than in the measurement, whose accuracy suffers from the beam energy estimation.

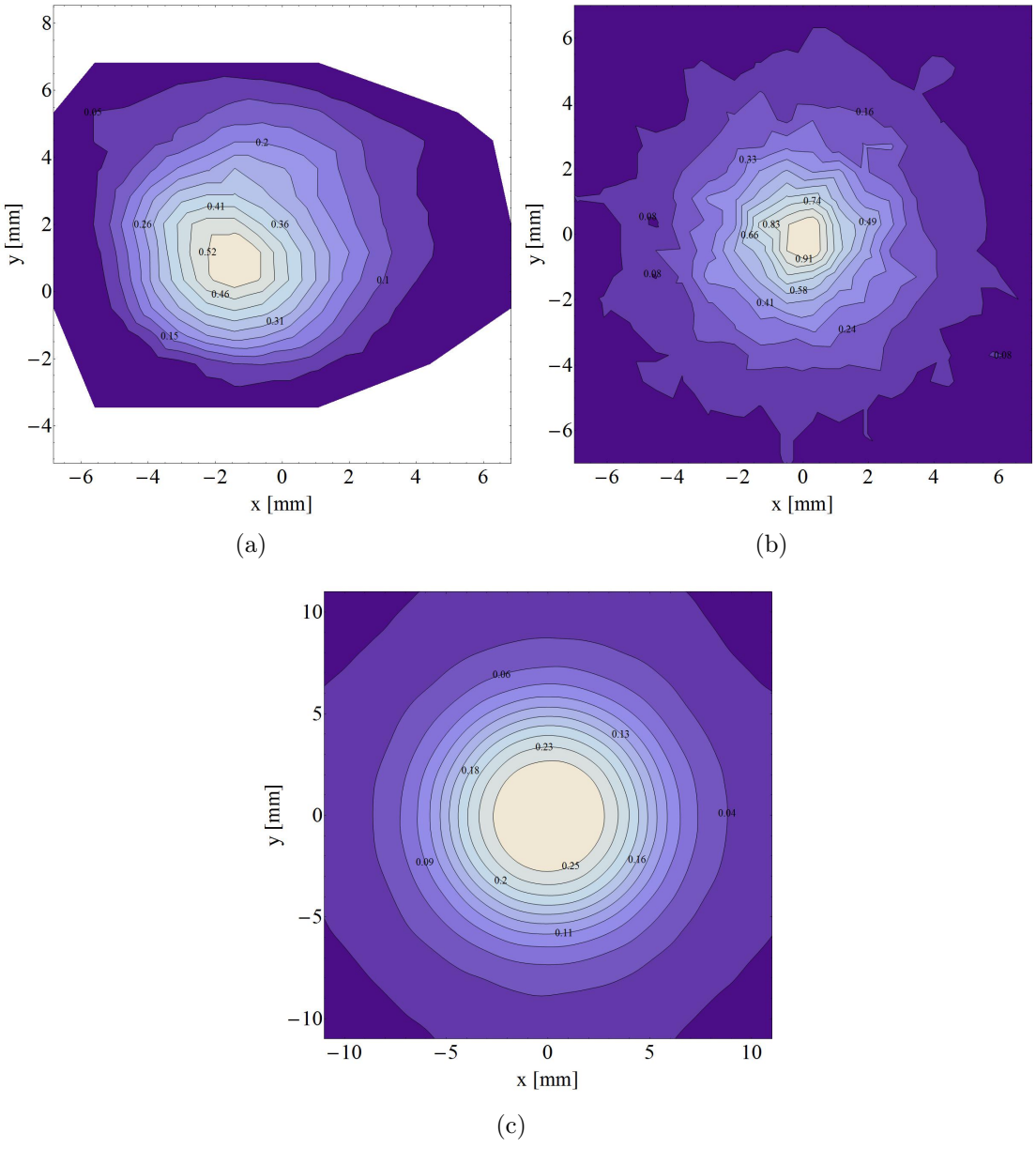

Figure 2.9: Scan of the electron beam over converter target aperture (a) and profile from particle tracking in ASTRA (b). For better comparison a convolution of the calculated beam is shown as well (c).

Chapter 3

Design and functionality of the new injection system

3.1 Motivation and requirements

After decades of successful operation mainly for particle physics experiments [22, 23] the HERA accelerator has been shut down in 2007. Afterwards, the PETRA ring which injected the beam into HERA was upgraded to a high brilliance hard X-ray light source [7, 8, 24]. The Linac II serves as electron and positron source for the storage ring light source PETRA III which provides the possibility to do X-ray experiments at 14 experimental stations since 2010. Due to the high user demand for occasions to perform experiments, an extension with two further experimental halls and ten further experimental stations are constructed in the upcoming shut down. The extension with focus on two beam lines is presented for example in [25]. The permanently high demand of beam time by also many external users requires a very reliable operation of the storage ring 24 hours a day and 7 days a week. Since the Linac II was operated since 1969 as described in [1] and was designed for a machine with more flexible planning of access for maintenance, required changes were implemented [11] or are under way in order to ensure the reliable operation, including the new injection system.

As mentioned before there are some unsatisfactory constraints in operating the Linac II as it is now. The major difficulties of the current design are the high beam losses at high energies that cause activation in front of the electron positron converter, as discussed in section 2.4.1. Together with the activation that has been caused at the converter, it turns the (for a machine of such age unavoidable) maintenance to a very complex work. Except current monitors no beam diagnostics are installed to identify possible reasons for the particle losses and the few beam optics magnets and steering coils do not offer the possibility to reduce them further.

Another difficulty for reliable long-term operation of the bombarder gun is the risk

of a leak in the HV isolating ceramics. For electrical and heat extraction purposes, the gun is operated in an oil bath. A damage of the ceramics isolator would lead to high cost and a long downtime. In addition, the cathode preparation for the bombarder gun is not trivial and it is operated since 2001 with the last available cathode. To avoid the effort of cathode preparation a gun which can be operated with commercially available cathodes was chosen for the new injection system.

Besides it was mandatory to choose a system which delivers a high peak beam current of 6 A like the old gun to sustain the capability of getting sufficiently high beam power to the converter for operation with positrons. In most modes of PETRA III operation, depending on the user demand, a multiple of the required positron number can be accumulated in PIA. The maximum number of particles in PIA is defined by space charge induced beam loss at approximately $4 \cdot 10^{10}$ particles. However, the failure of one klystron modulator and consequently operation with reduced energy is not unusual and can temporarily limit the number of positrons. Hence no compromise in terms of beam power was to be accepted. With the Y796 from Eimac in the United Kingdom [26], a cathode was found which fulfills all requirements and is going to be used in the triode gun of the new injection system.

Until December 2012 PETRA III was operated with positrons only, because operation of the DORIS ring required a positron beam. After experiments, which intended to investigate the effect of multiple photon exchange on elastic electron-proton and positron-proton scattering cross sections at DORIS within the OLYMPUS collaboration [27] and took place mainly in 2012, DORIS was finally shut down. Since then it is possible to run PETRA III with both types of particles. The option to make experiments with positrons needs to be sustained because there is a difference for storage rings between electron and positron operation. This is due to ion- and electron cloud effects respectively.

Detailed facts about such effects, which reduce the life time of a stored beam, are given in [28, 29]. Since the planning and tests for the new injection system started long before electrons could be tried in real as particles for PETRA III, the risk not having the option to go back to positrons, could not be taken. A second reason is that even though DESY has changed from a mainly particle physics facility to running 3rd and 4th generation light sources, there are only few facilities in the world which have the opportunity to provide positron beams. Accordingly the decision was made to keep this option. Aside from future use directly for particle physics experiments needing positrons, there is demand for positron accelerators in new accelerator physics fields.

For instance interest in the positron beam has been expressed by members of staff working on plasma wake field acceleration (PWA). There is progress in research of PWA at DESY and other facilities which could be applied as an alternative technology for an electron positron collider [30]. Previously the possibility of accelerating positrons using that technology must be investigated experimentally and accordingly

the availability of a positron source might become important for DESY. However the Linac II lacks the beam quality in emittance and bunch length for such an application. Hence development of complex changes would be required in case such use is desired in the future.
Another important point is that the installation and commissioning of the new injection system comes along with a couple of other higher priority projects, i.e. the XFEL (European X-ray free electron laser), FLASH II (Freie-Elektronen-Laser in Hamburg) and PETRA III extension. As a consequence availability of the technical staff for conception and commissioning is limited. Thus an additional requirement for planning and commissioning of the new injection system and the precedent test stand is simplicity and application of approved technology in a reasonable extent, in order to finish the build-up in the foreseeable future, while expenditure of human labor is not overdrawn. Accordingly a design was pursued that does not need an additional rf station in the Linac II modulator hall and is based on or close to existing component design. This was an important demand for the chosen design of the buncher structure, as will be explained later.

3.1.1 Principal design aspects

The following aspects were taken into account as limiting factors for the starting design of the new injection system.

1. Disassembly of the bombarder gun would be unreasonable since very stable operation of the new triode gun cannot be expected at once. Therefore, the bombarder gun will stay in place with a modified injection system and the new injection system will be installed in addition to have a redundant system available. Thus the new injection system should be built separately and merged with the old system by means of a magnetic chicane. Due to the according redundancy, operation of the Linac II with the triode gun is testable, while in case of failures of the added system, switching to the bombarder gun is possible, without causing unscheduled downtime for maintenance. Such a redundancy will be advantageous, if the previously mentioned sparks in the bombarder gun and the associated vacuum break downs occur again.

2. A new buncher structure for better electron capture was under development in order to reduce beam loss by means of better electron capture. A detailed description is given later in this chapter. Similar to the Linac II accelerator sections the buncher structure is surrounded by two solenoid coils in a iron cage enclosed by massive iron plates. They center the focusing solenoidal fringe fields in front of the aperture of the structure.

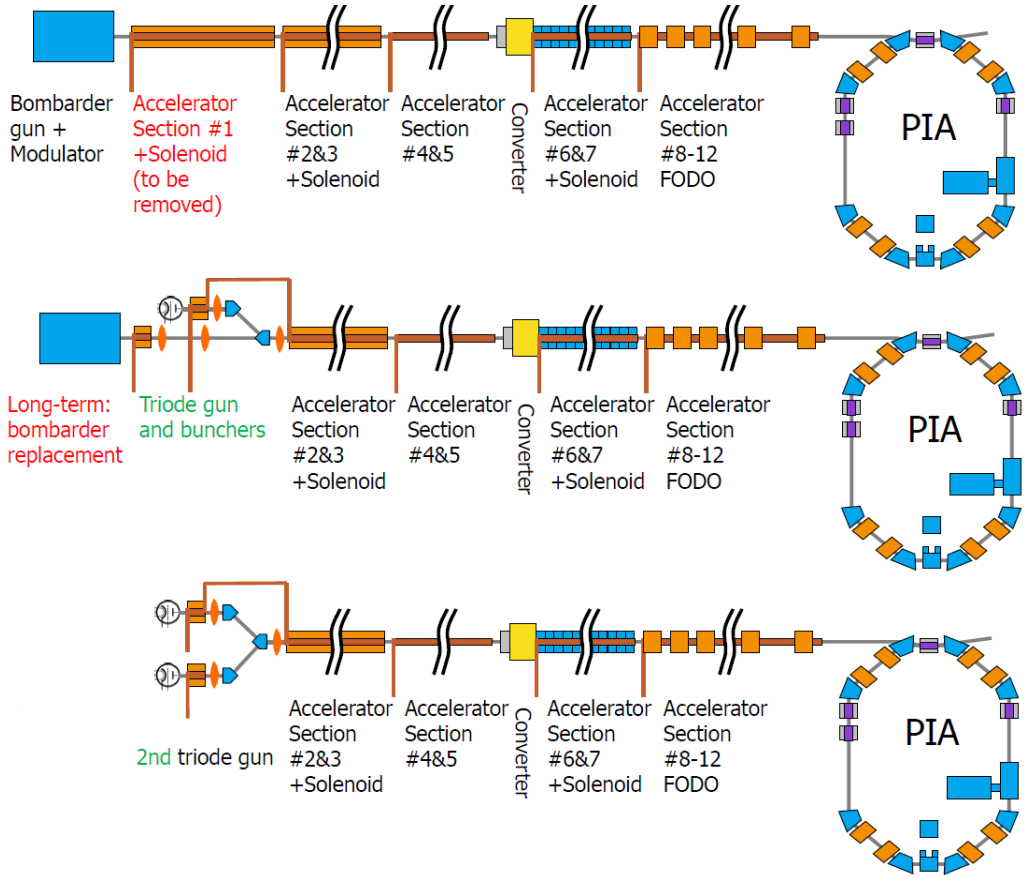

Figure 3.1: Overview of the Linac II and PIA after installation of the new injection system in place of section #1 (center) and a possible long-term setup with the bombarder gun uninstalled (bottom). Note that not each individual component is shown in this overview. For comparison the status quo (top) is illustrated again.

3. The bombarder gun injection system cannot be moved backward sufficiently to make place for installation of a new electron source and buncher structure above. Hence with the mentioned restrictions removal of one of the accelerator structures was the only measure that creates the needed space for the additional injection system.

4. Following from 3. the choice was made to remove the first accelerator section, because that way more accelerator sections can be used for acceleration of the beam injected from the new triode gun system. However a shorter accelerator section was needed, accelerating the beam coming from the bombarder gun sufficiently to stabilize the particle distribution in phase space in order to make the beam transportable to accelerator section #2. That task was supposed to be fulfilled by a second identical buncher structure.

The principal changes to the Linac II are shown in figure 3.1. The figure includes the status quo and the two steps of modification. In long-term planning the bombarder gun is to be disassembled and, if the triode gun injection system proves reliable, a second identical system can be installed, as indicated at the bottom drawing. Please note that in operation of the test stand beam loss behind the buncher structure occurred, what is discussed in chapter 6 in full detail. The doubts that were left whether as much beam can be transported to section #2 by use of the buncher structure in combination with the bombarder gun, as presently possible by means of section one, finally led to modified plans of replacing section #2 instead of section #1. The most recent plannings are denoted in the outlook in chapter 7.
A mechanical drawing of the new injection system with the second buncher structure and the beam line for the bombarder gun below is shown in figure 3.2. The reason for the vertical installation is the limited space sideways in the tunnel. Not all components are shown in the drawing, i.e. BPM buttons and vacuum feed-through, input and output waveguide, HV rack and further infrastructure are missing.
The principle resembles the injection system for the bombarder gun. For the total length used for setting up all components it had to be observed that the rear of the gun, which is at high voltage, needs a minimal distance to the load at the second coupling cell of the second buncher. A gap of 30 cm was considered sufficient. Beam pulses from 2 ns length are generated and accelerated by high voltage of typically 100 kV. A chopper is not needed, because the electron source is built as a triode. Solenoids focus the beam and an identical prebuncher, that was manufactured alongside the exemplar in use at the bombarder gun, compresses the beam into bunches.
Due to the removal of accelerator section #1 the maximum achievable energy at the converter target is reduced by one fifth from about 400 MeV to 320 MeV. Hence a lower conversion rate can be expected, notably because the target thickness was

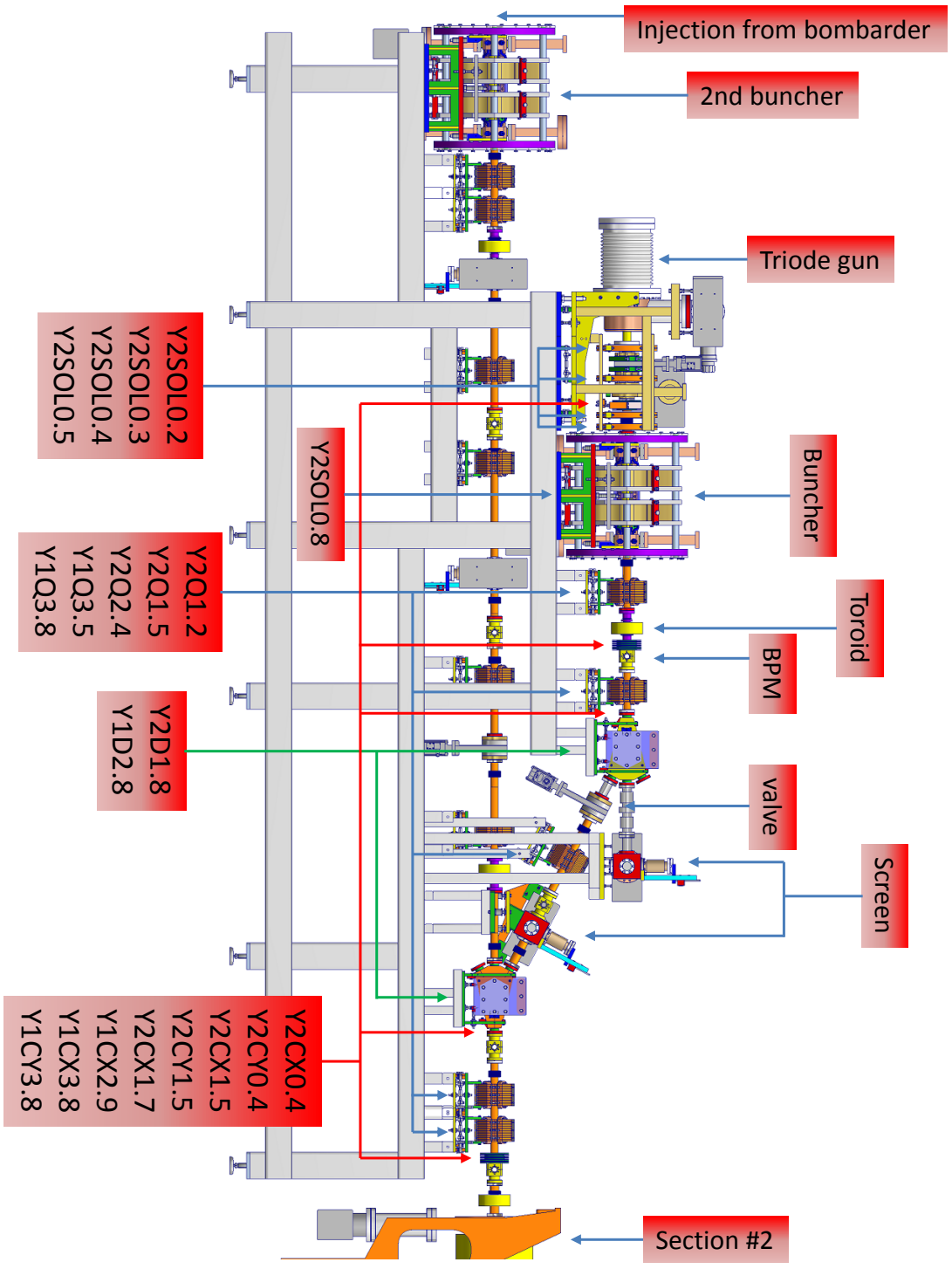

Figure 3.2: CAD drawing of the new injection system in place of linac section #1 with the second buncher and straight beam line for the bombarder gun below. The nomenclature of the magnets refers to their position and type, which are written out in table 3.2.

optimized for 400 MeV electrons. An analysis of the performance to be expected at lower energies is given later in section 4.5, where EGS5 (Electron-Gamma Shower) simulations are evaluated.
Number and positions of quadrupole magnets were optimized using the MADX (Methodical Accelerator Design) code [31] in order to get a starting point for the beam optics and ASTRA (A Space Charge Tracking Algorithm) [32] was used for minimization of particle loss. Results of these simulations are as well presented in the following chapter.
The magnetic chicane adds the advantage of losing particles at low energies, that would be lost anyway, without causing activation and therewith avoiding activation at higher energies in the accelerator sections. A variable aperture in the magnetic chicane, originally planed for use as an energy filter, has not been installed in the test stand. Still energy collimation takes place by means of the vacuum chambers inner diameter of 32 mm. If not made up, an alternative presently still under investigation is to add a second quadrupole magnet in order to compensate for dispersion. That might prove useful because of a measured energy spread above expectations behind the buncher structure, even though simulations did not show need for a dispersion free setup in terms of beam loss at energies above 10 MeV.

3.1.2 Method of electron pulse generation

For the new injection system, a thermionic triode gun will be used, that was originally developed for the S-Band Test Facility (SBTF) [33–36]. After closing down the SBTF it was given to the Elektronen-Stretcher-Anlage (ELSA) in Bonn where it was not required any more during the recent years. A detailed description of the injection system at ELSA is given in [37]. Hence it could be retrieved for constructing the new injection system. A heated filament is used instead of electron bombardment and instead of the chopper the cathode uses a grid close to its surface for pulse length control. It rejects electrons leaving the surface by means of a negative voltage U_{bias}. For the desired pulse length the grid opens for electrons by a pulse of positive voltage U_{puls1} and is closed by a second pulse U_{puls2}. For the emission control by U_{bias}, U_{puls1} and U_{puls2}, voltages of a few hundred volts are sufficient because the grid is located close enough to the heated cathode surface.
The emitted beam current is not only limited by the emission on the cathode surface, given by the used material and its temperature for thermionic electrons guns, but also by space charge. It limits the emitted current to a value depending on U_{HV} and a constant given by the geometry of the setup, the perveance P. If sufficient electrons are emitted from the surface, only as many leave the surface and are accelerated by U_{HV} as needed in order to compensate the charge, that would represent the anode, if the setup is regarded as a charged capacitor. Assuming that the particles are accelerated uniformly between cathode and anode, the relation between U_{HV} and

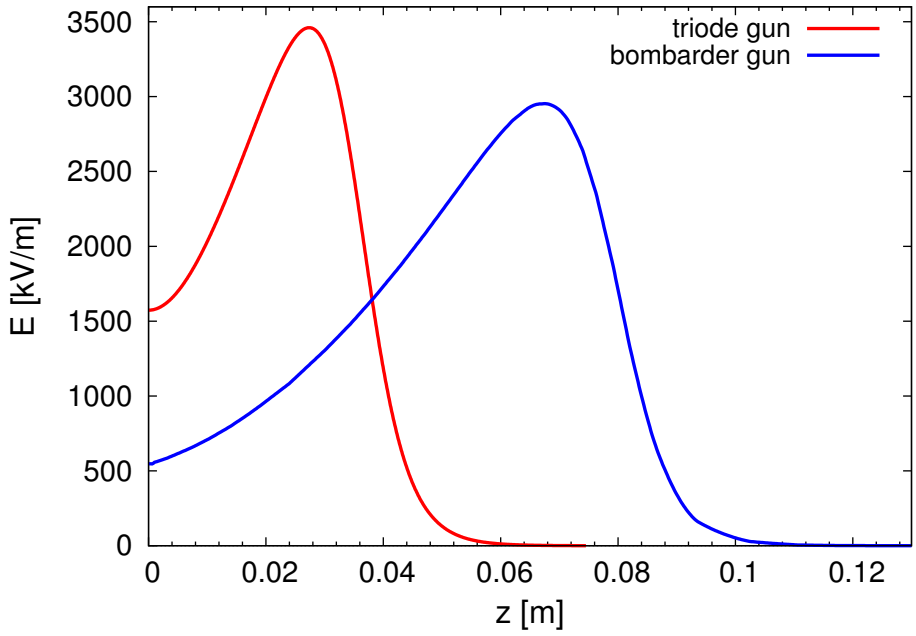

Figure 3.3: Comparison of static electric fields for 150 kV at the bombarder gun and 100 kV at the triode gun from calculations in CST EM Studio.

beam current I_{beam} can be calculated. In contrast to the bombarder gun the triode gun is supposed to be operated space charge limited, with the following relation

$$I_{\text{beam}} = P U_{\text{HV}}^{\frac{3}{2}}, \tag{3.1}$$

that also follows from the Child-Langmuir Law [38]. In case the space charge limit is reached at the desired beam current of 6 A, the gun has a perveance of

$$P = 0.006\,\text{A}/\text{kV}^{3/2}.$$

Detailed explanations about the functionality of thermionic tubes is given for example in [39]. Figure 3.3 shows the field distribution in bombarder and triode gun at applied HV of 150 kV for the bombarder and 100 kV for the triode respectively, as used in standard operation. At the cathode surface for $z = 0$, a lower electric field results for the geometry of the bombarder gun. Nevertheless, due to the big radius of the bombarder's cathode of 30 mm compared to the smaller Eimac Y796 for use in the triode gun, it is capable of generating 6 A beam current without reaching the space charge limit.
Aside from the triode gun, use of an injection system designed at MAX-lab in sweden [40, 41] was also taken into account before the decision fell to the former SBTF triode gun. It contained an rf gun and an energy filter in a compact design and was capable of delivering 900 mA beam current behind the energy filter [11]. Even

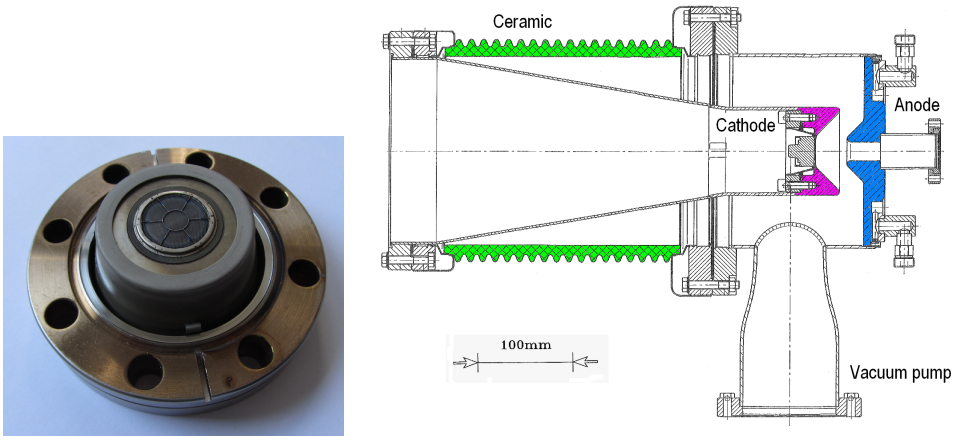

Figure 3.4: Cathode image and mechanical drawing of the triode gun for the new injection system. The PCB for its control and connection of the cathode to the HV-rack is placed in the conical rear of the gun.

for maximum transmission its use had meant a reduction of positron production performance and was discarded.

3.1.3 The thermionic DC triode gun

The mechanical design of the gun for the new injection system and an image of the cathode are shown in figure 3.4. The system is operated as a triode with the Y796-cathode from Eimac. Gun control, i.e. setting of parameters as pulse length, beam current and accelerating HV, is performed by means of a pulser electronics, located in a HV rack and lies on high potential together with the PCB (printed circuit board), that is connected directly to the cathode. The gun control system was delivered and commissioned by the external company PPT Puls-Plasmatechnik GmbH [42, 43].

3.1.4 Classification compared to other concepts for electron injectors designed for differing requirements

As an electron source for 3rd generation light sources, similar systems are commonly used with however lower maximum beam current, because positron generation is not an issue. For example injection systems based on the developments at the SBTF have been built for the Swiss Light Source (SLS) [44] and the Diamond Light Source (DLS) [45] by the company ACCEL GmbH. Both use a thermionic DC triode gun and 2.998 GHz traveling wave structures with a total charge of the bunch train of

1.5 nC at SLS and 3.0 nC at DLS. Their bunching systems differ from the Linac II injection in matters of the subharmonic prebuncher and the two buncher structures of which the first was designed for relativistic electrons of $\beta = 0.6$ and operates in $2\pi/3$ mode, while the second was designed for $\beta = 0.95$ and operates in $8\pi/9$ mode. Both systems are operated at rf power below 20 MW and mention an emittance of approximately $50\,\pi$ mm mrad. An accelerator designed for high beam current and positron generation is the Frascati Linear Accelerator for Dafne, which is based on the original Stanford Linear Accelerator Center (SLAC) injector [46]. It generates up to 10 A beam current of which 7 A at an energy of 250 MeV are transmitted to the tungsten target for positron generation. In addition a prebuncher cavity, a $\beta = 0.75$ TWS is used with 0.5 MeV output energy and a $\beta = 1.0$ constant gradient structure completes bunching and accelerates to 45 MeV. The resolved positron yield is stated 36 mA.

Aside from thermionic DC guns with dedicated prebuncher and buncher structures, other commonly applied electron injector principles use rf guns, photocathodes, or both. An example for an injection system using an rf gun is the rf gun system mentioned in section 3.1.2 that was tested but could not fulfill the requirements for the Linac II. An advantage is the initial acceleration and bunching by the high rf electric field and as a consequence the missing space charge limit for emission and the lower influence of space charge that occurs particularly during the drift between prebuncher and adjacent buncher structure. Instead of HV generation an rf source is needed for operation which can usually be considered a higher effort. An advantage of DC guns is the possibility of higher repetition rate up to continuous wave (cw) operation.

Where high brightness and low emittance is required from the injection system, rf photocathode injectors are often chosen, which use a laser to induce photoemission on the cathode surface. For example FLASH uses a Cs_2Te film on a molybdenum plug. These properties are notably advantageous for the performance of free-electron lasers (FEL), like for example FLASH and the European XFEL [47]. High brightness and low emittance photoinjectors can be realized as well by means of a DC gun as can be seen in the example of the injector developed at Cornell University [48] for a X-ray light source based on an energy recovery linac (ERL). However very high voltage of up to 750 kV is used in the DC gun. A trade-off has to be made considering the benefits of photocathode rf gun operation and the high effort for the laser system and due to the normally shorter cathode life time.

These examples intend to give a brief overview of alternative electron injector concepts, whereby other more specialized concepts were developed as well such as SRF guns and hence the above listed do not claim to be complete. For the Linac II, the thermionic DC gun fulfills all requirements and for reliability and simplicity purposes the gun built as a triode is the optimum technique. The following section presents the rf and bunching system for the new injector.

3.2 Bunching system

During tests buncher and prebuncher were supplied with rf by the linac's klystron modulator #15, which is available in the modulator hall for tests independently from Linac II operation. Pulses generated by the klystron can be compressed by means of a SLED cavity. The rf power is extracted partially behind the second coupling cell for the prebuncher. Using a phase shifter and an attenuator the prebuncher field can be adapted to the demand. The accelerating voltage in the buncher structure is adjusted directly by the rf power from the klystron.

3.2.1 The hybrid buncher structure

The new hybrid buncher structure [49] consists of totally 14 cells of which the first is shorter. That is a $\beta = 0.5$ capture cell, which is operated in the π mode with a standing wave, while the other 13 cells are operated in $2\pi/3$ mode as a traveling wave structure. The traveling wave part corresponds to the design of the other linac accelerator structures, except that the iris aperture is not adapted in order to obtain a constant gradient structure. Additionally two of the traveling wave cells (1st and 13th) are coupling cells. By means of the second coupling cell a load can be connected or the rf power leaving the buncher structure is used to feed the following accelerator structure. That way no additional rf station is needed for the buncher in the new injection system. A phase shifter and a vacuum window, both capable to bear the maximum rf power of 50 MW, are installed in between in order to separate the vacuum sections for the two structures and to choose the correct phase independently. Figure 3.5 shows a mechanical drawing of the structure and the field distribution resulting from a MWS (CST Microwave Studio) simulation. Other designs of hybrid buncher structures have been proposed for example in [50, 51].

3.2.2 Rf pulse usage

However the option to operate the buncher structure and the following Linac II accelerator section with only one rf station necessitates some compromises in terms of the filling and rf pulse shape for the two structures. A total fill time of $\sim$800 ns is expected if the waveguide between the structures is taken into account. The possibility to operate the buncher structure with a detuned SLED cavity and the attempt to compensate beam loading at lower rf power must be considered. The following describes briefly what modes of operation are possible:

1. Using of the SLED pulse with the accelerator section filled, the accelerating voltage in the buncher structure is relatively low (theoretically $\sim$5 MV). The maximum beam energy of the primary linac can be achieved, but beam loading compensation in the buncher structure cannot be provided. If the shape of

the phase jump for generation of the SLED pulse is adapted, rf pulses of different form can achieved. Examples of such pulse compression by phase modulation are presented in [19, 20] and might be used to achieve a higher field for electron capture in the buncher structure, if that turns out to be necessary while commissioning.

2. If the accelerator section behind the buncher structure can be operated with an independent rf station, beam loading can be approached using the steep rising rf power of the compressed pulse, just as discussed in the previous chapter for the linac sections.

3. (a) Operation with detuned SLED cavity and hence a flat rf pulse offers sufficient pulse length to fill both buncher and accelerator section. However lower energy is reached, because over the full length of the section only accelerating voltage of 57.05 MV instead of 90.55 MV is achieved, as calculated in section 2.3. The beam induced field affects both buncher and accelerator section. For higher beam currents accelerating voltage drops significantly.

   (b) By means of a feed forward control a rising rf power step from P_1 to P_0 for compensation of beam loading can be enabled, even with a filled accelerator section. However the maximum rf power is still as low as in 3. a) and has to be decreased before the beam pulse enters the buncher structure. The influence of this approach on the accelerating voltage of the buncher structure is calculated in the following.

3.2.3 Buncher accelerating voltage

Before consideration of beam loading compensation, the structure's accelerating voltage $V_{\mathrm{acc,b}}$ must be calculated anew. In case of the buncher the relation for its calculation differs from equation (2.11) since the traveling wave part is made from cells of equal irises. Hence damping of 0.045 Np along the structure reduces the gradient, assuming that attenuation per unit length of the structure does not change. It is assumed, that differing absorption and group velocity in the capture cell can be neglected. Hence the length of the structure used in the calculations is $L_b = 0.45\,\mathrm{m}$, where all cells are included. The used parameters of the buncher structure are given in table 3.1.
Using equation (2.10) and the relation

$$P(z) = P_0 e^{-2a_b \frac{z}{L_b}} \tag{3.2}$$

to describe damping yields the accelerating voltage for a structure with decreasing gradient:

Parameters	Symbol	Value
Length	L_b	0.45 m
Fill time	$T_{a,b}$	42 ns
Shunt Impedance	r_s	51.5 MΩ/m
Attenuation	a_b	0.045 Np
Operation frequency	f_0	2.998 GHz
Temperature	T_{str}	40 °C

Table 3.1: Parameters of the hybrid buncher structure.

$$V_{\mathrm{acc,b}} = \sqrt{\frac{2r_s P_0 L_b}{a_b}}(1 - e^{-a_b}). \tag{3.3}$$

In order to get information of how the buncher can be operated with non constant input power, the amplification $A_{\mathrm{out}}(t)$ must be included in the calculation. It can describe the pulse compression by the SLED cavity, as expressed in equation (2.15). In case of the feed forward (detuned SLED cavity) it describes the rf power relative to P_0.
For calculation of the time dependent accelerating voltage $V_{\mathrm{acc,b}}(t)$ the field $E(z,t)$ must be integrated along the length of the structure. The electric field is calculated according to equation (2.10), where the rf power has to be replaced by the time dependent input power. For the voltage follows

$$V_{\mathrm{acc,b}}(t) = \int_0^{L_b} E(z,t)dz \tag{3.4}$$

$$= \int_0^{L_b} \sqrt{\frac{2a_b r_s P_0}{L_b}} \cdot e^{-z\frac{a_b}{L_b}} \cdot A_{\mathrm{out}}(t - \frac{z}{v_0})dz. \tag{3.5}$$

For the example input power distributions the integration has been performed numerically. For a prediction of how beam loading affects the accelerating voltage, the beam induced voltages have been added according to equation (2.27) for the respective beam current. Even though that voltage was derived for the constant gradient structure, it describes the induced voltage in good approximation due to the low attenuation.

3.2.4 Compressed rf pulse

The high peak power of the SLED pulse traveling through a structure with short fill time such as the buncher leads to a steeply rising acceleration voltage, as shown

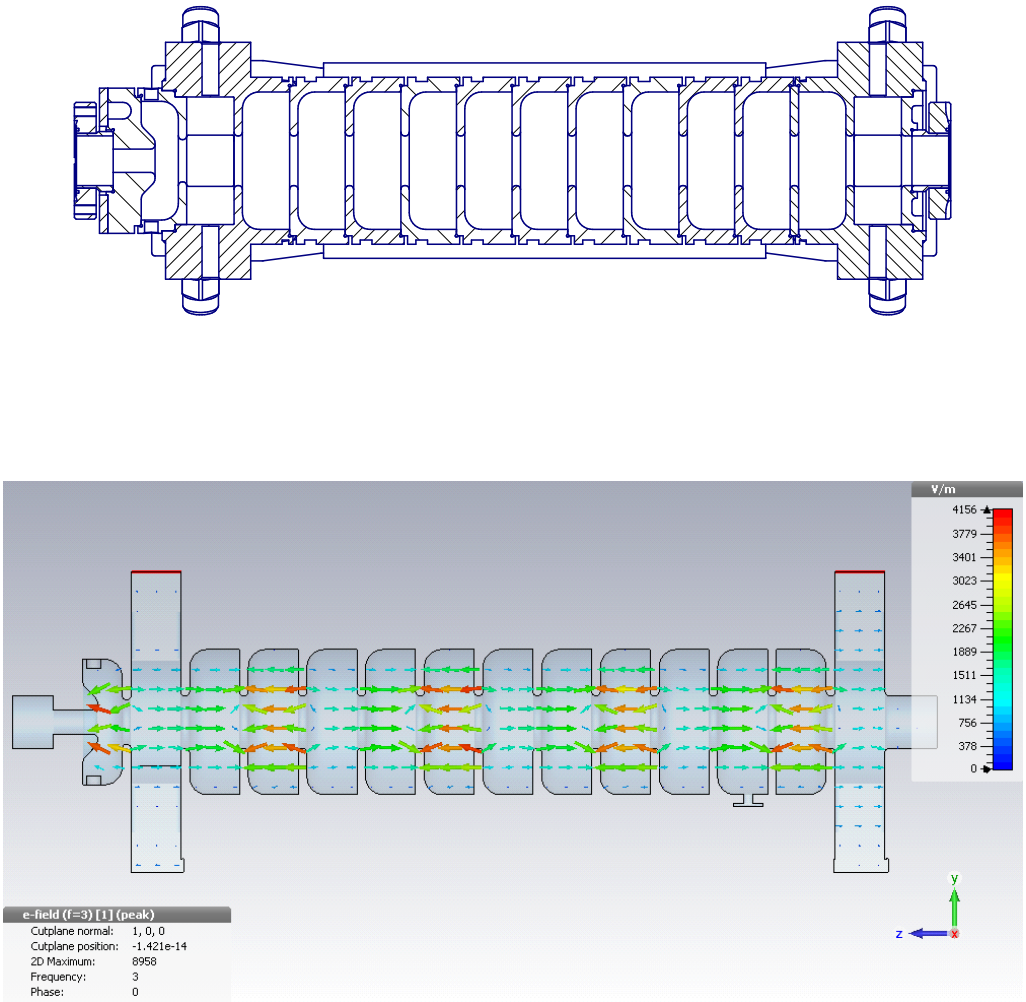

Figure 3.5: Drawing of the hybrid buncher structure and the field distribution calculated by the CST Microwave Studio tool.

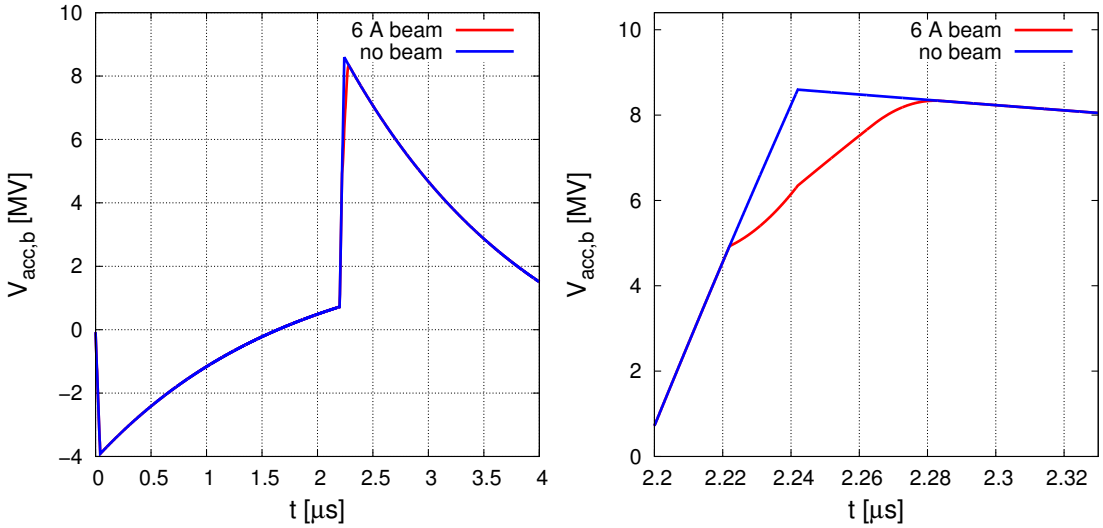

Figure 3.6: Total accelerating voltage for the buncher structure and SLED pulse with (red) and without 6 A beam passing the structure (blue). Plot (a) shows the overview of the pulse and in (b) the instant when the beam passes the structure can be seen in detail.

by the blue curve in figure 3.6. The red curve shows the voltage for the beam loaded structure. Even by considering transmission of the full 6 A beam current and reducing P_0 to 8 MW the voltage is still rising from 5.0 MeV to 6.4 MeV. Hence in practice one would adapt the form of the phase jump such that a slower rising of the rf power is achieved. For $P_0 = 20$ MW electrons with a kinetic energy of up to 13.6 MeV are generated. At that energy hardly activation is to be expected from lost particles before injection into section #2 and thus energy filtering in the magnetic chicane does not cause problems due to activation.

3.2.5 Feed forward

As a simple input function for beam loading compensation by means of a feed forward, a superposition of two rectangular functions has been chosen. When the rf is switched on, the power rises to a value P_1 and is increased to the higher value P_0 during the 4 μs duration of the rf pulse. For the example $P_1/P_0 = \frac{1}{2}$ input power and accelerating voltage in the buncher structure are shown in figure 3.7.
In principle more complex functions can be considered. For example rf power can be switched to P_0 while the accelerator section following the buncher structure is filled. Then the power is reduced to P_1 for one buncher fill time $T_{a,b}$, before power increases back to P_0 in order to stabilize the accelerating voltage in the buncher

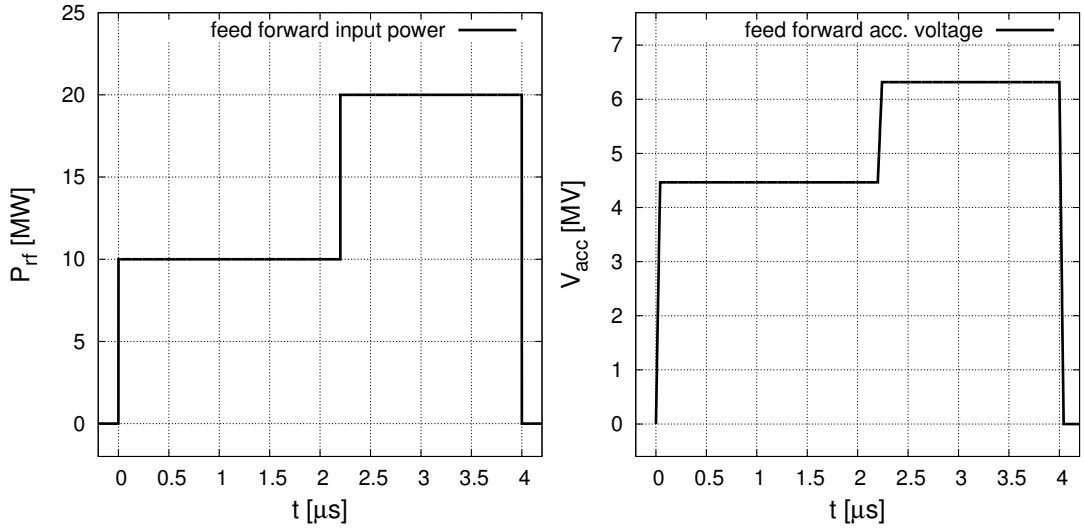

(a) (b)

Figure 3.7: Pulse form and accelerating voltage at the buncher structure with detuned SLED cavity and feed forward.

structure while the beam passes. That way the accelerating voltage in the section does not have to be reduced significantly below 57 MV. Since here only acceleration in the buncher structure is regarded, the simplest function has been used. First for $P_1/P_0 = \frac{1}{2}$ the accelerating voltage has been calculated for beam currents from 1 A to 4 A. The result is shown in figure 3.8 showing how the stability of the voltage depends on the beam current.

With the full $I_{\text{beam}} = 6\,\text{A}$ emitted from the gun, around 4.5 A are to be expected for transmission through the buncher structure. For a beam of such current P_1 has been adapted in order to stabilize voltage. Figure 3.9 shows the obtained accelerating voltage going from $P_1 = 0.1P_0$ to $P_1 = 0.4P_0$ in the left plot. Stable accelerating voltage while the beam passes the structure is achieved for $P_1/P_0 = 20\%$. Since usually rf power above the design value is possible with $P_0 = 25\,\text{MW}$, the right plot presents the results for the higher rf power. In this case the optimum value for P_1 lies between $0.2P_0$ and $0.3P_0$. The remaining change of the accelerating voltage is sufficiently low to transmit the full beam pulse through the energy filter and an electron energy of above 5 MeV is still achievable.

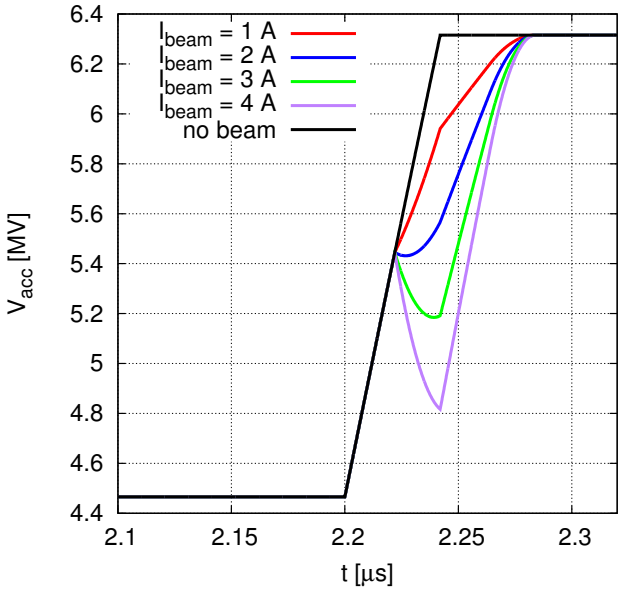

Figure 3.8: Total accelerating voltage for the buncher structure, using a feed forward for rf power, for different beam currents.

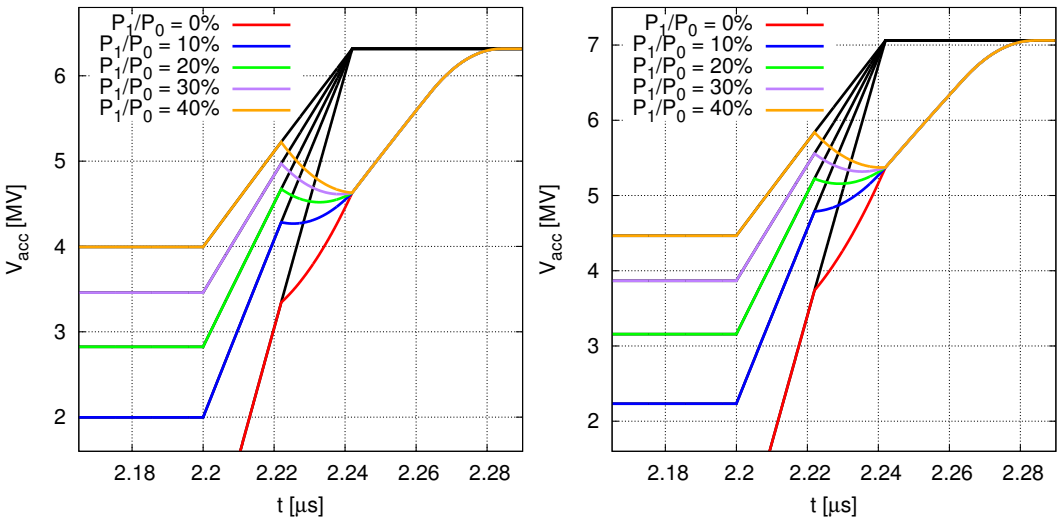

Figure 3.9: Total accelerating voltage for the buncher structure with detuned SLED cavity and feed forward at 4.5 A beam current. Results for varying P_1 are shown with $P_0 = 20$ MW in (a) and 25 MW in (b).

3.3 Beam optics and steering

The path of a charged particle i.e. an electron with transverse position x and momentum x' related to the design orbit through a magnetic field can be calculated using a matrix formalism in case of linear optics. For dealing with a lot of particles it is reasonable to switch to matched optical beam parameters, which can be calculated from the particle distribution. They can be tracked along the orbit by means of the same matrices for accelerator components as explained below.

3.3.1 Magnets

As a start the influence of the used magnet components must be investigated. In contrast to the old bombarder gun injection system, the new injector needs magnets besides focusing solenoids and small correction coils, i.e. quadrupole magnets capable of focusing particles accelerated in the buncher's rf field, and dipole magnets for deflection of the electron beam. The following briefly explains how the behavior of an electron beam tracked through those fields can be treated theoretically. More details can be found in [9].

Dipole magnets

A constant field of dipole magnet forces the incoming particle on a circular path of radius R. For simplicity all dipoles for the new injection system are manufactured identically. In order to avoid edge focusing the pole shoes have a pentagonal shape, such that the field edge lies perpendicular to the incoming and outgoing design orbit, thus forming a sector dipole magnet. The coils could be taken from spare correction coils of the secondary linac. The dipole strength is given by

$$\frac{1}{R} = \frac{e}{p} B_y, \tag{3.6}$$

where p is the particle momentum and B_y the magnetic field in y-direction. With the used dipole magnets the orbit of an electron with exactly 5 MeV kinetic energy the necessary deflection angle of 28° is reached at a magnet current of 6.43 A. Even at the highest usable magnet current, the magnetic field in the iron components of the magnet is not saturated. Hence with prior degaussing, the magnetic field is proportional to the magnet current, which can be used for calculation of the particle momentum.

Quadrupole magnets

Small quadrupole fields are used for focusing of the beam between the buncher structure and the main accelerator sections. They are focusing in one plane and defocusing in the perpendicular plane. The quadrupole strength k is expressed by

$$k = \frac{e}{p}\frac{dB_y}{dx} \tag{3.7}$$

Table 3.2 gives a list of all magnets installed in the new injection system. The magnet names correspond to the notation in the overview shown in figure 3.2.

name	type	z pos./mm
Y2SOL0.2	solenoid	149
Y2SOL0.3	solenoid	287
Y2SOL0.4	solenoid	453
Y2SOL0.5	solenoid	507
Y2SOL0.8	solenoid (klystron focus field coils)	819
Y2D1.8	dipole	1967
Y1D2.8	dipole	3095
Y2Q1.2	quadrupole	1256
Y2Q1.5	quadrupole	1706
Y2Q2.4	quadrupole	2534
Y1Q3.5	quadrupole	3624
Y1Q3.8	quadrupole	3784
Y2CX0.4, Y2CY0.4	steerer hor./vert.	409
Y2CX1.5, Y2CY1.5	steerer hor./vert.	1490
Y1CX3.8, Y1CY3.8	steerer hor./vert.	replaced
Y2CX1.7	steerer (Fe)	1807
Y1CX2.9	steerer (Fe)	3260

Table 3.2: List of all used magnets for focusing, steering and bending. The exact z coordinates refer to the distance from the cathode to the center of the magnet.

3.3.2 Transfer matrices

The simplest case is a 2×2 transfer matrix $\boldsymbol{M}$ of a beam component in one plane. Expansion to 6×6 matrices is possible in case of correlation between horizontal and vertical plane and dispersion. The matrix

$$\boldsymbol{M} = \begin{pmatrix} m_{11} & m_{12} \\ m_{21} & m_{22} \end{pmatrix} \tag{3.8}$$

is the transfer matrix for transformation of particles with $(x, x')^T$ moving in the x-s-plane. For a drift space of length L transformation is done by the matrix

$$\boldsymbol{R}_{\text{drift}} = \begin{pmatrix} 1 & L \\ 0 & 1 \end{pmatrix}. \tag{3.9}$$

For a sector dipole magnet of length s the horizontal transfer matrix is

$$\boldsymbol{R}_{\text{dp}} = \begin{pmatrix} \cos\frac{s}{R} & R\sin\frac{s}{R} \\ -\frac{1}{R}\sin\frac{s}{R} & \cos\frac{s}{R} \end{pmatrix}. \tag{3.10}$$

In case of a quadrupole magnet, the beam is transferred by

$$\boldsymbol{R}_{\text{focus}} = \begin{pmatrix} \cos\sqrt{k}l_Q & \frac{1}{\sqrt{k}}\sin\sqrt{k}l_Q \\ -\sqrt{k}\sin\sqrt{k}l_Q & \cos\sqrt{k}l_Q \end{pmatrix} \tag{3.11}$$

in the focusing plane and by

$$\boldsymbol{R}_{\text{defoc}} = \begin{pmatrix} \cosh\Omega & \frac{1}{\sqrt{|k|}}\sin\Omega \\ \sqrt{k}\sinh\Omega & \cosh\Omega \end{pmatrix} \tag{3.12}$$

in the defocusing plane with $\Omega = \sqrt{|k|}s$.

3.3.3 Transformation of optical beam parameters

If, instead of individual particles the total beam is to be investigated as a collective of particles, one can switch to a method of calculation as explained in the following. More detailed descriptions and derivations can be found in most general accelerator physics books, as for example [9, 16]. The equation of motion

$$x''(s) - k(s)x(s) = 0 \tag{3.13}$$

for the particle trajectory $x(s)$ along the design orbit is used as a starting point. The solution is a transversal oscillation around the orbit, depending on the position s, and is called betatron oscillation. If an approach to solving the problem of the form

$$x(s) = Au(s)\cos[\Psi(s) + \Phi] \tag{3.14}$$

is used, for $u(s)$ a non linear differential equation is obtained, that can in general not be solved analytically. Thus the beam optics is treated usually by means of matrix transformation like the particle trajectory. One utilizes the beta function

$$\beta(s) := u^2(s), \tag{3.15}$$

which is related to the trajectory, emittance ϵ and the phase $\Psi(s)$ as follows:

$$x(s) = \sqrt{\epsilon}\sqrt{\beta(s)}\cos[\Psi(s) + \Phi], \tag{3.16}$$

$$\Psi(s) = \int_0^s \frac{d\sigma}{\beta(\sigma)}. \tag{3.17}$$

The limit of the transversal particle movement is defined by the envelope

$$E(s) = \sqrt{\epsilon\beta(s)}, \tag{3.18}$$

by means of which the beam size can be obtained, if emittance and beta function are known. In most cases the beam profile is approximately Gaussian. Thus the rms beam size will be used, as well as rms emittance. Emittance is a quantity that is conserved during beam transport according to Liouville's theorem under certain conditions, in particular if interaction between the particles (collective forces) can be neglected, and can be understood as the volume in phase space occupied by the beam particles. It is sufficient to transfer the beta function piecewise through the beam transport system in order to specify the beam dimension for any location s. In order to calculate the emittance independently from energy the normalized emittance is defined as

$$\epsilon_n = \gamma\beta\epsilon \tag{3.19}$$

Parameters derived from the above mentioned are

$$\sigma(s) = \sqrt{\epsilon\beta(s)}, \tag{3.20}$$

$$\alpha(s) := -\frac{\beta'(s)}{2}, \tag{3.21}$$

$$\gamma(s) := -\frac{1+\alpha^2(s)}{\beta(s)}. \tag{3.22}$$

The Twiss parameters $\beta(s)$ and $\gamma(s)$, which are not to be mistaken for the relativistic parameters β and γ, can be combined to the beam matrix

$$\boldsymbol{\sigma} = \epsilon \begin{pmatrix} \beta & -\alpha \\ -\alpha & \gamma \end{pmatrix}, \tag{3.23}$$

that then can be transported through the beam line by means of the transfer matrices of the beam line components in the following way

$$\boldsymbol{\sigma_1} = \boldsymbol{M}\boldsymbol{\sigma_0}\boldsymbol{M^T}. \tag{3.24}$$

Alternatively the parameters combined in a vector $(\beta, \alpha, \gamma)^T$ after transformation can be calculated to

$$\begin{pmatrix} \beta \\ \alpha \\ \gamma \end{pmatrix} = \begin{pmatrix} m_{11}^2 & -2m_{11}m_{12} & m_{12}^2 \\ -m_{11}m_{21} & m_{11}m_{22} + m_{12}m_{21} & -m_{22}m_{12} \\ m_{21}^2 & -2m_{22}m_{21} & m_{22}^2 \end{pmatrix} \begin{pmatrix} \beta_0 \\ \alpha_0 \\ \gamma_0 \end{pmatrix}. \tag{3.25}$$

3.4 Beam diagnostics

Transmission, simplicity and high reliability are most essential for the operation of the modified Linac II. Hence the possibility of measurement and archiving of beam current and beam position and their drift during a longer period of operation was regarded essential. Additionally the possibility of investigating optical beam parameters, for example by means of a quadrupole scan, was considered. The diagnostics components are briefly presented in the following.

3.4.1 Button BPMs

For beam position measurement four button BPMs are used. Their design corresponds widely to the BPM developed for the XFEL, only the vacuum chamber has been modified. The four buttons per BPM are arranged pairwise in the horizontal and vertical plane respectively. A mechanical drawing is presented in section 5.3 together with calibration data. As shown in figure 3.2, one BPM is located between buncher structure and the first dipole magnet and another one in the magnetic chicane. Both are located close to quadrupole magnets in order to help steering the beam through their center and thus to avoid deflection. Two further BPMs are needed in front of the termination/accelerator section and hence on the axis defined by the Linac II accelerator structures. By means of these two BPMs the direction of the beam can be optimized for the transmission through the primary accelerator and the positions are recorded. A possible drift of the buncher phase during longer periods of operation, changing energy and deflection angle in the magnetic chicane, can be corrected by scanning the phase and therewith retrieving the correct positioning. The associated BPM electronics evaluates the extracted signal at 2.998 GHz for obtaining the necessary data. Hence the beam position can only be measured with rf power coupled into the buncher structure, engraving the rf structure to the beam pulse. A precision of 100 μm was aspired, which was considered sufficient for identifying beam position drifts causing particle loss during operation of the linac.

3.4.2 Pneumatically driven fluorescence screens with Faraday cup

Two fluorescent screens are used in the injection system test stand. They are located straight behind the first dipole magnet and directly in front of the second dipole

magnet in the magnetic chicane. Two further identical screens are foreseen for the second new designed beam line for operation of the bombarder gun. In order to move the screens into the beam path, pneumatically driven movers are used. The application of a step motor for stepwise movement of the screens was considered unnecessary, hence the screen can only be moved out or in to a preset position. Besides the DN40 flanges for the beam tube, four flanges are available at the vacuum chamber of which one is unused, one is used for the mover, one for the observation window and a bigger DN100 flange for ultra-high vacuum (UHV) generation by an ion getter pump. The observation takes place by a plane mirror and a camera, equipped with an adaptable aperture and objective lens for setting of magnification and brightness. For illumination of the chamber's interior, the window is equipped with LEDs and its inner side is coated completely with a copper mesh-work. This is supposed to prevent vacuum leaks, that can occur due to electrical charge collected by the window and causing cracks in the material. Such cracks appeared during test operation before the mesh-work was added. In order to minimally limit the sight on the screen through the window by reflections of the copper surface, it has been oxidized by heating to black copper(II) oxide. The screens themselves consist of thin aluminum plates of size 30 mm × 30 mm and are yttrium aluminium garnet (YAG) coated. Alternatively zinc sulfide coated screens are available.
The screens are as well usable as a Faraday cup. Therefore the coated aluminum plate is fixed on a copper block, isolated from the mover's holder by a ceramic. Discharging takes place through a wire, which is guided to the outside of the mover flange via a vacuum feed through, where voltage can be measured. However the screens are mainly planed for beam profile measurement. Carrying out a quadrupole scan, the optical beam parameters, i.e. emittance and beta function, can be determined as will be described in section 6.2.1.

3.4.3 Beam current monitoring

Except for the above mentioned beam current measurement using the screens, behind the buncher structure a foldaway inductive current monitor of type Fischer F-80-1 is used. Two more of this model are going to be installed in the straight bombarder gun beam line. It possesses a bandwidth of up to 100 MHz, a sufficiently high inner diameter of 127 mm for the ceramic of the associated vacuum chamber and can be installed and removed independently from the vacuum chamber due to the foldability. In early tests of the triode gun, a Bergoz FCT-122 was used.
For termination of the beamline another Faraday cup is installed in the test stand. When the new injection system will be installed as electron source for the Linac II, to measure beam current at this position, a Pearson inductive current monitor, at present installed between section #1 and section #2, will be left in place. Additionally before commissioning in the Linac II, a resistive wall current monitor is going

to be added between the triode gun and the buncher structure. Since installation of the buncher structure, beam current measurement directly behind the gun was not possible anymore because the necessary vacuum chamber with a ceramic gap was not ready yet. This deficit will therewith be repaired.
During tests beam current values could be determined with an accuracy better than 20 mA. In case of short beam pulses the precision of beam current measurement is limited due to the rise time of the signal. The manufacturer specifications are given in [52, 53]. During the test stand operation charge measurement using the Faraday cup of the screens was very important. Even though oscillations of the current occur, charge measurement is not affected. For an individual beam pulse, the statistical error for the measurement is mainly determined by the used ADC (analog-to-digital converter). Some issues with respect to the calibration of the Faraday cup, such as reflection from the surface, are considered in section 5.2.2.

3.5 The vacuum system

In order to achieve a UHV vacuum of $\sim 10^{-8}$ mbar, six ion getter pumps are installed alongside the new injection system, i.e. at the gun chamber, the prebuncher, the buncher structure and the screen vacuum chambers. Additional pumps are installed along the waveguides. The system is divided into three sections, separated by vacuum valves, which contain the gun (1st vacuum section), the prebuncher, buncher and vacuum chamber till screen #1 (2nd vacuum section) and the remaining beam line including the adjacent accelerator section (3rd vacuum section). For separation of the 2nd and the 3rd section the waveguide connecting the buncher structure with the accelerator section had to be equipped with an rf window, capable of sustaining 50 MW peak rf power. In the 1st vacuum section the UHV conditions must be kept even during maintenance periods, if a functional cathode is installed. Otherwise the capability of emission can be lost. Therefore, the cathodes are delivered in a evacuated recipient which is opened only for activation in the gun. For storage a pressure below 10^{-3} Torr must be ensured, according to the manufacturer's instructions [26].

Chapter 4

Simulations

4.1 Particle tracking with ASTRA

For the discussed types of injection for the Linac II (status quo with bombarder gun and new injection with triode gun), the expectations of performance were determined by particle tracking with ASTRA. ASTRA is an algorithm for tracking of arbitrary distributions of charged particles through electromagnetic fields. It is of great use when consideration of space charge is important, as in the case of designing injection systems where electrons are tracked from emission at a cathode to the main accelerator. Its functionality and physics are well described in [32].

In the following, results for the two different injection systems are shown. Particle lists were generated appropriate to the size of the cathode, the pulse length and charge desired for the respective analysis. Since space charge is taken into account, two aspects concerning the length must be considered. The first is bunching in not completely filled rf buckets and the second is missing space charge forces in front and rear of the pulse, if only one bucket is supposed to be filled. While for optimization it is often useful to use pulses shorter than one 3 GHz rf bucket, for the presented results pulses which correspond to the emitted beam must be used. Since even the shortest experimentally available pulse length of 2 ns equals six rf periods, such long pulses must be used in the simulation unless compression into only one bunch for each 333 ps pulse length is provided. However ASTRA offers options to discard debunched particles, i.e. particles with a distance to the bunch center, exceeding a specified multiple of σ_z, are passivated for further calculation.

The necessary electric and magnetic field data for the components were generated with the software CST Studio [54] or the Poisson/Superfish simulation tool [55]. For quadrupole magnets and dipole magnets, ASTRA does not accept external field data, but uses analytical field profiles, that can be found as well in [32]. Therefore a few parameters can be specified, which were used to match the field to the profile

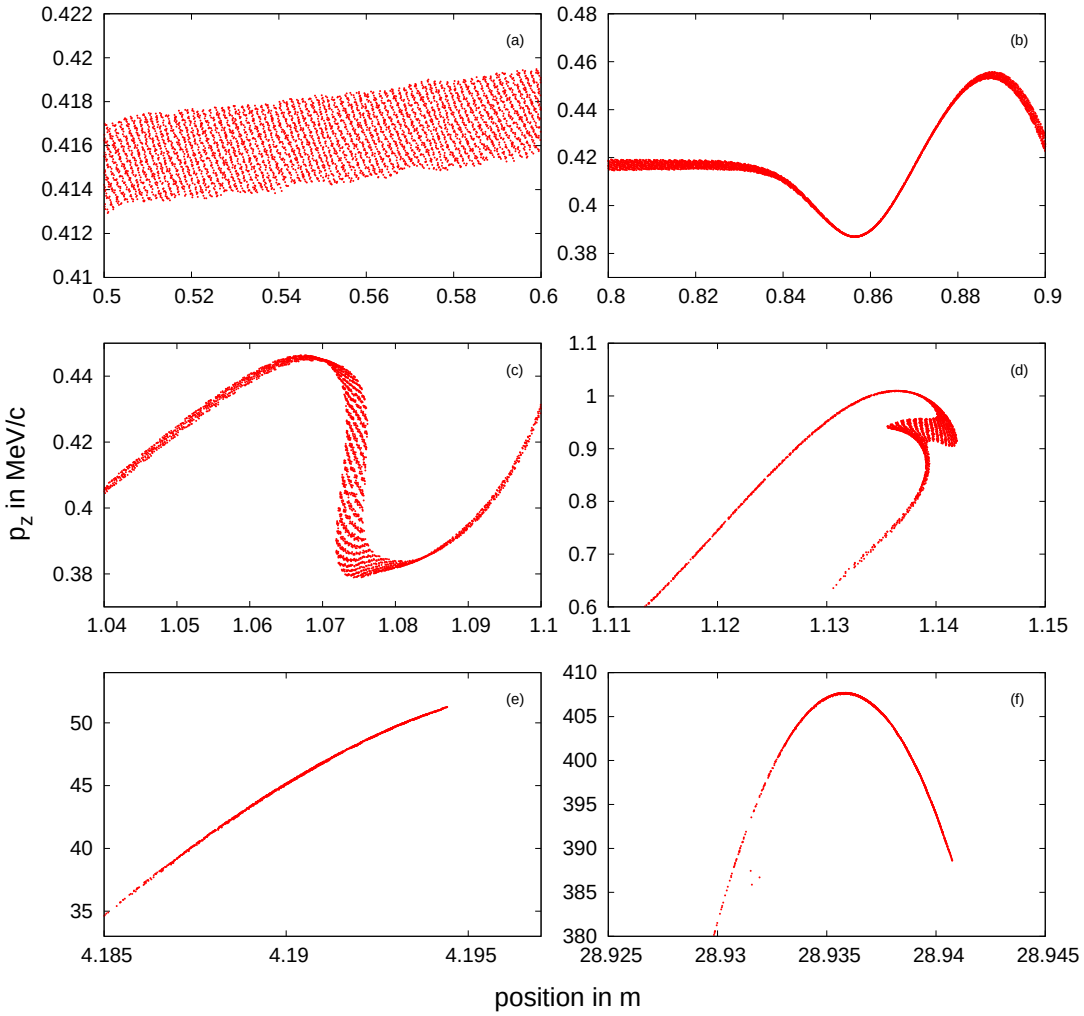

Figure 4.1: Particle distribution from ASTRA in longitudinal phase space for status quo injection system: (a) after emission, (b) at the prebuncher, (c) before injection into section #1, (d) during electron capture in the first cells, (e) off-crest accelerating at the end of section #1, (f) in fron of the converter.

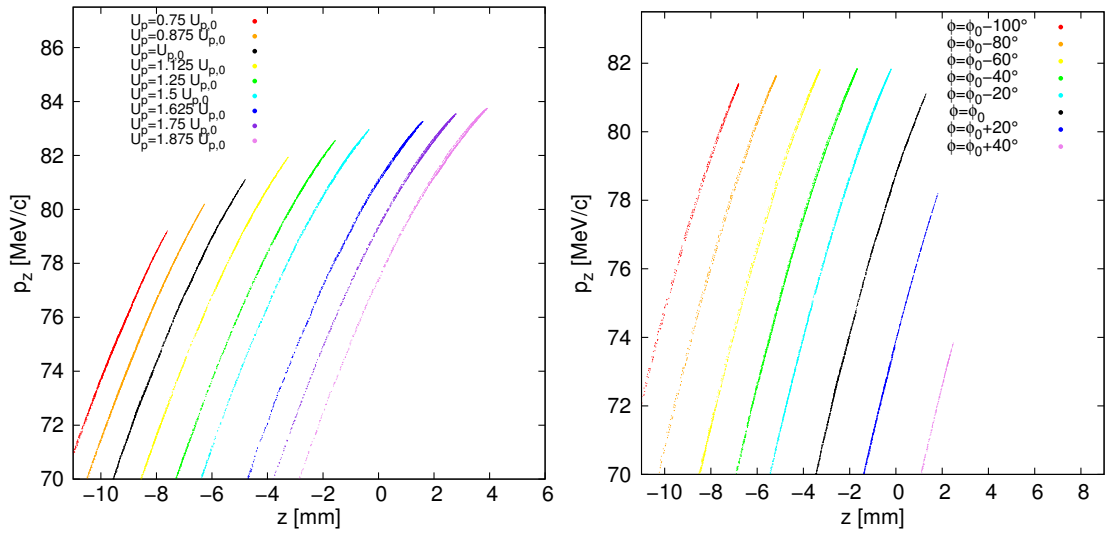

Figure 4.2: Particle distribution in longitudinal phase space for prebuncher amplitude (a) and section #1 phase (b) scans. Acceleration on the crest of the field is not reached. For highest deviations the number of particles transmitted through section #1 drops by 15%.

that was obtained from field profile measurements. Apertures were included for the gun anode, the beam tube and the iris apertures of the buncher's capture cell and the traveling wave cells.

In the optimization process transmission through the system and through the linac sections was maximized by changing all variable parameters, i.e. magnetic field strengths, amplitude and phase of the rf fields and in case of the new injection system the positions of components. The gun HV remained constant. Aside from initial manual setting to reasonable values, scans were carried out sequentially for the available parameters and repeated in several iterations. If the procedure did not yield the required result, selected parameters were changed manually for further scans.

4.2 Unmodified Linac II

Figure 4.1 shows several particle distributions in longitudinal phase space along the injection system and the Linac II. The first plot shows the particle distribution right after emission and acceleration by the gun HV of 150 kV. The slight rise of kinetic energy along the z-axis is due to space charge effects in the pulse of limited length.

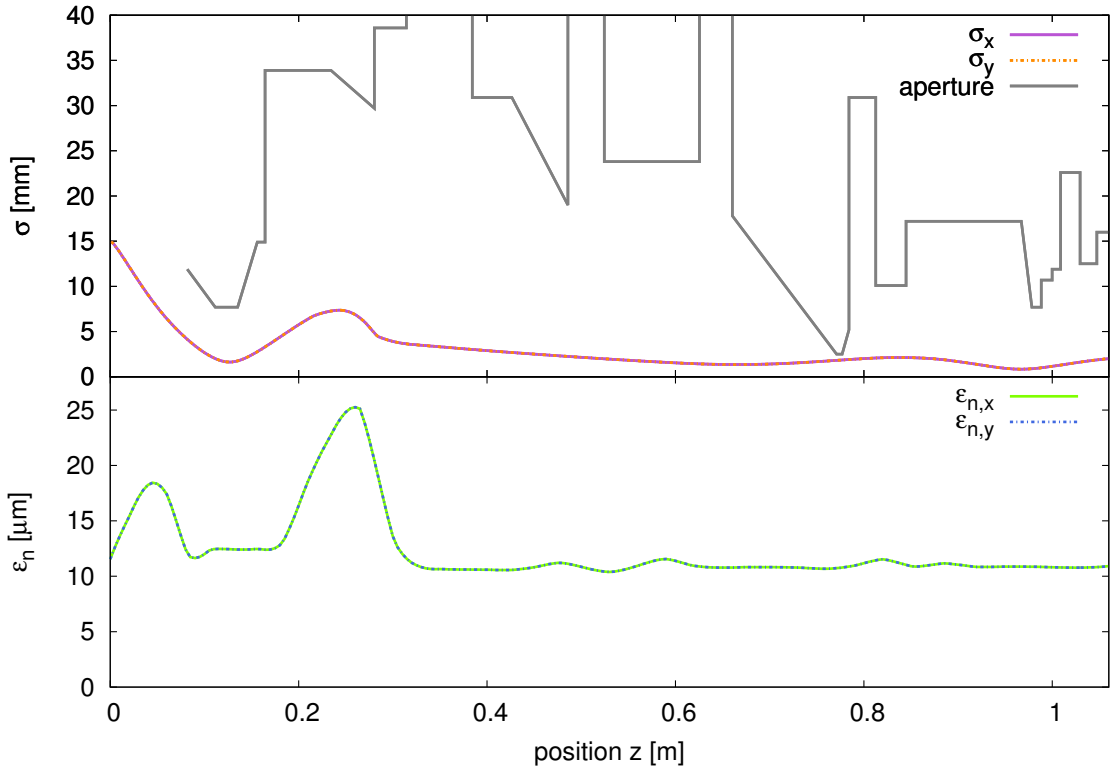

Figure 4.3: Normalized emittance and rms beam size of a particle distribution tracked from bombarder gun cathode to section #1.

In the next plot the impact of the prebuncher can be seen, that was applied with a total accelerating voltage of $U_{p,0}$=18.5 kV in this case. The slightly overbunched beam right before injection into the first accelerator structure of the linac is shown in plot (c). Formation of the bunch after acceleration by the structure's first cell is shown in the adjacent plot. The length of this first cell is not matched to the electron velocity of $v_e = 0.63c$. Thus off crest acceleration takes place in the main part of the structure as shown in plot (e) with higher energy spread as a result. This problem of the present bombarder gun injection system is approached in the new injection system by the short β-matched capture cell and the energy filtering in the magnetic chicane. In the four remaining accelerator structures the phase is set to on-crest acceleration for the purpose of reaching the maximum energy.

In order to demonstrate the off-crest acceleration due to the missing capture cell, figure 4.2 shows particle distributions in longitudinal phase space while scanning the prebuncher amplitude (left plot) and section #1 phase (right plot). The distribution for the amplitude $U_{p,0}$ and phase ϕ_0 found in the manual optimization are painted in black. These values from the optimization described in the previous section yielded the minimal particle loss at high energies for reasonable values of beam current and energy. For rising amplitude, the maximum energy within a particle distribution

is rising, but transmission through the section diminishes. The distribution with the highest shown amplitude contains 15% less particles. In case of the phase scan a similar result is obtained. With $\phi = \phi_0 - 20°$ the maximum energy within the distribution is highest, but transmission is slightly lower than for ϕ_0. For even lower phases the trend of decreasing transmission persists. Overall, during the optimization the missing capture cell could not be compensated by adapting the field in the prebuncher and section #1. The presentation of the particle distribution in the longitudinal phase space for the new injection system, which follows in section 4.3, verifies that the problem does not occur in the buncher structure. Thus by means of the new bunching system with a capture cell, lower energy spread, higher average energy and shorter bunches are to be expected.

4.2.1 Emittance and beam size in the injection system

For Linac II operation a minimized emittance is not directly essential, especially in positron operation. But due to its conservation and the dependency of beam size from emittance and beta function by

$$\sigma(s) = \sqrt{\epsilon\beta(s)} \tag{4.1}$$

it is desirable to achieve an emittance below the threshold where losses on apertures occur. During beam transport from the buncher structure to the adjacent linac section quadrupole magnets are used for focusing and hence the beta function becomes larger in the respective plane of defocusing. The optics has to be chosen such that losses due to high emittance and high beta function do not reduce the overall transmission below the value needed for sufficient positron generation. Beam size and normalized emittance development calculated with ASTRA for the present injection system are shown in figure 4.3. The high starting rms beam size is given by the large cathode surface with a radius of 30 mm. For normalized emittance calculation the option in ASTRA for neglecting the solenoid fields has been deactivated, which corresponds to the default settings. Even though emittance is conserved according to Liouville's theorem, the calculated emittance for the tracked particles shows changes. This has a number of reasons originating from the way the emittance is computed. One reason is the non-local calculation. Instead the calculation takes place for certain time steps. Hence when external fields act onto the beam, correlated emittance growth occurs, because the head has traveled a longer path in the field. For the non-local emittance parts of the raised emittance can remain. In drift space this remaining correlated emittance growth can be avoided by calculating the projected emittance, which has been done in the presented data. It is reversible and does not violate Liouville's theorem. A very detailed theoretical description on this topix is given in [56]. Reasons which are not due to computation but do cause

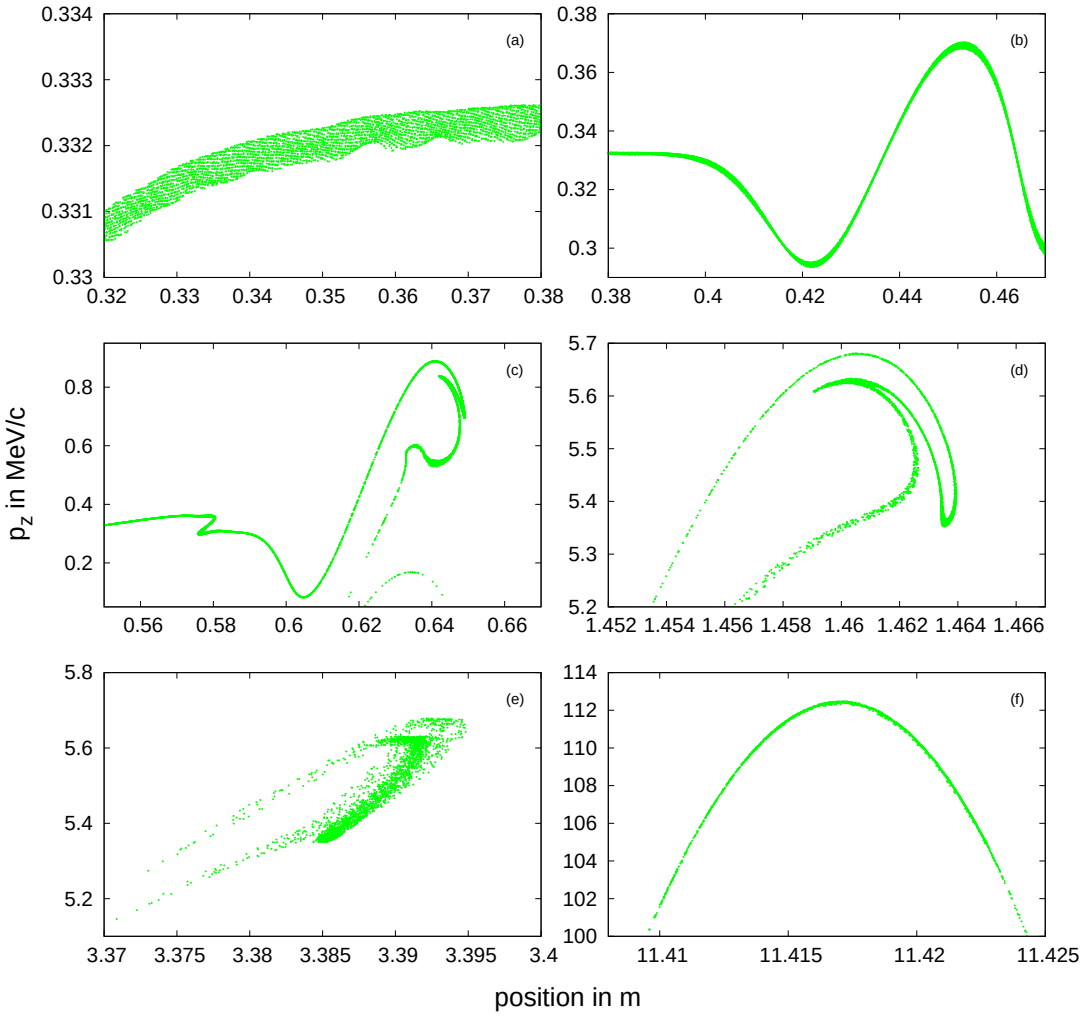

Figure 4.4: Particle distributions in lognitudinal phase space computed with ASTRA for the new injection system design: (a) gun, (b) start prebunching, (c) electron capture in the buncher structure, (d) behind the buncher, (e) energy filtered beam, (f) on crest acceleration in linac structures.

change of emittance are space charge and loss of particles. Space charge affects the beam, in particular from emission at the cathode to injection into the first accelerator structure. Influence of particle loss has been avoided by taking only transmitted particles into account. In addition, only particles within a single bunch have been taken into account for normalized emittance calculation. That way influence of the mentioned external fields on the computed values is limited to a short length.

4.3 Tracking through the new injection system

The results given above for the bombarder gun injection system have been compared to the results from an optimization in ASTRA for the new injection system, presented in the following. Figure 4.4 shows the particle distribution in longitudinal phase space for six positions along the new injection system and the linac. An identical prebuncher field is used with marginally lower amplitude. The bunch arrives slightly overcompressed to a length of 5 mm at the capture cell at $z = 0.58$ m. In the following cells it is accelerated on the right phase for further bunching. Its tail is lost in the energy filter. Injected into the linac the bunch is accelerated on the crest of the field.

The evolution of beam size and normalized emittance along the whole injection system until to the adjacent accelerator structure are presented in figure 4.5. As for the data in figure 4.3, all particles are taken into account for the beam size calculation and only the transmitted particles of a single bunch are taken for computation of the normalized emittance. The options in ASTRA for the latter are identical. Since the normalized emittance is shown, the influence of energy gain in the buncher on the emittance is not visible. The beam size becomes minimal for both planes when focused on the aperture of the capture cell. Behind the buncher structure, the rotational symmetry disappears at the first quadrupole magnet and the beam grows wide in the vertical plane because of dispersion after the first dipole magnet. As mentioned above, at magnet positions the projected emittance is raised due to the method of calculation, while only parts of the bunch are located in a magnetic field. In the vertical plane a correlated emittance growth shows up from the first dipole magnet because of the correlation between transverse particle position and energy. As derived in [56] this growth is in principle reversible and does not violate Liouville's theorem because it does not show up in the six dimensional phase space volume.

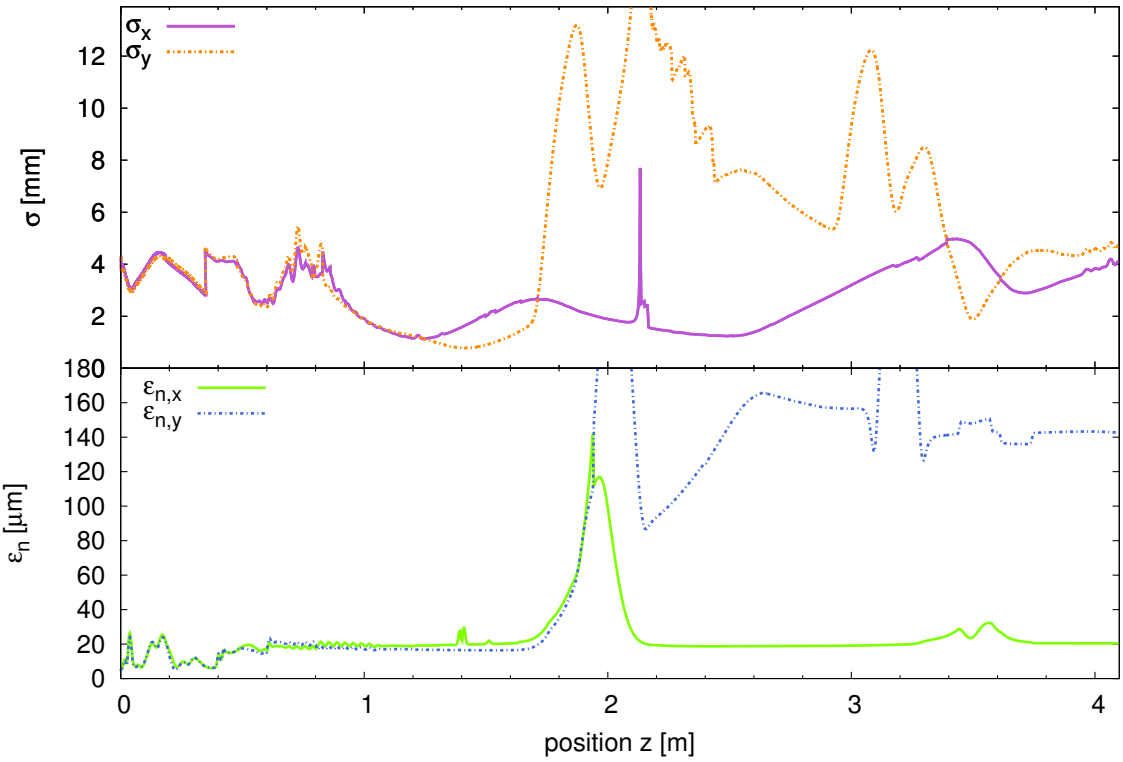

Figure 4.5: Beam size and normalized emittance development through all external fields of the new injection system from gun to injection into the main linac.

4.4 Primary linac performance comparison

4.4.1 Beam loss at high energies

In order to compare the performance of the old and the new injection system in terms of particle loss and hence activation of the linac, the loss in particle tracking has been investigated. Comparisons have been made for differing assumptions relating to beam loading induced transient accelerating voltage in the respective accelerator structures.

At first optimization of particle transmission has been done for a single bunch and without considering beam loading. Figure 4.6 presents the achieved performance for both injection systems as a histogram. The fraction of lost particles is plotted vs. energy intervals of 5 MeV size for a tracked bunch that consisted of 200,000 macro particles. In all loss histograms, the results for the new injection system are indicated by green bars and by red bars for the status quo injector. In order to emphasize the lower loss per bin at high energies compared to the high loss at the injection a logarithmic scale is used. In both cases the losses above 10 MeV do not exceed 0.1%, i.e. 200 macro particles. This result is not satisfying yet, because

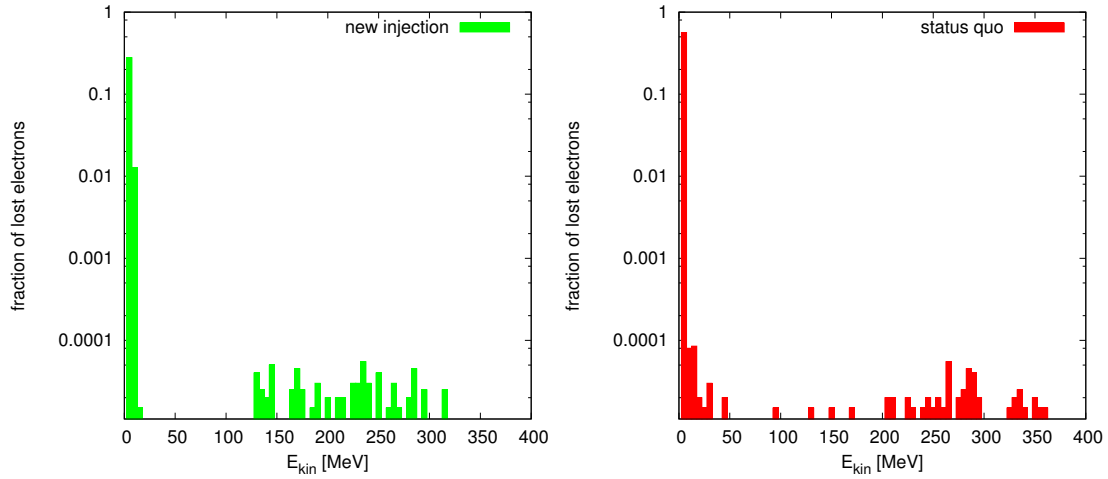

Figure 4.6: Beam loss for run with single bunch, i.e. without consideration of beam loading, in the Linac II sections with the new injection system (a) and the status quo bombarder gun injection system (b).

no reason for the loss in the Linac II can be identified. Thus multi-bunch energy spread must be taken into account. Its origin is beam loading, playing an important role at the used high pulse charge. It can be taken into account using the transient accelerating voltage, which includes the beam induced field and has been calculated in section 3.2.3 for the buncher structure and in section 2.3.1 for the linac sections.
As a comparison to the single bunch tracking, the tracking has been repeated with dropping accelerating voltage in the accelerator structures for consideration of beam loading. The resulting loss for all energy intervals is indicated in figure 4.7 for the new injection system and 4.8 for the bombarder gun injection system. For the accelerator sections an 8% drop of V_{acc} from 80 MV to 73 MV has been assumed according to the calculations in section 2.3.1. The reduction has been carried out in ten equal steps for each of which one bunch has been tracked through the whole primary linac. The shown histogram results from the accumulated losses of all these calculations.
In the left side plots of both figures total compensation of beam loading was assumed for the first accelerator structure, which is the buncher for the new injection system and accelerator section #1 for the bombarder gun injection system. The plot on the right side shows results for the case of dropping voltage in all structures. In that case tracking was stopped after a drop of accelerating voltage in the buncher structure from 5 MV below 4.6 MV, where all particles were lost in the energy filter. Without compensation of beam loading a higher drop is to be expected, as shown in section 3.2. That means, a significant part of the beam pulse will be lost in the

magnetic chicane due to multi-bunch energy spread, if the beam induced voltage is not compensated.

Another reason why the drop of energy from head to tail of the bunch train after the buncher structure needs to be minimized is, that with on average $\beta = 0.9957$ bunches with decreasing energy drift apart before injection into the adjacent accelerator section. Hence not all bunches of the beam pulse are accelerated on the correct phase in the main accelerator. The bunch energy at the converter drops if the buncher accelerating voltage differs much from the optimum value. Here the problem is not yet the differing final energies themselves, but their origin, the wrong phase. It would persist in the secondary linac, where energy spread forms anew, and hinder injection into PIA. For the energy drop from 5.0 to 4.6 MeV, β drops from 0.9957 to 0.9950. For the drift to the section of 3.07 m length, the change in phase is 7.8°. In the last section of this chapter, which discusses capture and transmission of positrons, the problem will be seized by means of phase scans for section #6/7, and the energy spread, that is to be expected in the secondary linac, will be given.

Summarizing, compensation of beam loading is essential for transmission of high current pulses with up to 20 ns length to the converter. As discussed earlier this is achievable for the buncher structure in contrast to the longer accelerator sections. In practice a sufficiently stable voltage in the mentioned range can be a challenge to obtain, as will be discussed in chapter 6. Nonetheless the advantage of low particle loss remains for the new injection system even with dropping gradient. Compared to tracking with stable voltages, small additional loss occurs right behind section #3. This is due to particles leaving the field of the solenoid magnets, enclosing the first three Linac II sections. For the bombarder gun injection system, loss at high energies occurs in the simulations. Due to the lack of energy filtering and the higher energy spread from capturing of the prebunched beam with wrong phase velocity, bunches with much higher energy spread pass the linac sections. Then chromaticity effects at the transitions between the section's focusing solenoid magnets cause loss. With still below 1% at energies above 10 MeV, this loss is still much lower than experienced in operation of the Linac II, but indicates that energy filtering is advantageous. In practice the Linac II is operated with a not entirely filled accelerator section #1, even though beam loading can by far not be completely compensated as discussed earlier. Anyway compensation was assumed in the left plot of figure 4.8. Slightly better performance compared to an entirely filled structure is observed in practice. The reason is that a higher field for beam capture in the first cells is obtained due to the SLED pulse form.

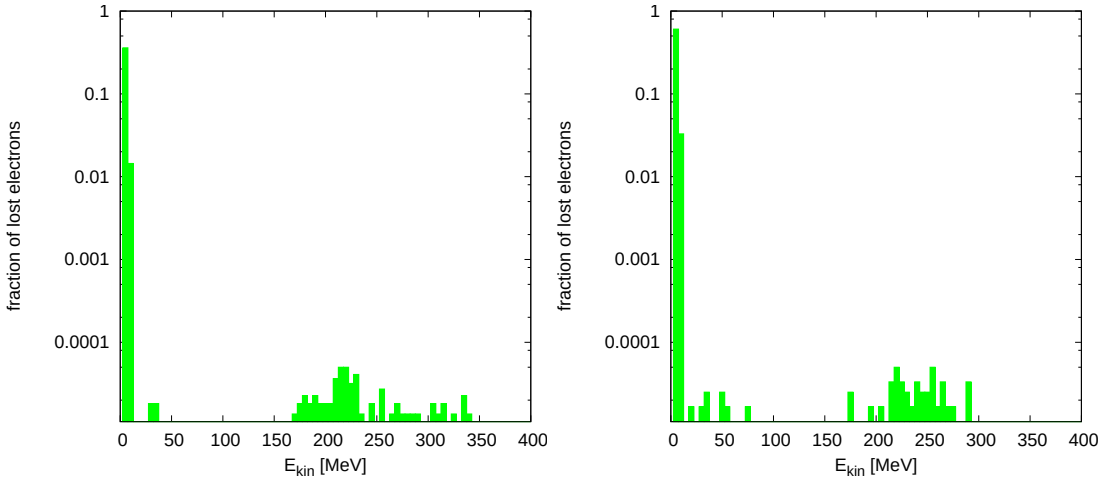

Figure 4.7: Beam loss with diminishing accelerating field for the new injection system. Plot (a) shows loss resulting from runs with constant field in the buncher structure and plot (b) shows loss for diminishing amplitude in all structures, including the buncher.

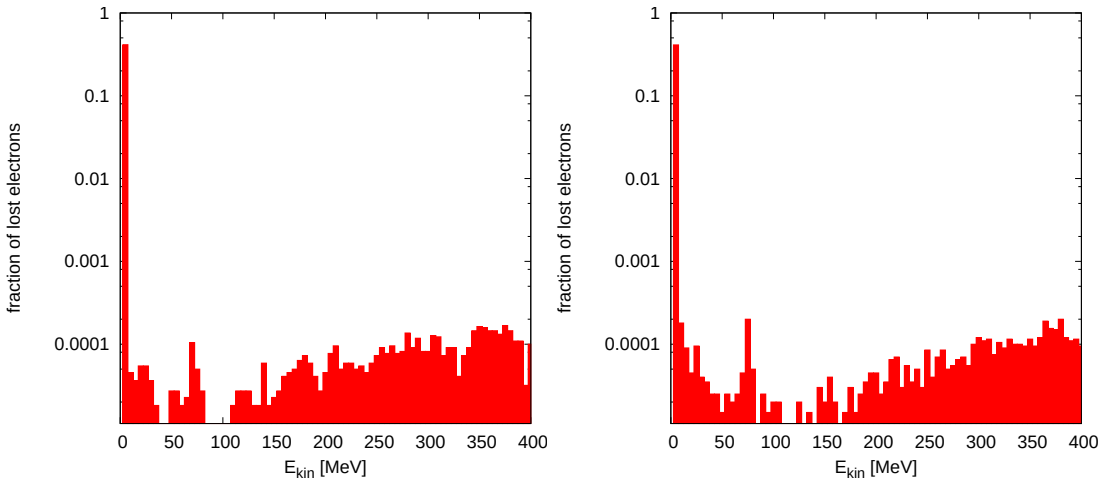

Figure 4.8: Beam loss with diminishing accelerating field for the bombarder gun injection system. Plot (a) shows loss resulting from runs with constant field in section #1 and plot (b) shows loss for diminishing amplitude in all structures.

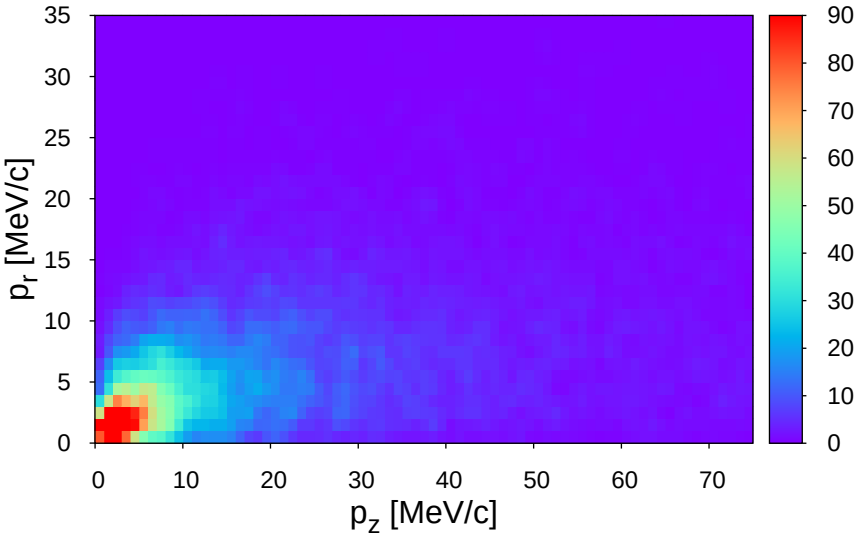

Figure 4.9: Distribution of EGS5 generated positrons in transverse and longitudinal momentum. Most of the highly divergent particles are lost. The scale for particle numbers is in arbitrary units.

4.5 Converter

For investigation of the electron positron converter, the particle showers caused by the electrons in the tungsten target were simulated by means of the EGS5 code [57]. Therefore particle distributions obtained from ASTRA at the end of the primary linac are taken to be imported by the EGS5 code. For each listed macro particle the individual particle momentum and coordinates are taken for evaluation of a particle shower. In case one or more positrons are generated, its coordinates and momentum when leaving the tungsten target are stored in a new file, that ASTRA is capable to read for further tracking of the positrons through the secondary linac.
The resulting positron bunch is strongly divergent with a high energy spread. Figure 4.9 shows the positron distribution in a p_r vs. p_z plot. Obviously most of the positrons will be lost directly behind the converter target. In order to capture as many positrons as possible, solenoid magnets with high fields are used, i.e. a short 1.8 T pulsed coil and 0.4 T solenoids enclosing the accelerator sections #6 and #7, as presented in section 2.5.
For installation of the new injection system the first accelerator structure of the Linac II has to be removed. Thus a lower energy $E_{\mathrm{red}} \approx 320\,\mathrm{MeV}$ is reachable at the end of the primary linac instead of $E_0 \approx 400\,\mathrm{MeV}$. Descriptions of electron positron

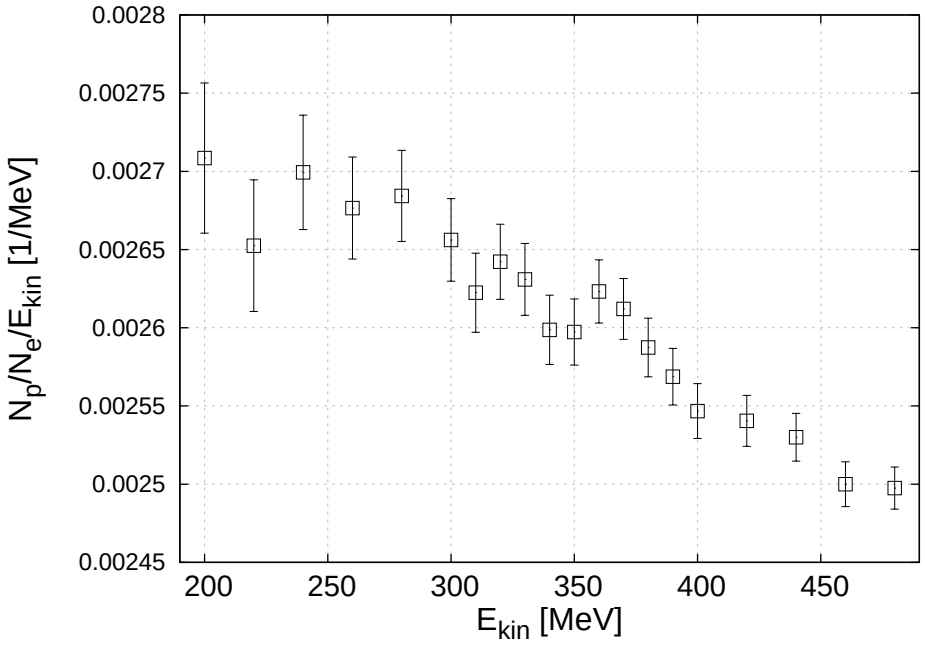

Figure 4.10: Positron rate from EGS5 for different monoenergetic beams. The error bars are based on the number of generated positrons. For lower energies with constant number of incident electrons, less positrons were generated and errors are higher.

converter optimizations are given in [58,59]. According to [59] the optimum thickness for a converter target for beam of energy E is

$$l_W = (1.1 \ln(E[\text{GeV}]) + 3.9) X_W, \tag{4.2}$$

where $X_W = 3.58\,\text{mm}$ is the radiation length for tungsten. Using that equation for a 400 MeV incident beam the optimum length turns out to be $l_W = 10.4\,\text{mm}$. The used thickness of 7 mm yields an optimized thickness for a 170 MeV beam. But when choosing l_W other aspects as for example thermal issues must be considered as well. In order to estimate the expected performance reduction due to lower incident energy, EGS5 computations were carried out for a range of energies. A calculation of the conversion rate for energies from 200 MeV to 480 MeV with EGS5 showed slightly higher positron yield per energy of incident electrons at lower energies. Figure 4.10 shows the conversion rate per MeV vs. kinetic energy of the incident electrons. These results show that instead of a drop of the conversion rate of >20% only a drop of 17% must be expected. The error bars are based on the number of generated positrons. For lower energies with constant number of incident electrons less positrons were generated and errors are higher.

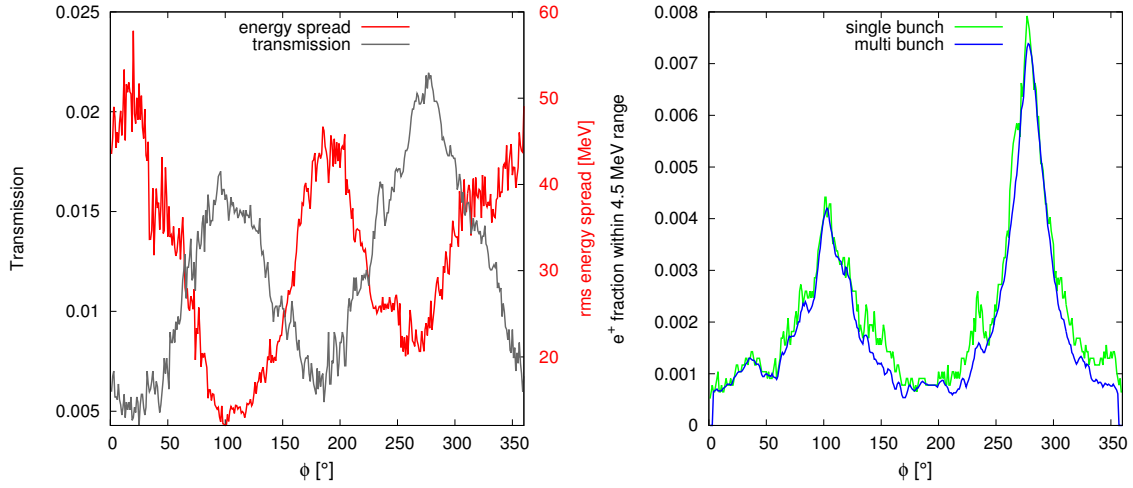

(a) (b)

Figure 4.11: IMA07 position positron rate and rms energy spread vs. phase of section #6 and section #7 of the secondary linac (a). Additionally the fraction of tracked positrons within the for PIA acceptable energy range is shown for a single and for multiple tracked bunches (b).

4.6 Secondary Linac II

Transport of sufficient positrons to PIA is essential for accumulation of high particle numbers. The positron distribution obtained from EGS5 has been tracked with ASTRA through parts of the secondary linac. As an overview of how good positrons are captured according to the simulations a scan of the rf phase in section #6 and section #7 has been carried out. The two plots in figure 4.11 illustrate the result. For their generation a scan with a step size of 1° has been done for the phase over the whole range of 360°. For each point the individual positron distribution behind section #7 has been evaluated. On the abscissa of the left plot both rms energy spread and the fraction of captured positrons are shown. A low energy spread below 0.5% is necessary for injection into PIA at 450 MeV. In the presented case, the rms energy spread is lowest at a phase of ϕ =100°, while transmission is highest at ϕ =280°.

The conversion rate for that phase is 1.9%, which is above the presently measured yield. Dispersion caused by steering can cause a lower conversion rate based on the IMA07 measurement. In normal operation the ratio of positrons injected into PIA to electrons for conversion is approximately 0.4%. Because of the much lower pulse charge, beam loading was neglected in the positron pulse tracking through section #6 and section #7.

Though from the left plot in figure 4.11 it is not clear, if ϕ =280° is the optimum

phase for injection of a maximum number of positrons into PIA. The rms energy spread of 22 MeV is too wide to inject the main part of the particles. Thus the data shown in the right plot has been computed from the particle distributions. It shows the maximum fraction of particles for each individual distribution, lying in any interval of 4.5 MeV width (green curve for single bunch). The given fraction relates to the initial number of positrons. Assuming that further acceleration takes place by the same voltage for all positrons, the computed fraction is the maximum, that can be injected into PIA according to its limited energy acceptance. As explained before, the shift of the phase on which acceleration takes place in the primary as well as in the secondary linac may cause particle loss at the injection into PIA. This problem originates from a non-compensated beam induced accelerating voltage in the buncher structure and the associated drift of the pulse tail to a wrong phase in the linac sections. For analysis of that problem, the multi-bunch curve in the figure 4.11 has been calculated. It shows the fraction of particles calculated the same way as the single bunch curve, but is based on the joined distributions within a 8° interval. For both single bunch and multi bunch evaluation the highest fraction of particles within the usable energy range is at ϕ =280°. The two curves are very close for most phases. Even though two thirds of the positrons transmitted through section #7 would be lost during injection, at that point the phase shift would not limit the particle number significantly.
The required number of particles in PIA depends on the mode of PETRA III operation and in most cases around 10^{10} particles are sufficient. Using the data from figure 4.10, for a usable positron fraction of 0.007 and an electron beam of 2 A, 320 MeV and 20 ns pulse length, the number of injected positrons would be $1.5 \cdot 10^9$. The ratio of electrons on the converter target to positrons injected into PIA is 0.6%. This corresponds to one and a half times the measured ratio. With an accumulation of a few Linac II pulses the required positron rate can be achieved, which stands in agreement with operational experience.

Chapter 5

Construction and commissioning of the new injection system test stand

This chapter discusses the commissioning of the injection system test stand. Starting with preparation of components e.g. the tuning of the buncher structures, followed by calibration of diagnostics and the gun control. The tuning process of buncher #2, for which a stub tuner was available is presented in detail. For buncher #1 that was used in the test stand, the final field curves are presented as well.

5.1 Tuning of the hybrid buncher structures

Before installation of one of the two buncher structures in the test rig it had to be tuned in order to obtain a flat field distribution and the correct phase advance of $2\pi/3$ per cell. Therefore the first step is to measure the field along the axis of the structure. The method of choice is the bead pull measurement, in which a perturbing object (the bead), fixed on a string, is pulled stepwise through the structure. For each step, the field of the reflected wave is measured to obtain the reflection coefficient S_{11}. A summary of the experiences during the tuning of the buncher structure is also available in [60]. The following paragraph explains the theory of how the structure's field distribution can be calculated from that data.

5.1.1 Nonresonant perturbation theory

Reflection coefficient measurement with and without a perturbing object placed at the point at which the field strength is to be measured are made in order to calculate the field. The necessary equations for use in case of cavities which are too lossy to support resonance are derived in [61]. The content is briefly summarized in this section.

Consider a region R of volume V inside the closed surface S. The surface S lies entirely within the cavity walls, except where it crosses the input waveguide in a plane normal to the waveguide. Two different electromagnetic fields are considered within the region R. One field, in the absence of a perturbing object, is designated by the electric and magnetic field components $\boldsymbol{E}_a$ and $\boldsymbol{H}_a$, respectively. The other field, in the presence of a perturbing object within the region R, is designated by the electric and magnetic field components $\boldsymbol{E}_p$ and $\boldsymbol{H}_p$, respectively. These two fields have the same frequency. The vector $\boldsymbol{p}$ is defined by

$$\boldsymbol{p} = \boldsymbol{E}_a \times \boldsymbol{H}_a - \boldsymbol{E}_p \times \boldsymbol{H}_p. \tag{5.1}$$

$\boldsymbol{p}$ over the surface S is related to $\boldsymbol{p}$ throughout volume V by the divergence theorem

$$\int_S (\boldsymbol{n} \cdot \boldsymbol{p}) ds = \int_V (\nabla \boldsymbol{p}) dv \tag{5.2}$$

where $\boldsymbol{n}$ is the unit vector, normally outward from surface S. The assumption that $E_{a,p}$ and $H_{a,p}$ are composed of the same single waveguide mode over the input port surface S_1 leads to the fact that $\boldsymbol{E}_{\mathbf{as}}$ and $\boldsymbol{E}_{\mathbf{ps}}$ lie in the same direction as do $\boldsymbol{H}_{\mathbf{as}}$ and $\boldsymbol{H}_{\mathbf{ps}}$. The subscript s denotes those components of the fields that lie in the plane surface S_1. $\boldsymbol{E}$ and $\boldsymbol{H}$ that lie in a cross-sectional plane must be perpendicular to each other. Then using (5.1) leads to the following equations containing the incident and reflected waves

$$\begin{aligned} E_{\text{as}} &= (1 + S_{11}^0) E_{\text{asi}} && (5.3)\\ H_{\text{as}} &= (1 - S_{11}^0) H_{\text{asi}} && (5.4)\\ E_{\text{ps}} &= (1 + S_{11}) E_{\text{psi}} && (5.5)\\ H_{\text{ps}} &= (1 - S_{11}) H_{\text{psi}} && (5.6) \end{aligned}$$

where S_{11}^0 and S_{11} are the reflection coefficients at S_1, the input port. Using the reflection coefficients and the incident wave power level P_i, the left part of equation (5.2) can be expressed as

$$\int_S (\boldsymbol{np}) ds = 2P_i(S_{11} - S_{11}^0). \tag{5.7}$$

Now consider the right hand side of equation (5.2). By means of a vector identity

$$\nabla \boldsymbol{p} = (\nabla \times \boldsymbol{E}_a) \cdot \boldsymbol{H}_p - (\nabla \times \boldsymbol{H}_p) \cdot \boldsymbol{E}_a - (\nabla \times \boldsymbol{E}_p) \cdot \boldsymbol{H}_a + (\nabla \times \boldsymbol{H}_a) \cdot \boldsymbol{E}_p. \tag{5.8}$$

Using Maxwell's Equations and the Lorentz Reciprocity Theorem (5.7) and (5.8) can be combined to

$$2P_i(S_{11} - S_{11}^0) = \int_{V_p} (\boldsymbol{E}_p \cdot \boldsymbol{i}_{\mathrm{ta}} - \boldsymbol{E}_a \cdot \boldsymbol{i}_{\mathrm{tp}} - j\omega(\mu_a - \mu_p)\boldsymbol{H}_a \cdot \boldsymbol{H}_p)dv \tag{5.9}$$

where $\boldsymbol{i}_s$, $\boldsymbol{i}_d$ and $\boldsymbol{i}_t$ are conduction, displacement and total current density, respectively. V_p is the volume occupied by the perturbing object since outside the object $\nabla \boldsymbol{p} = 0$ applies. This follows from the Lorentz Reciprocity Theorem because at every such point the conductivity, permittivity and permeability are the same with and without the perturbing object. If the perturbing object is small compared to the wavelength, its scattered field consists entirely of the radiation from an electric and magnetic dipole moment. The right side of (5.9) can be replaced by an expression in terms of these dipole moments. The reflection coefficients are otherwise independent of its properties.
Restrictions to the perturbing object are that it has rotational symmetry about an axis, symmetry about a plane normal to the axis, and electric and magnetic polarizabilities that are scalar in the direction of the axis, and in the direction normal to the axis. This leads to the simplified equation [62]

$$2P_i(S_{11} - S_{11}^0) = j\omega k E_a^2 \tag{5.10}$$

for measurement on the axis of a structure and zero magnetic field with a constant k depending on the perturbing object. The S_{11} are obtained by measuring the reflection at the desired frequency and the perturbing object at position z, while S_{11}^0 is measured without a perturbation in the structure. By means of these reflection coefficients, the electric field squared at position z can be obtained along the axis of the structure, except for a constant factor.

5.1.2 Bead pull measurement setup

The bead pull measurements were realized in the modulator hall of the Linac II with a HP 8720C network analyzer (NWA). There the buncher structure could be supplied with the 40 °C cooling water of the linac. In order to tune the structure for $f_{\mathrm{vac}} = 2.998\,\mathrm{MHz}$ in vacuum, the structure has to be tuned to a shifted frequency dependent on the measurement conditions. As a function of air pressure p_{air}, relative humidity H_{air} and the temperatures of the structure T_{str} and the air T_{air}, the correct tuning frequency f_{op} can be calculated as follows:

$$\epsilon = 1 + 10^{-6} \cdot \left(\frac{p_{\mathrm{air}} \cdot \frac{760 \cdot 211}{1013}}{T_{\mathrm{str}} + 273} + \frac{p_0 \cdot H_{\mathrm{air}}}{T_{\mathrm{str}} + 273} \cdot \frac{760}{1013} \cdot \left(\frac{10160}{T_{\mathrm{str}} + 273} - 0.294 \right) \right), \tag{5.11}$$

$$p_0 = 2.8868 \cdot \left(1.098 + \frac{T_{\mathrm{air}}}{100} \right)^{8.02}, \tag{5.12}$$

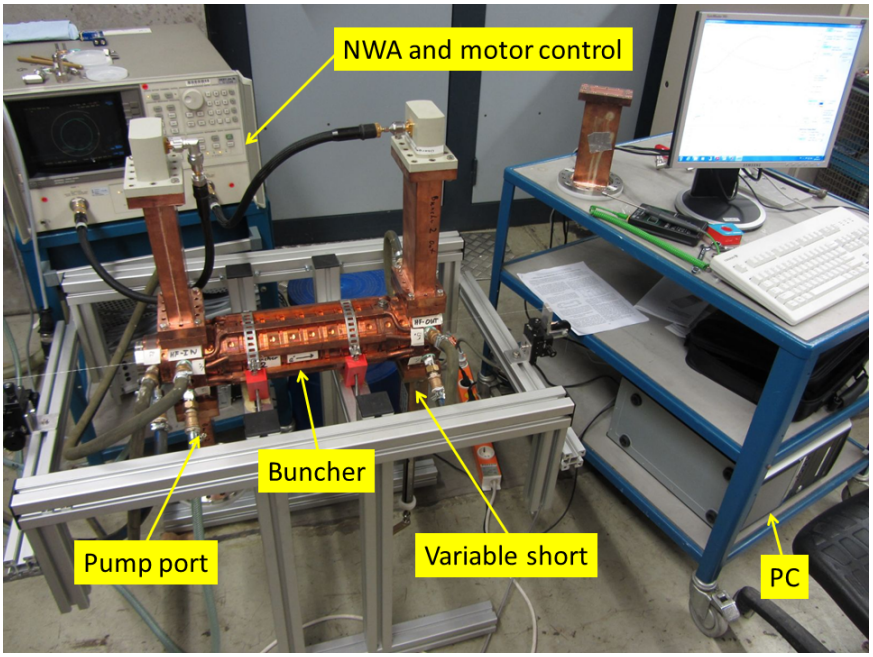

Figure 5.1: Bead pull measurement setup of one buncher structure.

$$f_{\mathrm{op}} = \frac{f_{\mathrm{vac}}}{(1 + 1.7 \cdot 10^{-5}(T_{\mathrm{str}} - 40)) \cdot \epsilon^{\frac{1}{2}}}. \tag{5.13}$$

All temperatures are in °C, the air pressure in mbar and the relative air humidity in %. These equations are similar to those presented in [62], but yield slightly more accurate results. For typical conditions as for example $p_{\mathrm{air}} = 1006\,\mathrm{mbar}$, $T_{\mathrm{str}} = 40.1\,°\mathrm{C}$, $T_{\mathrm{air}} = 23.7\,°\mathrm{C}$ and $H_{\mathrm{air}} = 39.3\%$ the resulting target frequency is $f_{\mathrm{op}} = 2.9971\,\mathrm{GHz}$. An image of the used bead pull measurement setup is shown in figure 5.1. As a bead a 5 mm long piece of a 0.9 mm thick cannula was fixed on a 0.25 mm thick string of plastic material. It was guided by plastic reels that were positioned at the center of the iris holes by micrometer screws. Note that for the measurements of buncher #1 presented in the following aside from results for buncher #2, a different bead and different string, but of similar size and material, were used.

5.1.3 Five stub tuner

For tuning of the second buncher structure, a five stub tuner became available. It consists of five stubs, which are placed alongside a waveguide and are movable in the direction perpendicular to its wall. Such components are used for impedance matching in high power rf applications. Connected to the second coupling cell of the buncher it helped significantly in reducing the reflection at the rear of the structure.

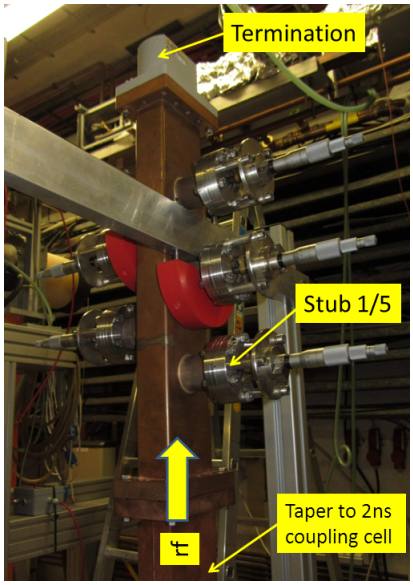

Figure 5.2: Image of the five stub tuner connected to the output coupling cell of the buncher structure during tuning.

In earlier use it had proven suitable for use with high power pulsed rf, so it will be integrated in the waveguide between buncher #2 and linac section #2 directly behind the second coupling cell of the buncher. An image of the stub tuner is shown in figure 5.2.

5.1.4 Tuning procedure for buncher #2

The geometry of the coupling cells differs from the regular cells. Hence the rear part of the structure (coupling cell, tapered waveguide and termination) causes reflections. For the second coupling cell, this hinders the tuning procedure because due to the backward traveling wave a significant standing wave part can be identified in the $\sqrt{|\Delta S_{11}|}$ vs. z plot. A periodicity of three cells becomes visible due to the superposition of two waves traveling forward and backward through the whole structure with approximately the same phase in each n-th and (n+3)-th cell. The left plot in figure 5.3 shows the resulting amplitude $|E|$ vs. z for the untuned structure with the mentioned periodicity.
As a preparation of the tuning procedure the ratio of backward to forward traveling wave has been calculated from the bead pull data and minimized using the stub tuner. For the thirteen traveling wave cells a significantly flatter field amplitude distribution could be achieved. In order to achieve the correct phase advance of $2\pi/3$ per cell, deformation of the cells is necessary. The tuning process was started

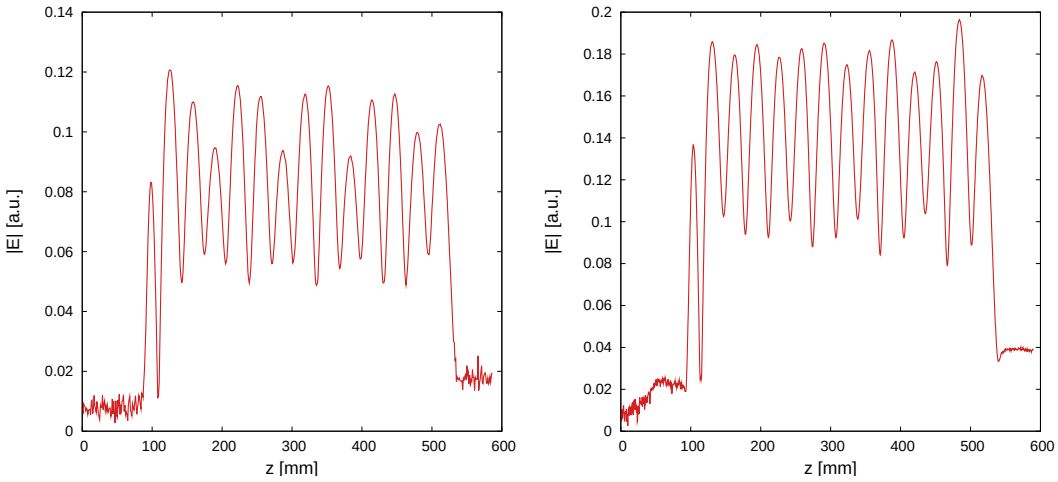

Figure 5.3: Amplitude of the field before (a) and after (b) tuning of buncher #2 at f_{op}.

with the π-mode capture cell, because of the experience with the buncher #1. There a deformation of the capture cell after tuning the traveling wave part undid the achieved field flatness. The objective is to obtain an amplitude in the capture cell, which is as high or higher than in the traveling wave cells. While this was possible for the buncher #1 (see section 5.1.5), the tuning holes at the capture cell of buncher #2 did not allow enough deformation. A 25% lower field had to be accepted, as can be seen in the final field amplitude distribution plotted on the right side in figure 5.3. In the case of future reproduction of such a structure the design will be changed accordingly, by foreseeing additional tuning holes.

When starting the tuning of the traveling wave cells, beginning at the rear of the structure, the correct phase advance of $\varphi = 2\pi/3$ must be achieved while the reflection of the individual cells is supposed to be minimal. Otherwise a standing wave would remain in the structure and hence no flat field can be achieved. In order to reduce the reflection of each cell, the following procedure from [63] was applied. A similar procedure is also presented in [62, 64]. From the data obtained by the bead pull measurement ΔS_{11} can be calculated at the center of each cell. These complex numbers correspond to the wave traveling trough the structure and can be expressed as superposition of a forward and a backward wave between the n-th and (n-1)-th cell, as drafted in figure 5.4.

The forward traveling wave A_n and the backward traveling wave B_n for the n-th cell are

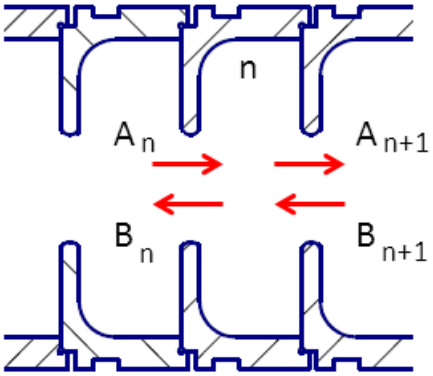

Figure 5.4: Forward and backward traveling wave in n-th cell.

$$A_n = A\mathrm{e}^{j(\omega t - n\varphi)},\ B_n = B\mathrm{e}^{j(\omega t + n\varphi)}. \tag{5.14}$$

The superposition is the wave in the individual cells

$$I_{n-1} = A_n\mathrm{e}^{j\phi} + B_n\mathrm{e}^{-j\varphi},\ I_n = A_n + B_n. \tag{5.15}$$

For the forward and backward traveling wave

$$A_n = \frac{I_{n-1} - I_n\mathrm{e}^{-j\phi}}{2j\sin\varphi},\ B_n = \frac{I_{n-1} - I_n\mathrm{e}^{j\varphi}}{-2j\sin\varphi} \tag{5.16}$$

can be derived. For the n-th cell, the reflected wave is the difference between the backward waves seen before and after the cell. Hence the reflection coefficient for the n-th cell is

$$S_{11}^{\mathrm{local}} = \frac{B_n - B_{n+1}\mathrm{e}^{-j\varphi}}{A_n},\ (2 \le n \le 12). \tag{5.17}$$

In order to calculate S_{11}^{local} for the last traveling wave cell, the following assumption was made:

$$S_{11}^{\mathrm{local}}|_{13} = \frac{B_{13}}{A_{13}}. \tag{5.18}$$

This requires that no reflections are caused by the output waveguide what has been achieved by the optimization of the stub tuner.

5.1.5 Bead pull measurement and tuning result for buncher #2

At the beginning of the tuning procedure the phase advance differs from $2\pi/3$ at the frequency f_{op}. The measured phase along the structure before and after tuning

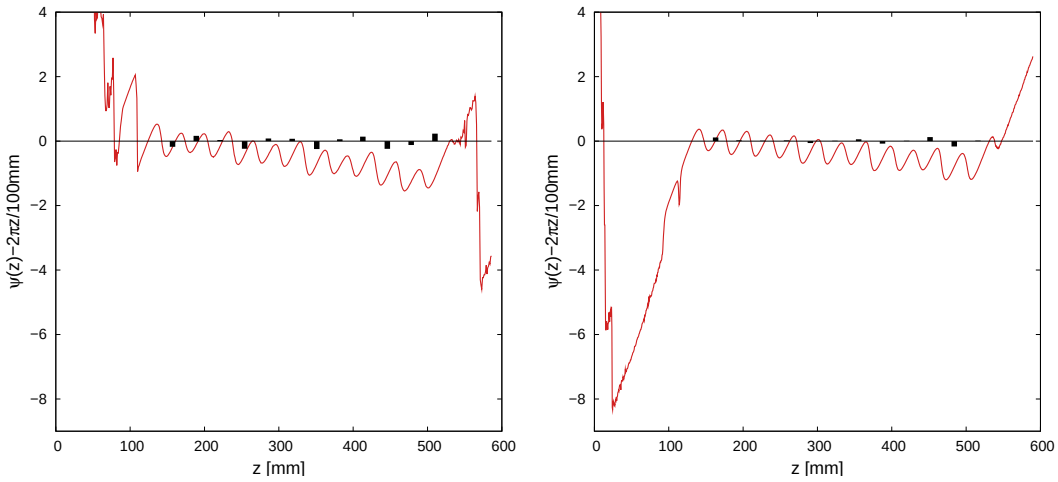

Figure 5.5: Phase of the field before (a) and after (b) tuning of buncher #2 at f_{op}. The black bars show the phase advance -$2\pi/3$ from the prior cell at their centers.

can be seen in figure 5.5. The plot shows the phase with the $2\pi/3$-line subtracted: $\psi'(z) = \psi(z) - 2\pi/3 \cdot 0.03 \cdot z[\mathrm{cm}]$. Thus the plotted $\psi'(z)$ is expected to be periodic within the structure and with equal values for phase at the center of each cell. However there is inaccuracy in realizing the specified motor step size leading to a slope superimposing the plot of the phase. The black bars in the figure indicate the phase difference $-2\pi/3$ to the prior cell. It could be reduced significantly. The calculation is performed for the center of the cells, where the gradient of the phase is lowest. It was located by means of finding the maximum of a polynomial fit to the field data points in the neighborhood of the cell's center. In a polar plot of the full field data before and after the tuning procedure, as shown in figure 5.6, the effect of the tuning procedure is very recognizable. Eventually the field in the centers of the cells form the corners of an equilateral triangle which results from the phase advance of $2\pi/3$ per cell and the constant amplitude.

The resulting S_{11}^{local} values for the thirteen traveling wave cells are shown in figure 5.7. The reflections are reduced by decreasing $\mathrm{Im}\{S_{11}^{\mathrm{local}}\}$ for the individual cells, starting at the rear of the structure. Note that a phase advance of $\varphi = 2\pi/3$ per cell is assumed in this calculation, even though that is achieved accurately only after the tuning procedure. A reduction was achieved for most of the cells, but turned out to be difficult for cells 11 and 12. There spilled brazing material was observed inside the structure with an endoscope, which hinders tuning.

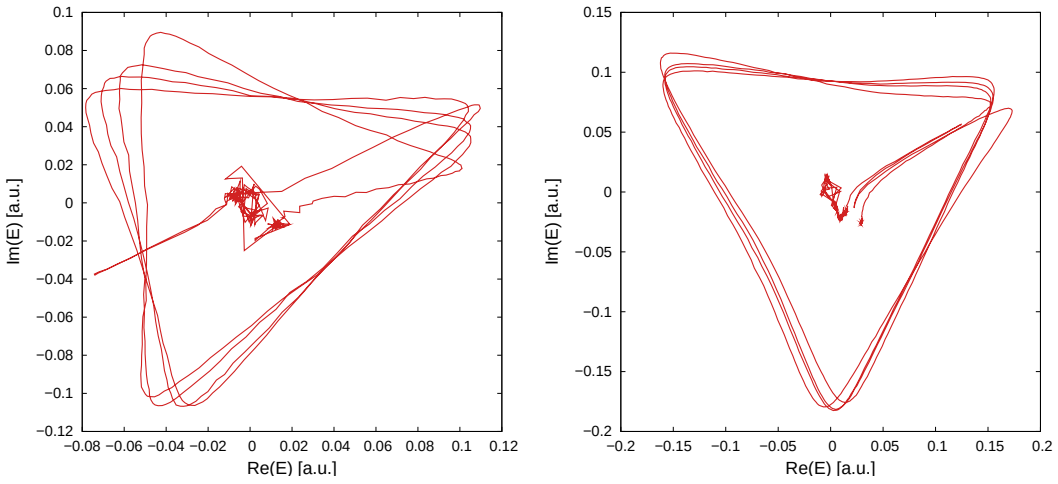

(a) (b)

Figure 5.6: Bead pull measurement polar plot of field before (a) and after (b) tuning of buncher #2 at f_{op}.

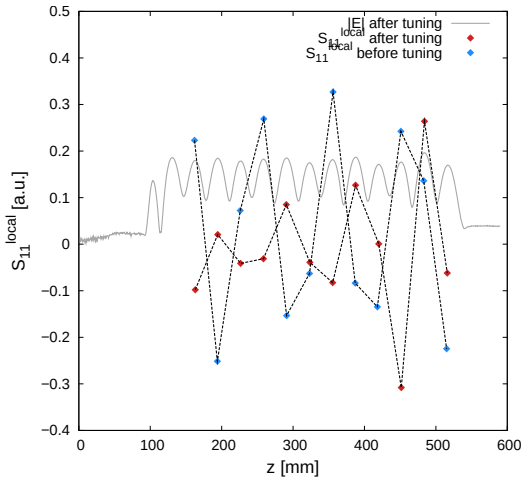

Figure 5.7: $\mathrm{Im}\{S_{11}^{\mathrm{local}}\}$ from cell 2 to 13 before and after the tuning process.

Accuracy of the bead pull measurements

The conditions in the environment of the measurement can influence the result by several ways. Errors in the measurement can be caused by dust particles on the string, which cause unwanted perturbation aside from the bead. Furthermore measurements with high spacial resolution take much time and thus T, p, and H_{air} can change during the measurement. Additionally there are the mentioned deviations between set value and actual value of the bead position. For comparison of the set and actual value of the bead, the observed cell positions can be compared to the values returned by the motor control. The accumulated real motor steps from 1st to last cell are 15 mm bigger than indicated by the scale on the abscissas. This corresponds to a phase shift of 0.3π and is close to the visible deviation from zero at the 13th cell's center of the tuned buncher in the phase plot 5.5. Higher accuracy of the motor step size is not required since it does not affect the tuning procedure.

For the reflection coefficient with the bead outside the structure equal values are expected regardless of the bead being in front of or behind the structure. However in the shown plot of the amplitude the coefficients differ and thus

$$\Delta S_{11}(z = 0) \neq \Delta S_{11}(z > 550\,\mathrm{mm}).$$

This effect is more significant for measurements with smaller motor steps and hence more time consuming cycle. A higher change of environmental conditions can be expected and changes f_{op}. In the tuning procedure that effect was avoided by means of faster measurement cycle through skipping points aside the center of the cells. Feasible bead pull data could be obtained even though inhomogeneities of the string, i.e. perturbing dust particles, might lead to a small contribution to the differing amplitude as well.

Comparison to buncher #1 tuning results

In the traveling wave cells the correct phase advance per cell could be achieved with an accuracy of 3 ° and reflections were minimized. The results of tuning buncher #2 are satisfying except for the low amplitude of the capture cell. The field data from buncher #1 fulfills all requirements and there are no indications for limitations of the beam quality in operation. After the tuning procedure buncher #1 was installed in the test stand. Its final field distribution is shown in figure 5.8. In the test stand rf conditioning was successfully accomplished with a peak power in the SLED pulse of 50 MW.

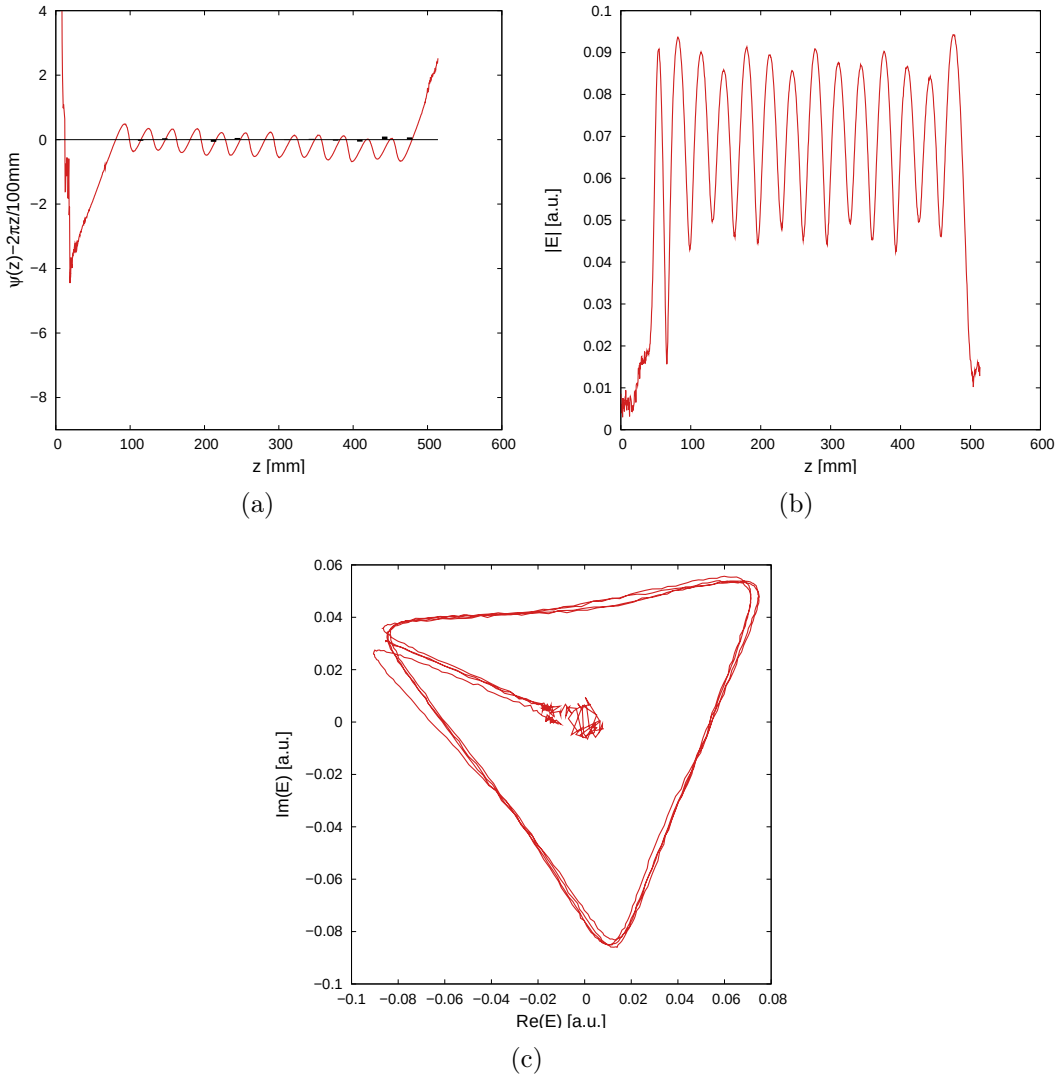

Figure 5.8: Measured phase (a), amplitude (b) and polar plot (c) of the field of tuned buncher #1 at f_{op}.

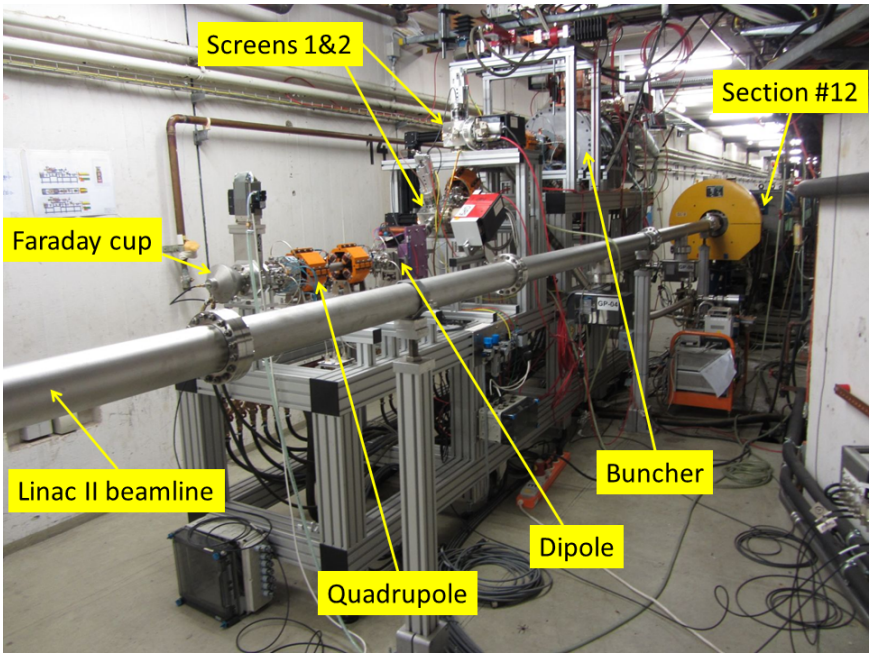

Figure 5.9: Test stand in Linac II tunnel behind section #12. The triode gun and its HV rack are hidden by the case for the buncher structure and the aluminum frame.

5.2 Commissioning of the injection system test stand in the Linac II tunnel

Before construction of the test stand for the new injection system, a decision about its location during tests had to be made. Therefore reasons for different possible locations with different effort and conditions in terms of the necessary infrastructure had to be considered. They are briefly presented in the following. The Linac II modulator hall, the Linac II tunnel and the closed down Linac III were considered as reasonable locations. The modulator hall would have offered the possibility of unrestrained access to the setup and an available rf station, which was formerly used for conditioning of accelerator sections. Limited space and safety issues (HV and radiation) hampered that possibility. The Linac III would have offered enough space, without depending on the operation of other accelerators, but an additional rf station would have had to be installed. Because of the high costs and lack of time for the installation, the Linac II tunnel was eventually chosen as location for the test stand. Even though the available rf station in the modulator hall could be used, the rare access to the tunnel due to permanent demand of Linac II operation for PETRA III and DORIS was a serious restriction. By reason of that compromise unexpected technical failures, that will be specified in section 5.2.2, delayed the opportunity for analysis of the beam properties in the full injection system. The

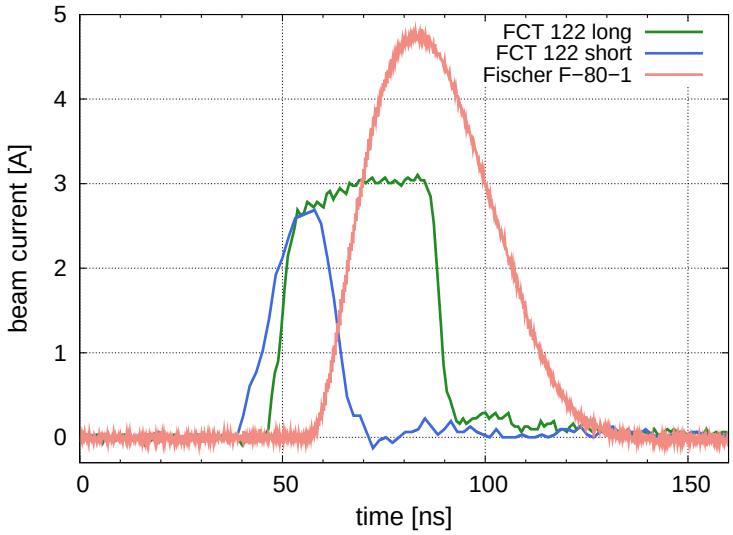

Figure 5.10: Triode gun beam current curve of 38 ns and 17 ns length (FWHM) measured with the inductive current monitor Toroid Bergoz FCT122 20:1 with solenoids YAS0.4/5 switched off and current measured after buncher installation with a Fischer F-80-1.

final status, except for alignment and additional steering magnets, of the test system in Feb. 2013 in the Linac II tunnel is shown in figure 5.9.

5.2.1 Gun calibration

For the triode gun in usual operation the generated beam current is space charge limited. Hence it depends on the accelerating high voltage U_{HV}, the grid voltage U_{bias} for blocking beam generation and the pulse voltage U_{puls1}, which opens the grid temporary for emission. An overview of the used parameters for operation of the triode gun is given in table 5.1. In case of not-space charge limited beam generation, the emission depends as well from the cathode temperature controlled by the heater voltage U_{heat}. Starting in July 2011 the test stand in the Linac II tunnel was operated initially with only the gun, four solenoids for focusing and an inductive current monitor (Bergoz FCT 122) as well as a Faraday cup for beam current measurement. After installation of the gun and its control the associated electronics, i.e. the high

voltage source, cathode heater PS and pulser were commissioned and tested by the external company Puls-Plasmatechnik GmbH (ppt) from Dortmund in Germany. The range of the mentioned parameters for beam current control proved sufficient for reaching the required 6 A current [42] during the calibration procedure.

parameter	range	function
U_{HV}	0-150 kV	acceleration, space charge limit
U_{heat}	5.5-7.0 V	emission
U_{puls1}	0-500 V	grid open
U_{puls2}	0-500 V	grid close
U_{bias}	$U_{\mathrm{bias,min}}(U_{\mathrm{HV}})$-200 V	block emission

Table 5.1: Gun parameter functions and ranges. $U_{\mathrm{bias,min}}$ is the lowest grid voltage where the grid still blocks dc beam current. It depends on U_{HV}.

Figure 5.10 shows an example beam current curve measured directly behind the gun with a Bergoz FCT 122, a fast inductive current monitor. The current reaches only 50% of the possible 6 A, because at that moment the power supplies of two solenoids were inoperable. Before the installation of the buncher structure, the toroid and the cup had to be removed. Additionally a change of the cathode was necessary. Beam current measurement were only possible behind the buncher structure with a Fischer F-80-1 because a wall resistance monitor was not available in time for installation in front of the buncher. At the F-80-1 a peak beam current of 4.7 A was reached with $U_{\mathrm{HV}} = 100\,\mathrm{kV}$ and rf switched off. The diminution is probably due to beam loss at the capture cell's aperture of 10 mm (see figure 3.5), but poorer performance of the newly manufactured cathode is another possible reason. Although tracking with ASTRA shows that full transmission to the toroid's position is possible, slight misalignment of the solenoids can cause losses. Anyway parts of the calibration procedure were repeated for study of the new cathode's behavior.
Figure 5.11 shows the measured peak current for varying U_{puls1} at certain U_{bias}. The plot shows the obtained values for acceleration with $U_{\mathrm{HV}} = 90\,\mathrm{kV}$ on the left side and for $U_{\mathrm{HV}} = 100\,\mathrm{kV}$ on the right. The range of the grid voltage U_{bias} was very limited compared to the former calibration. For $U_{\mathrm{HV}} = 100\,\mathrm{kV}$, it was adjustable only between 90 V and 120 V, where for the old cathode a voltage of $U_{\mathrm{bias}} = 50\,\mathrm{V}$ proved usable. However with the new cathode below 90 V emission was not fully blocked between the pulses and hence DC current occurred from the HVPS. This might be caused by a differing distance of the grid to the cathode surface. The distance is only a few μm and hence high accuracy during manufacturing is necessary. For voltages higher than 120 V, the set value was not transferred to the actual value by the control unit for unclear reasons. Within the remaining parameter range for U_{bias}, the peak current value obtained from the Fischer F-80-1 hardly changes,

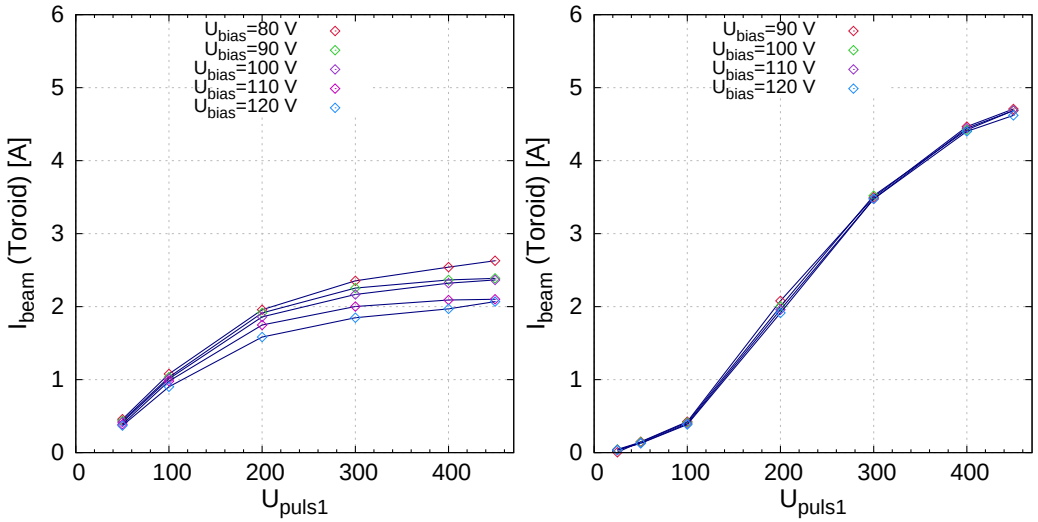

Figure 5.11: Peak beam current control using U_{puls1} at fixed U_{bias} for an U_{HV} of 90 kV (a) and 100 kV (b).

specially at $U_{\mathrm{HV}} = 100\,\mathrm{kV}$. Hence for beam current control the pulse voltage U_{puls1} was used, which allows full range current regulation.
In figure 5.12 the peak beam current vs. U_{puls1} is shown for fixed U_{HV} values. For investigation of the peak beam current for varying gun HV, the beam optics needed to be re-optimized. Otherwise beam loss occurs. For the shown results, the beam current was maximized for each accelerating voltage using all five solenoids and the steerer pair Y2CX0.4/Y2CY0.4. The highest measured beam current during test operation was 5.1 A for $U_{\mathrm{HV}} = 110\,\mathrm{kV}$ and $U_{\mathrm{puls1}} = 450\,\mathrm{V}$. It shows that the beam current for normal $U_{\mathrm{HV}} = 100\,\mathrm{kV}$ operation is not limited by emission at the cathode surface yet. During HV conditioning of the gun with the new cathode voltages up to 125 kV were reached. However a boost of beam current by shifting the space charge limit using the higher HV involves the disadvantage of leaving the initial energy level, the buncher's capture cell was designed for with $\beta = \frac{v}{c} \neq 0.5$. The higher beam current generation for decreased U_{HV} at very low U_{puls1} is unexpected. For longer pulses the beam current drops to a lower level at the rear of the pulse. In order to investigate how the effective pulse length changes for different U_{puls1}, the integrated current has been recorded as well for a series of measurement with $U_{\mathrm{HV}} = 100\,\mathrm{kV}$ and $U_{\mathrm{HV}} = 110\,\mathrm{kV}$. The obtained pulse charge has been divided by the respective peak current. The resulting effective pulse length is shown in the right graph of figure 5.12. For most of the curve and especially for high peak beam current, the effective pulse length does not differ for changing U_{HV}. It is slightly rising

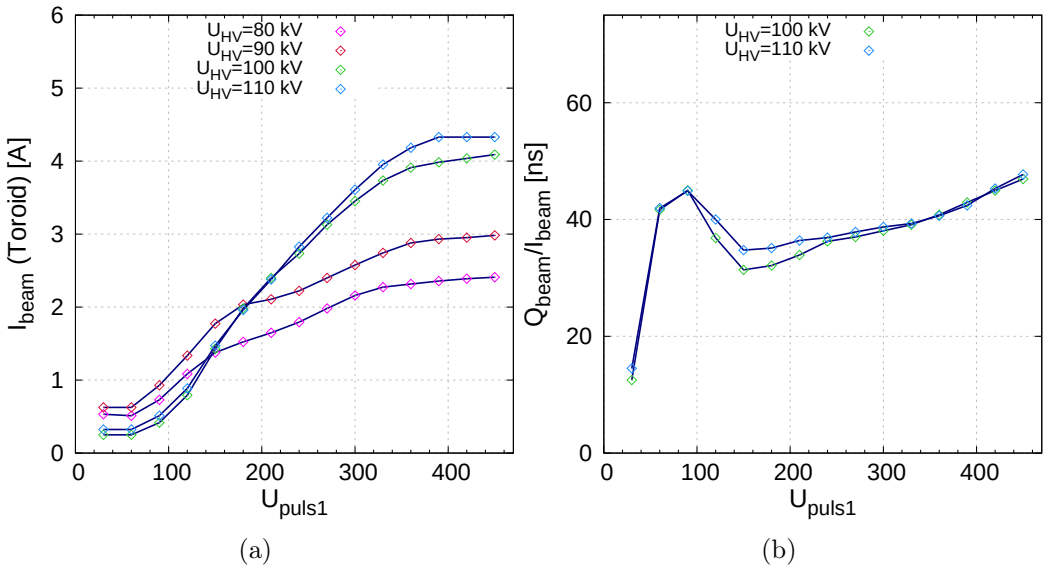

Figure 5.12: Peak beam current control using U_{puls1} at fixed U_{HV} (a) and effective pulse length (b).

with U_{puls1} from U_{puls1} =150 V and has its maximum at the highest pulse voltage of $U_{\mathrm{puls1}} = 450$ V. The gap between start and stop pulse was 82 ns. Seemingly the pulse length is not limited by the parameters used for gun control.
Concluding, all the required values for test operation are reached and the parameters are controllable. Despite the mentioned technical restrictions concerning the gun control, the beam current can be freely set to above 5 A, if necessary. The triode gun matches the current of almost 5 A that is transmitted from the bombarder gun to the first inductive current monitor in the Linac II, which was presented in section 2.4. Control of the pulse length is possible and for the design pulse length of 30 ns constant emission is achieved. Longer pulses can be generated but with dropping beam current.

5.2.2 Technical issues and optimization of reliability

Alignment

During first tests with rf acceleration, more accurate alignment of components, notably the first and second quadrupole magnet turned out to be necessary. Due to a horizontal offset, the two quadrupole magnets behind the buncher structure caused too high deflections of the beam. This could not be compensated by the air-core coil steering magnets. Obviously the beam did not pass through the center of the magnet. It is estimated that afterwards the transversal offset of quadrupole magnets and buncher structure could be minimized to less than 1 mm. Anyhow two

additional horizontal steering magnets with an iron core (Y2CX1.7 and Y2CX2.9) were added in order to avoid any restrictions in terms of beam steering. This proved useful for transmission through the magnetic chicane, where the third quadrupole magnet tends to have a high horizontally defocusing field because of dispersion. Misalignment was discovered as well for the prebuncher with a tilt related to the x-axis of 0.0296 rad. According to ASTRA simulations transmission is hardly diminished. The reason was a nonuniform pressed copper gasket between two vacuum chambers, but a correction was possible only after the period of test operation.

Gun electronics and radiation damage

In addition to the restrictions mentioned in the test stand due to the misaligned components and the missing water cooling for the buncher's solenoid, further technical problems occurred. They had to be solved in order to continue operation of the test stand or to improve reliability in general. The failures concerned amongst others the cathode heater PS, an isolating amplifier, the transition from Ethernet to fiber optics for the control unit, the HV charging resistor and the circuit board connected to the cathode in the gun cone and its cooling fan, but also the control unit outside the tunnel. One crucial point was the radiation from the linac and from the converter in particular, which likely caused parts of the electronics failures in the HV-rack.

The gamma ray dose was first measured for two weeks of operation at the unshielded HV-rack and at its final position in order to find out whether the high dose remains when the gun is commissioned as electron source for the Linac II. The result was a dose of $> 2\,\mathrm{Sv}$. Neutron dose was not measured, for lack of test strips adequate for high doses. In order to avoid exposition of the rack to gamma rays and neutrons from the converter, the niche where the rack was placed was extended by concrete bricks. However the narrow tunnel did not allow a shielding in all directions, thus radiation due to beam loss in the accelerator structures remains undiminished. After its construction the dose was measured again at the rack and in front of the shielding as comparison for three weeks of operation. For all cases a second measurement was carried out for verification. All values are presented in table 5.2. Averaging with the second value measured for verification indicates a reduction of 21% for the gamma ray dose due to the concrete shielding. At the final position, close to the old injection system, radiation can be expected less critical with a dose that is lower by two orders of magnitude. Eventually the shielding proved too big a barrier during maintenance and was uninstalled.

status and position	1st γ-dose/Sv	2nd γ-dose/Sv
without shielding (2 weeks)	2.082	2.675
in front of shielding (3 weeks)	2.699	2.043
behind shielding (3 weeks)	1.993	1.917
final position	0.024	0.023

Table 5.2: Measured γ-dose at the HV-rack during test operation and at the future location.

Cathodes

After completion of the test stand one out of five newly manufactured cathodes was activated and proved reliable during the eight months period of final tests. Before their availability, older cathodes of undefined age were used, of which the first was capable of 6 A emission [42] until the heating element broke. The cathodes are delivered in vacuum and must constantly be stored in such. Lack of such storage is likely the reason why a second older cathode was not capable of emission.

Vacuum window for the screens

The optical window for the imaging with the cameras for the screens is installed sideways of the beam in a flange at a distance of only 68 mm from the center of the screen. The incapability of discharging from electrons scattered in direction of the window caused fissures and in consequence vacuum break down. With replacement of the windows, two measures were taken to avoid repeated damage. An additional vacuum tube of 100 mm was added between screen chamber and window in order to reduce collected charge and a copper mesh-work was fixed on the inner side of the window. By means of that mesh-work, which is pressed to the inner wall of the steel chamber, the window is to be discharged and shielded from scattered electrons. To minimize restrains in visibility by reflection, the mesh was heated until a layer of black copper(II) oxide was formed.

Electron beam reflection on Faraday cup and screens

An issue concerning the accuracy of measurements at the screens is electrons scattered from the surface. They are not taken into account in the charge measurement. Simulations using the EGS5 code yield a fraction of scattered electrons, which depends on the energy of the incident particles. It is 18% for 5 MeV electrons incident on a copper block of 1.5 cm thickness in an angle of 45°. The screens were originally designed for use at FLASH, where a calibration has been carried out [65, 66], showing good agreement for energies of approximately 5 MeV. This obvious disagreement between simulation and calibration is due to several facts that are not taken into account in the EGS5 code. The scattered electrons may originate from ionization and

at their relatively low energies the positive charge of the screen is relevant. Additionally the field of the incident beam has an influence on the scattered electrons. An exact simulation would be non-trivial and it was decided that no correction should be used on the basis of simulations, which do not take the mentioned facts into account. Nonetheless a further calibration must be considered, if charge measurements for energies strongly differing from 5 MeV are carried out.

5.3 Test of BPMs

For BPMs 2, 3 and 4 the function was tested by means of upstream steering and dipole magnets. The beam positions are evaluated from the beam caused signal at 3 GHz by the associated electronics and software tool. The result for changing current at different magnets is shown in figure 5.13. The peak beam current at the toroid was 2.0 A and the beam energy was 4.5 MeV during the BPM tests. Quadrupole magnets between the deflecting magnet and the respective BPM were switched off in order to avoid adulterant deflection. For deflection in the horizontal plane, the steering magnets Y2CX1.7 and Y1CX2.9 were used and for changing the vertical beam position at BPMs 3 and 4, the second dipole magnet Y1D2.8 was used. The central values of each plot are more relevant because accurate information about the beam position is desired close to the design orbit defined by the center of the aperture. This center is not necessarily located exactly at the measured zero position. Most essential for good transmission through the accelerator sections are the beam position at BPM 3 and 4. For the horizontal position, using steerer Y1CX2.9, their indicated position is linear at the center but shows a plateau for the closer BPM 3, which can be caused by a very wide beam.
Anyway for the steerer, which has an integrated field of $1.94 \cdot 10^{-4}$ Tm at 1 A current according to simulations, much higher deflections are expected, exceeding the measured values by a multiple. In the subsequent test with steerer Y2CX1.7 similar results for BPMs 2 and 3 were obtained. For BPM 2 the curve is monotonically increasing, but also flattening. For BPM 3 plateaus at -1.6 A and -0.75 A are visible. Vertical position measurement was investigated at BPM 3 and 4 using dipole Y1D2.8 for steering. Dispersion yields inaccurate positions for both BPMs. Due to the beam loss, the measurement data is of limited use for calibration. The high beam size is part of the analysis in the following chapter. It discusses desirable optimizations, which are going to yield a lower energy spread and a better focused beam from the buncher structure. However, even uncalibrated the BPM data is of use for future operation, indicating drifts of parameters when stable operation is needed. More feasible data for calibration will be obtainable after the optimizations.

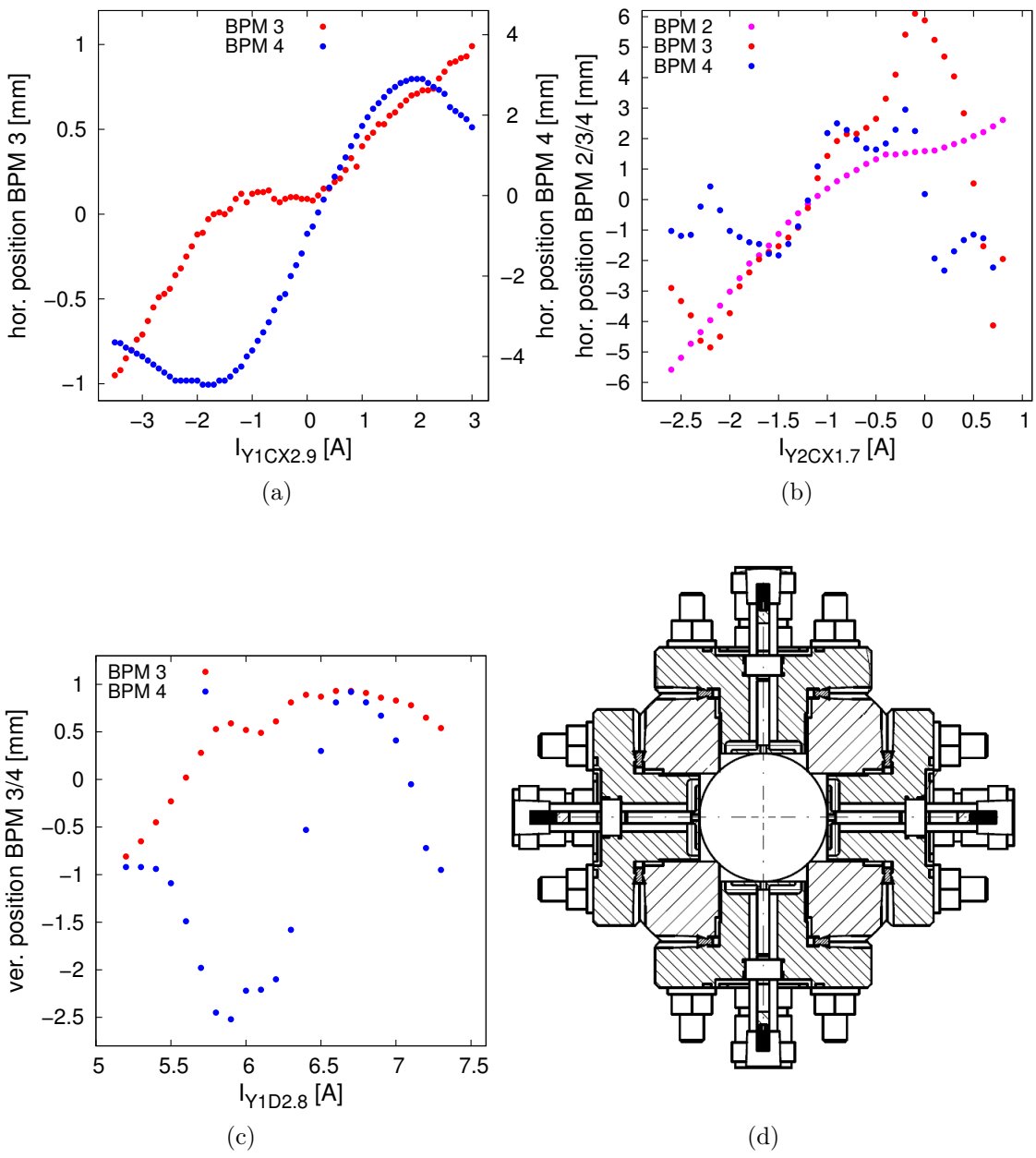

Figure 5.13: Horizontal beam position at BPM 3 and 4 while scanning the current of steerer Y1CX2.9 (a), horizontal beam position at BPM 2, 3 and 4 while scanning the current of steerer Y2CX1.7 (b) and vertical beam position at BPM 3 and 4 while scanning the current of dipole Y1D2.8 (c). A drawing of the BPM is shown in (d).

Chapter 6

Analysis of beam properties at the new injection system

The complete test stand for the new injection system was operated for several months in the Linac II tunnel. The chapter is divided into two topics. The first section discusses adequate rf settings, including different possibilities of compensating the beam induced change of the accelerating voltage in the buncher structure. It is followed by the results of quadrupole scans to analyze beam optics.

6.1 Rf settings optimization

When selecting the diagnostics for the new injection system, a possibility to measure the longitudinal bunch properties directly was renounced, as explained in section 3.4. To be able to draw conclusions as to whether bunching and acceleration by the rf field take place as expected, the dipole magnets can be used as a spectrometer like setup. The deflection angle of the electrons is proportional to the integrated magnetic field of the dipole magnet and inversely proportional to the momentum [67]

$$\theta \propto \frac{1}{p} \int B(s) ds. \tag{6.1}$$

Thus $\theta \propto \frac{1}{p} I_{\mathrm{DP}}$ applies as well, because the magnetic field in the iron of maximal $B = 0.011\,\mathrm{T}$ ist not saturated. In order to estimate the kinetic energy transferred to the electrons from this relation, the dipole magnet field was calculated using CST EM Studio. Afterwards the peak magnetic field was adjusted such that the trajectory of an 5 MeV electron is deflected by an angle of $\theta = 28°$ which corresponds to the design orbit determined by the vacuum chamber. A measurement of the field profile at known magnet current finally yields a magnet current of $I_{\mathrm{DP1}} = 6.43\,\mathrm{A}$ at 5 MeV kinetic energy. Then E_{kin} can easily be calculated from any I_{DP1} using the relation above.

For the measurements of the electron spectrum, the magnet current of the degaussed dipole magnet was increased stepwise, while the Quadrupole Y2Q2.4 was switched off. Pulses with 20 ns length (FWHM) measured at the toroid were used. The spectrum was recorded systematically for varying prebuncher phase and prebuncher amplitude for two different rf input powers P_{rf} in order to find settings for the optimum bunching. The input power was set to 25 MW and 33 MW respectively. Phase and amplitude were adapted using the phase shifter and attenuator, which are installed between the prebuncher and the waveguide connected to the second coupling cell. There parts of the rf power are coupled out in front of the terminating load. First phase ϕ_p and amplitude P_p were chosen such that the transmission to the inductive current monitor was maximal. Phase and amplitude were varied in the proximity of these starting values and for each value the beam was scanned over screen 2 with dipole Y2D1.8. Since no variable aperture was installed, the accuracy of the energy measurement is limited by the screen size of 30 mm. This yields an acceptance of $^{+189}_{-176}$ keV at a kinetic energy of 5 MeV with the assumption that the integrated magnetic field is independent of the trajectory for such small deviations of the deflection angle.

Figure 6.1 shows the spectrum resulting from the peak beam current measured at the screen 2. The kinetic energy is determined by the dipole magnet current. Note that the scale of the abscissa shows theoretical values resulting from the magnet current under the assumption of a pencil beam. In fact the energy distribution is biased by the non-zero vertical beam size almost as much as by the size of the screen, as indicated later by values for the optical beam parameters in section 6.2.1. More accurate measurements of the energy distribution can be obtained, if the beam profile at the screen is saved for each point. Then detailed information of the deflection angle of the main part of the bunch train can be used. Because of the long-lasting problems with the optical vacuum windows mentioned in section 5.2.2, this gain in accuracy was not exploited.

A deconvolution of the measured I_{beam} vs. E_{kin} data using the energy acceptance of the screen was carried out to obtain more accurate data, which is used in the plots. Hence a beam current density ρ vs. kinetic energy is shown instead of the beam current I_{beam} collected by the screen. Therefore the function for list-deconvolution in Mathematica was applied. The function is explained in [68]. Different methods are available and in some cases artifacts like oscillations are possible. The spectrum yielded by the used method seems reasonable and the used code is shown in the appendix. The measured beam current collected by the whole screen results, if the screen size is considered by integrating the momentum range of particles hitting the screen. Based on equation (6.1) the momentum range of particles hitting the screen is $[p - \Delta p_1, p + \Delta p_2]$. From the current density $\rho(p)$, with an electron of momentum

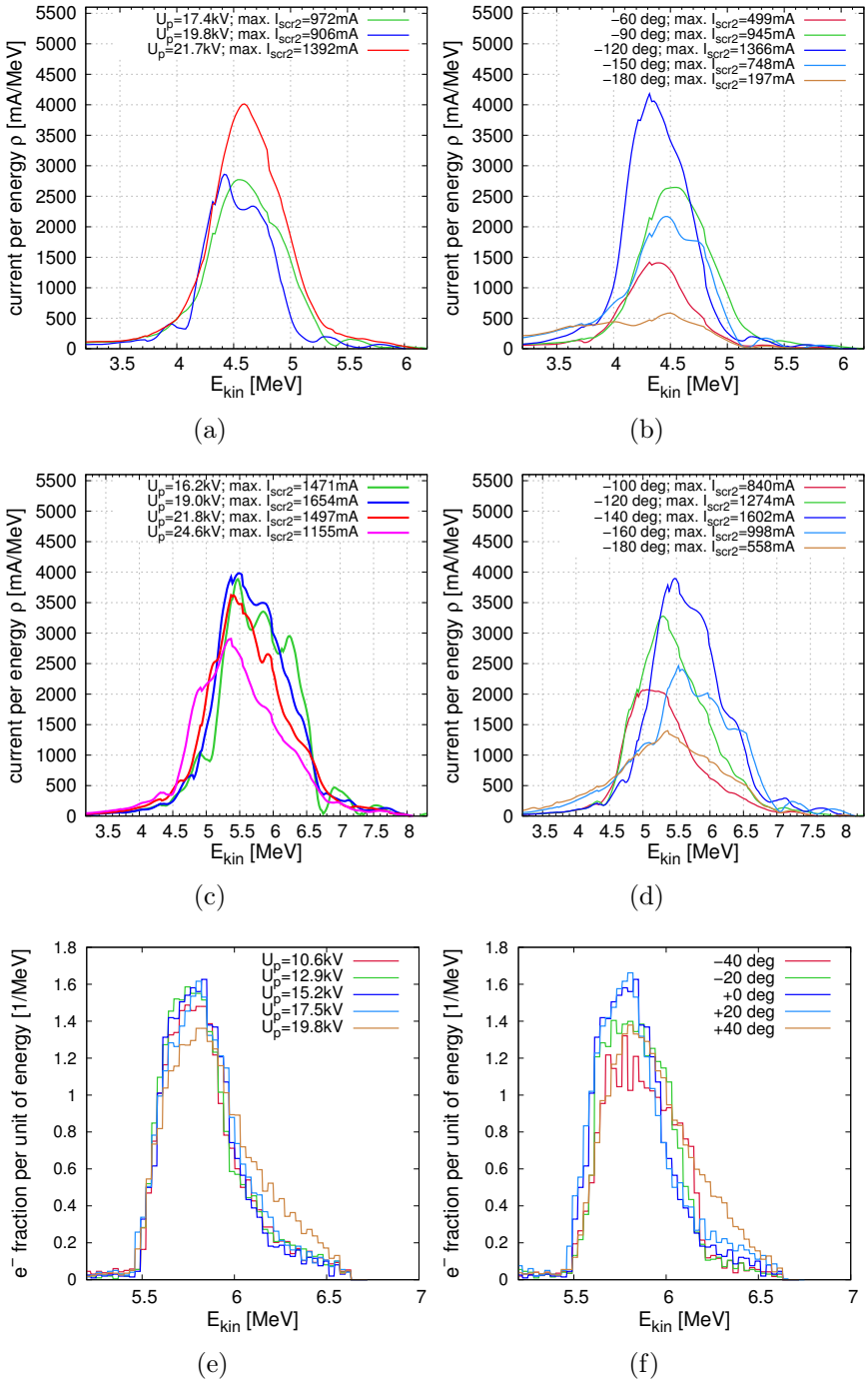

Figure 6.1: Measured spectrum at screen 2 for several values of rf input power and prebuncher amplitude/phase. For $P_{\mathrm{rf}} = 25\,\mathrm{MW}$ differing prebuncher amplitudes were set in (a) and differing phases in (b). For $P_{\mathrm{rf}} = 33\,\mathrm{MW}$ differing prebuncher amplitudes were set in (c) and differing phases in (d). For comparison, simulation data for different amplitudes (e) and phases (f) is shown.

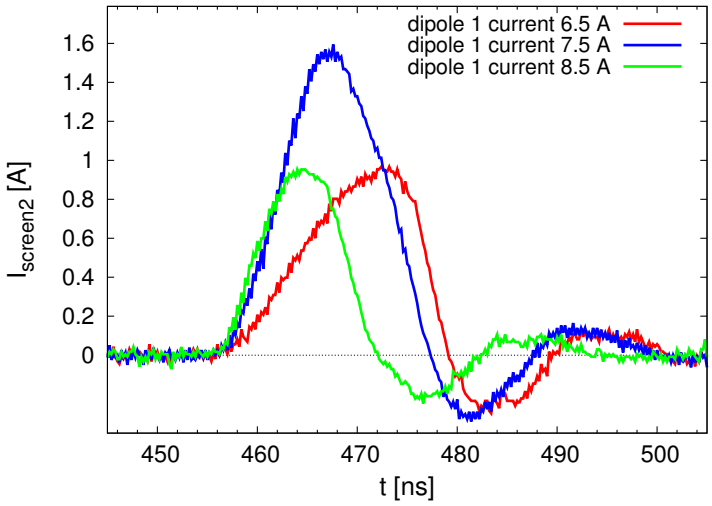

Figure 6.2: Current at screen 2 for different dipole magnet currents. Due to the beam loading induced multi-bunch energy spread, only parts of the beam pulse are transmitted.

p hitting the center of the screen, the beam current collected by the screen results to

$$I_{\mathrm{beam}}(p) = \int_{p-\Delta p_1}^{p+\Delta p_2} \rho(p')dp' = \int_{\frac{p}{1+\frac{\Delta\theta}{\theta}}}^{\frac{p}{1-\frac{\Delta\theta}{\theta}}} \rho(p')dp' \tag{6.2}$$

with $\Delta\theta = 0.93°$ for the used geometry.
The accelerating voltage of the prebuncher, calculated using equation (2.5), varies from 16.2 kV to 24.6 kV. The main intention of this series of measurements was the systematic search for optimum settings with a narrow energy distribution which allows to steer the highest possible pulse charge to the terminating Faraday cup. The result for prebuncher input power of $P_p = 1.709\,\mathrm{kW}$ at $\phi_p = -140°$ and $P_{\mathrm{rf}} = 33\,\mathrm{MW}$ seemed satisfying for further tests and no significantly better result was obtained in further tests using differing P_{rf}. A comparison whether the results fulfill the expectations can be obtained from the spectrum of ASTRA tracked electrons presented in the two bottom plots in figure 6.1. The optimum prebuncher's accelerating voltage in the computation was $U_p = 15.2\,\mathrm{kV}$. However a scan measuring the transmitted charge, corresponding to the number of particles, instead of the peak current would be more meaningful, but the later used real time integration of the pulse was not available during the first tests. Anyway the shift of mean energy and width of the distribution resembles for most of the curves.
Parts of of the widening of the energy distribution is caused by beam loading. It is included in the shown results from ASTRA. The beam induced field in the buncher structure is taken into account using the relation expressed in equation (2.27). A

series of runs has been carried out with decreasing gradient in the buncher structure. The used span of the gradient corresponds to the drop of accelerating voltage from 6.7 MV to 6.2 MV. It is obtained for constant input rf power and a beam beam current of $I_{\mathrm{beam}} = 1.7\,\mathrm{A}$. Constant power was assumed despite the compression of the pulse, because the SLED peak was significantly wider than the fill time of the structure. The measured beam current at the toroid ranged from 1.4 A to 1.8 A for the $P_{\mathrm{rf}} = 33\,\mathrm{MW}$ tests. Due to the significant beam loss before and in the bunching process, the current, which corresponds to a lossless acceleration on the crest of the field, as assumed in theory, is not known exactly. Even though that current surely depends on amplitude and phase, the same current was assumed in all ASTRA runs for simplicity reasons.
Since due to beam loading peak beam current vs. energy does not develop analogue to pulse charge, it must be pointed out again that the shown distributions are of limited comparability. Anyway these measurements are of use to find the optimum field parameters at the prebuncher and indicate a strong influence of beam loading, dominating the influence of the size of the beam and the screen. The simulations give additional information of how the actual spectrum changes with the field parameters. Comparability between the shown simulation data and the pulse charge vs. energy measurements, carried out when real time integration was realized, is given. Using that possibility a detailed analysis of how beam loading widens the spectrum in parts of the beam pulse and how this effect can be reduced was done and is presented in the following sections.

6.1.1 Influence of beam loading

A big challenge in terms of achieving high transmission is posed by beam loading in the buncher structure at long pulse length, high peak current and hence high total pulse charge. Such high charges will be necessary when positron operation should be demanded again and thus high beam power at the converter is needed. The broadened energy distribution resulting from beam loading was again investigated using the first dipole magnet with the screen behind as a spectrometer like setup. The effect induces a clear cutting in the beam pulse caused by dispersion and consequently loss on the aperture between the first dipole magnet and screen 2.
In figure 6.2 the pulse forms measured at the screen are shown for different dipole magnet currents at 2.2 A peak current at the toroid. For the highest dipole current of 8.5 A only the front part of the beam pulse is transmitted. This is were the energy is highest, before the accelerating voltage drops, causing a multi-bunch energy spread. For the lowest magnet current, the rear part of the pulse is measured at the screen, and equivalently for the center of the pulse. This shows, even if high peak beam current through the magnetic chicane and in the future through the linac to the converter is reached, the pulse length will become short and hence the number of

positrons produced per pulse might be not sufficient. Obviously, the high energy spread is not mainly a single-bunch problem and beam loading must be investigated.

The presented beam current measurements show significant oscillation at the rear of the pulse because of reflections in the wire. Hence beam current results might be inaccurate at individual points. However this inaccuracy does not affect the measurement of the total pulse charge because therefore an integration over the pulse, including all oscillations, is carried out. This yields an exact result for the charge, which is mainly of interest in the further analysis.

In order to achieve compensation of beam loading, the timing of the beam pulse can be adapted such that the buncher is passed by the beam while the input rf power is rising due to the steep edge of the SLED pulse. Then the beam induced field can be compensated by the rising accelerating voltage during filling of the structure. The second possibility of using a feed forward at lower rf power has been investigated experimentally as well.

Regarding beam loading, it is also of importance that the mean energy of a long bunch train with constant bunch charge stabilizes for the rear part of the bunch train, when incoming rf power and beam induced field compensate each other. As indicated above, for a beam pulse with higher length than the fill time of the structure the energy drop should disappear for the last bunches. Even though the achievable length of constant beam current is lower than the fill time of the buncher, the possibility to analyze the rear part of a bunch train was used as an approach to check whether the energy distribution for a single bunch would become significantly smaller than in the measurements of the full pulse. The left plot in figure 6.3 shows how the drop of accelerating voltage ΔV_{acc} decreases theoretically for the second half of a 30 ns pulse. The red curve shows its drop for a 15 ns pulse and the blue curve the bigger drop for a 30 ns pulse of each 2.5 A beam current. The saturation with no further drop of V_{acc} for pulses longer than the fill time is represented by the black curve.

For an experimental analysis of the rear part of the pulse, the beam current curve was saved at the Faraday cup of screen 2 for a longer pulse of 30 ns length and for a shorter pulse of 15 ns length, while the dipole Y2D1.8 magnet current was increased stepwise. Afterwards for each step the short pulse was subtracted from the long pulse yielding the pulse form of the rear part of the bunch train. An example difference of a long and a short pulse can be seen in the right plot of the figure. These pulses were integrated in order to obtain the transmitted charge. Note that the results for the difference of two measured pulses are called result for saturation of beam loading in the following, even though the pulses are too short to achieve full saturation. The plot at the bottom of figure 6.3 shows the resulting charge vs. kinetic energy calculated from the magnet current for both the short pulses and the subtraction of short pulses from the long pulses. The peak current of such pulses

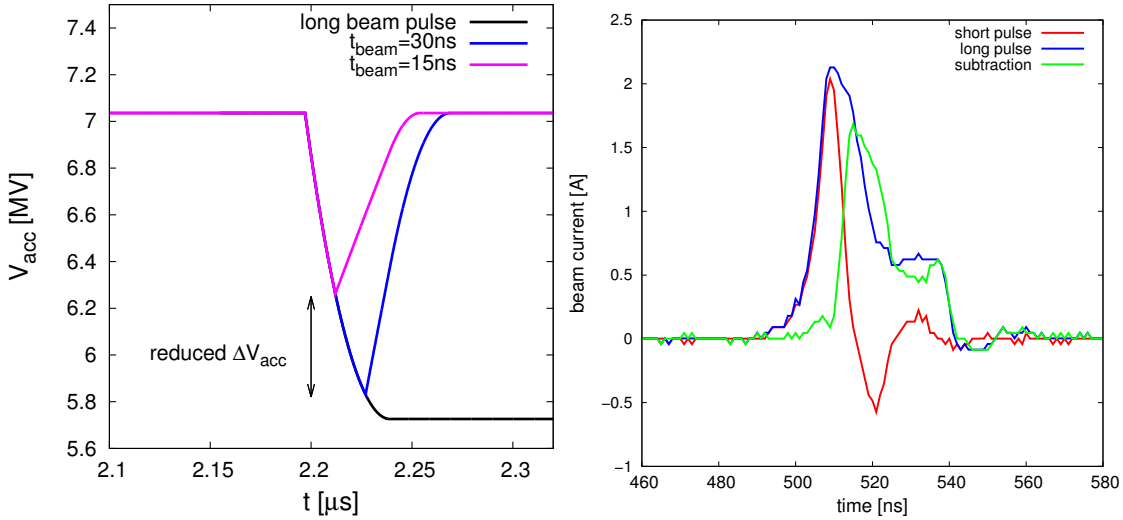

(a) (b)

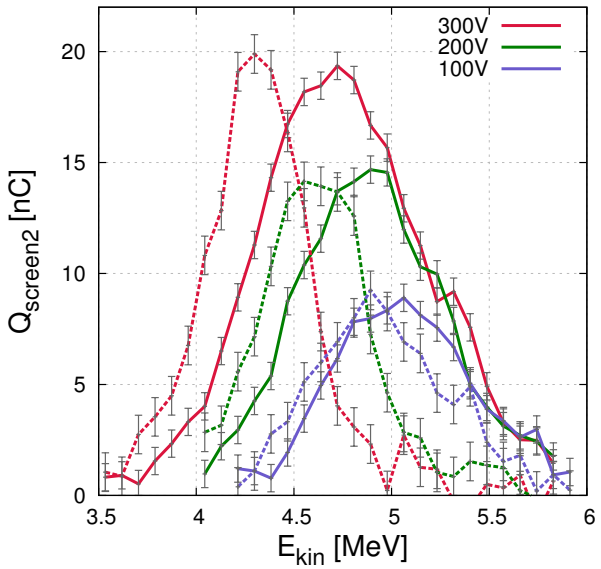

(c)

Figure 6.3: Theoretical beam induced saturation of V_{acc} (a) and example subtraction of short and long pulse form (b). Plot (c) shows the measured Q_{screen2} vs. E_{kin} for unsaturated (solid lines) and saturated (dashed lines) accelerating voltage.

has not been investigated, because it is distorted by the oscillations seen in signals from the Faraday cup. The beam optics and prebuncher field were optimized with a gun pulse voltage $U_{\mathrm{puls1}} = 300\,\mathrm{V}$. Anyway the measurement was repeated with lower U_{puls1} and hence lower beam current for comparison without change of other settings. In this Q vs. E_{kin} plot the charge calculation is done using the measurements of single pulses while for all others average values of a greater number of pulses are shown. This results in much higher statistical errors as indicated by the error bars. The error is dominated by the resolution limit of the used ADC.
The $U_{\mathrm{puls1}} = 300\,\mathrm{V}$ curve fulfills the expectations of a significant reduction of the width of the spectrum from 0.9 MeV to 0.6 MeV (FWHM) while the mean energy dropped from 4.75 MeV to 4.30 MeV. For the attempts with lower beam current the mean energies become higher because of lower induced field. Yet the energy width of the rear part of the beam pulse does not become as narrow as for the highest current. For the $U_{\mathrm{puls1}} = 100\,\mathrm{V}$ curve the difference becomes very small. This might be caused by longitudinal overfocusing which in return comes from lower space charge forces compared to the high current curve. Thus the beam crosses the structure badly bunched and smaller parts of the bunch are accelerated on the crest of the field. The presented experimental results verify that the energy drop at the rear of the pulse is caused by beam loading. As shown, the spectrum becomes narrower, if influence of beam loading is reduced.

6.1.2 Beam loading compensation

As mentioned above the SLED pulse offers the opportunity to be used for compensation of beam loading. Its shape can be modified easily by use of potentiometers in the electronics which realizes the 180° phase jump. For that purpose they have been set such that dP_{rf}/dt is maximized. Figure 6.4 shows the obtained SLED pulse with and without the impact of the beam induced field. For measurement of the rf power curve, the signal was coupled out at the buncher structure and recorded with an oscilloscope, while the calibration was carried out with a peak power meter. The attempt of beam loading compensation was realized even though, as explained in section 3.2.2, the operation of buncher and accelerator section with one rf station would mean a not properly filled section, if such a compensation scheme needs to be used.
It turned out that neither the peak beam current nor the transmitted charge were improvable in this manner. The deviation of the prebuncher amplitude from the nominal value or not stabilized phase might cause the loss by improper bunching. The ratio of the prebuncher amplitudes calculated from the measured $P_{\mathrm{rf}}(t)$ at the time t_{beam} when the first bunch enters the prebuncher and $t_{\mathrm{beam}} + 50\,\mathrm{ns}$ is

$$\frac{U_p(P_{\mathrm{rf}}(t_{\mathrm{beam}} + T_{\mathrm{a,buncher}} + 50\ \mathrm{ns}))}{U_p(P_{\mathrm{rf}}(t_{\mathrm{beam}} + T_{\mathrm{a,buncher}}))} = 1.105.$$

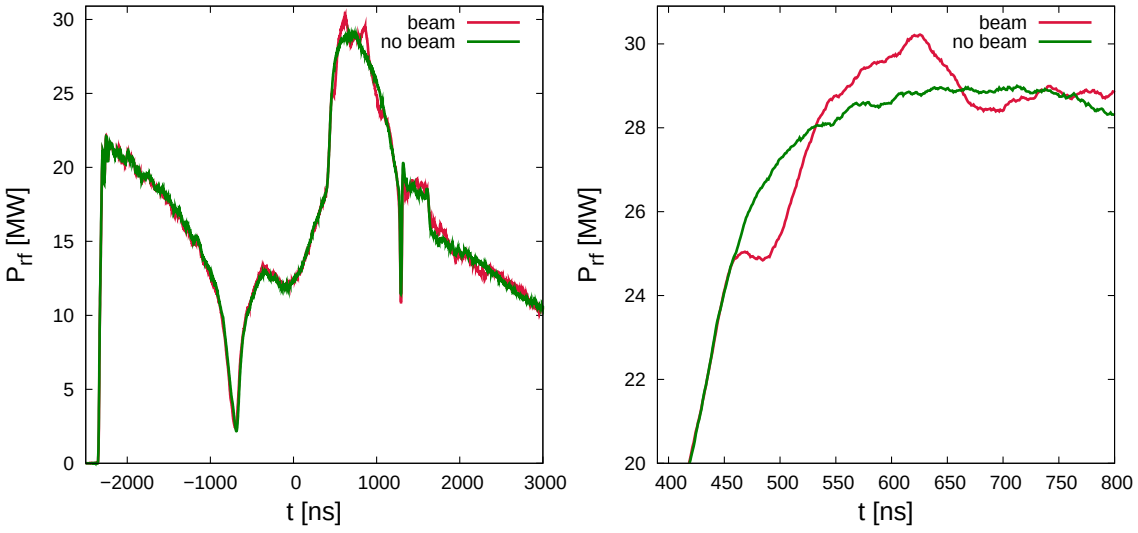

Figure 6.4: Measured effect of beam loading on SLED pulse for compensation purpose: Overview of the whole SLED pulses with 29 MW input power (a) and detailed view of the power drop caused by the beam pulse (b).

According to the data shown in figures 6.1 the 10.5% rise of U_p should not affect transmission to the observed extent. However in relation to the 180° phase jump a small drift of the phase can impede bunching. When after installation in the linac the prebuncher rf will be coupled out in front of the first coupling cell, better results can be expected for this scheme.
Since attempts to achieve transmission of higher charge by using the rising edge of the SLED pulse for beam loading compensation failed in terms of charge transmission, further tests focus on compensation with detuned SLED cavity. Therefore no phase jump is induced and the rectangular, unamplified rf pulse of 4 μs length as emitted from the klystron is coupled into the structure for acceleration. The obtained rf power during that test of 17 MW was very low compared to the usual performance for such an rf station with up to 25 MW. For compensation purpose a linear amplifier and a pulse generator were added temporarily to the rf station control in order to obtain a pulse as shown in figure 6.5. As before for the SLED pulse, the rf power is shown with and without influence of the beam.
A big drop in rf power remained because a bigger step in rf power requires further reduction of the lower rf power level which in turn limits the prebuncher amplitude. For that reason bigger steps did not yield better results. Figure 6.6 shows a peak beam current I and pulse charge $Q_{screen2}$ vs. kinetic energy E_{kin} comparison of the beam accelerated using that scheme and a beam accelerated by use of constant

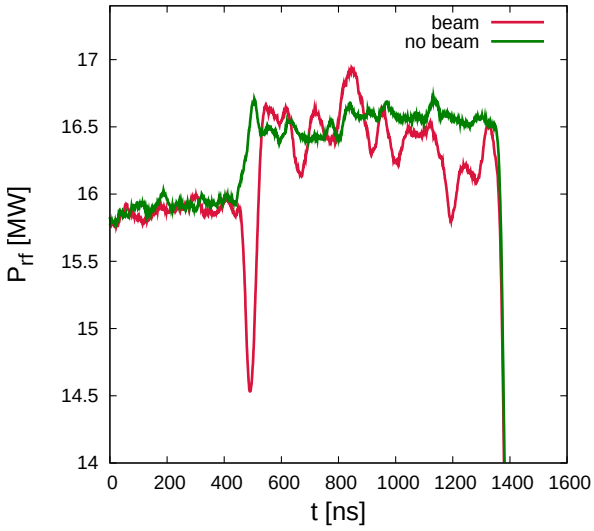

Figure 6.5: Measured effect of beam loading on the rf pulse when the feed forward for compensation is used.

rf power. Statistical errors in the measurement are smaller than the size of the symbols because of averaging over a high number of beam pulses. The test was carried out for different emitted currents controlled by U_{puls1}. Even though the peak current at the screen 2 is lower when beam loading compensation is tried, the improvement is clearly visible in the right plot. As intended the cutting of longer beam pulses recedes and hence the achievable transmission in terms of charge is up to 25% higher for U_{puls1}=400 V. For lower currents the curves become congruent. However the transmission achieved in this test is hardly sufficient to compete with the present Linac II injection. That yields approximately 2 A·20 ns=40 nC at the converter.

Normally with detuned SLED cavity rf power of 25 MW is achievable. That would offer more options in terms of size of the rf power step with reasonable acceleration. Thus for future operation of the buncher structure this scheme of beam loading compensation is promising, particularly with respect to filling of a following accelerator section and constant prebuncher field.

6.1.3 Maximized charge transmission

For different rf pulse properties the transmission was optimized with and without the attempt of beam loading compensation. Aside from reduction of activation, it is essential for future operation of the Linac II with positrons to have sufficient particles generated per beam pulse. Therefore the objective of the optimizations

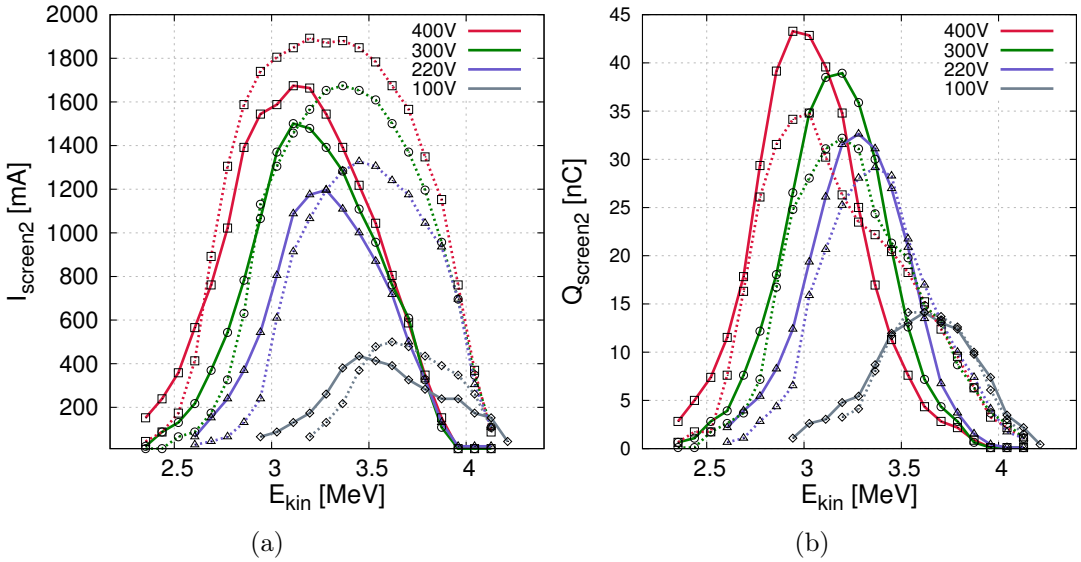

Figure 6.6: Beam current (a) and pulse charge (b) vs. E_{kin} with (solid lines) and without (dashed lines) attempt of beam loading compensation by means of a feed forward (detuned SLED cavity and P_{rf} ≈17 MW). The tests were carried out for different beam currents controlled by the parameter U_{puls1} at the gun between 100 V and 400 V.

was to get as much charge per pulse as possible, within a for PIA acceptable pulse length, to the terminating Faraday cup. The results are summarized in table 6.1.

timing	rf power/MW	Q_{toroid}/nC	Q_{screen1}/nC	Q_{screen2}/nC	Q_{cup}/nC
no comp.	29 (SLED)	154	108	60	56
no comp.	45 (SLED)	150	122	74	58
comp.	29 (SLED)	119	-	46	-
comp.	17 (flat rf)	91	-	60	48.0

Table 6.1: Measured transmissions through the injection system test stand with/without attempt of beam loading compensation for tuned/detuned SLED cavity.

For a 20 ns pulse as lately used for positron generation the maximally transmitted charge of 58 nC corresponds to a mean beam current of 2.9 A. Assuming no further losses in the accelerator sections once the new injection system is commissioned, the expected number of particles would be 45% higher. A reduction of the positron rate will be caused by the reduced energy due to removal of section #1. Using the data obtained by EGS5 simulations (see figure 4.10) for an electron energy at the converter of 320 MeV instead of 400 MeV, the positron yield would be improved by 20%. Concluding, the presented values for transmitted charge show, that the new injection system can reach the required performance, if good transmission through

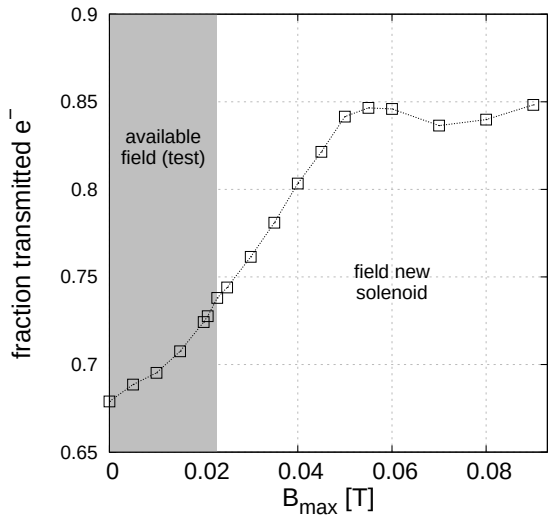

Figure 6.7: Change of transmission to screen 1 position by use of solenoid Y2SOL0.8 in ASTRA with file optimized for $B_{\max} = 0.023\,\mathrm{T}$.

the accelerator sections is reached. Higher transmission through the injection system is desirable. The remaining problems must be analyzed and possible modifications to reach better transmission are discussed as follows.
A possible reason for the bad transmission is the wide spectrum. But since even dispersion free transmission to the screen 1 is unsatisfying, an analysis of optical beam parameters is reasonable. The following section discusses quadrupole scans realized for that issue. ASTRA tracking shows higher loss with the maximum field of $B_{\max} = 0.023\,\mathrm{T}$ for the air cooled solenoid at the buncher as well. Still the obtainable transmission with such a restriction is far higher in the computation, as shown in figure 6.7. For the scan all fixed parameters were set as in the test stand, including the prebuncher tilt around the x-axis of 0.0296 rad and tilts of the first two quadrupoles around the z-axis of 0.0112 rad and 0.0225 rad respectively. Afterwards a full optimization of all variable parameters was done, followed by the scan of the field for solenoid Y2SOL0.8 at the buncher. The simulation promises a gain in transmission of 11% to 84% at screen 1 position. Here the transmission is based on the particles emitted at the cathode. The beam loss does hardly occur behind the buncher structure.

6.2 Beam profile measurement

For the emissions at the cathode, the beam profile is expected Gaussian. Deviations on the screens occur due to the high energy spread behind the buncher, particularly

at screen 2 due to dispersion. As a consequence the beam profile changes when switching to a different pulse length. Figure 6.8 shows example beam profiles at screen 2 for a 30 ns and a 15 ns beam pulse (FWHM at the toroid). The profiles are different but both are not Gaussian and look more like a superposition of two independent Gaussian profiles. If the short pulse image is subtracted from the long pulse image (analog to the procedure explained above for beam current curves at different pulse length), the resulting image represents the profile of the lower energy beam part, where less deviation from the Gaussian profile is expected. In fact a beam spot remains, which is shifted with respect to the 15 ns spot. The shift in the y-axis is due to dispersion while the higher focusing strength for the lower energy causes the different horizontal and vertical beam size. These subtractions have been used as one setting amongst others for measurement of beam parameters with screen 1.

6.2.1 Quadrupole scan

For study of the optical beam parameters, quadrupole scans have been performed with the second quadrupole magnet Y2Q1.5 on screen 1 after a drift of $L = 0.81\,\mathrm{m}$, as illustrated in figure 6.9. The scans were done in both horizontal and vertical with that quadrupole focusing in the respective plane. The technique uses the transformation matrices for focusing quadrupole magnets and drift space and exploits conservation of emittance, which means that according to Liouville's theorem it is not changed by focusing magnets or in drift space.

Calculation of optical beam parameters using transformation matrices The emittance can be calculated from the rms beam size and the beta function with the relations

$$\epsilon_x = \frac{\sigma_x^2}{\beta_x(s)}, \tag{6.3}$$

$$\epsilon_y = \frac{1}{\beta_y(s)} \left[\sigma_y^2 - \left(D(s) \frac{\Delta p}{p} \right)^2 \right], \tag{6.4}$$

assuming that the distribution in y and Δp is Gaussian. The dispersion D(s) comes into play primarily after deflection by the dipole magnets in the vertical plane and is neglected because the screen terminating the straight beam line behind the buncher was used. The beam matrix $\boldsymbol{\sigma}$ is

$$\boldsymbol{\sigma} = \epsilon \begin{pmatrix} \beta & -\alpha \\ -\alpha & \gamma \end{pmatrix} \tag{6.5}$$

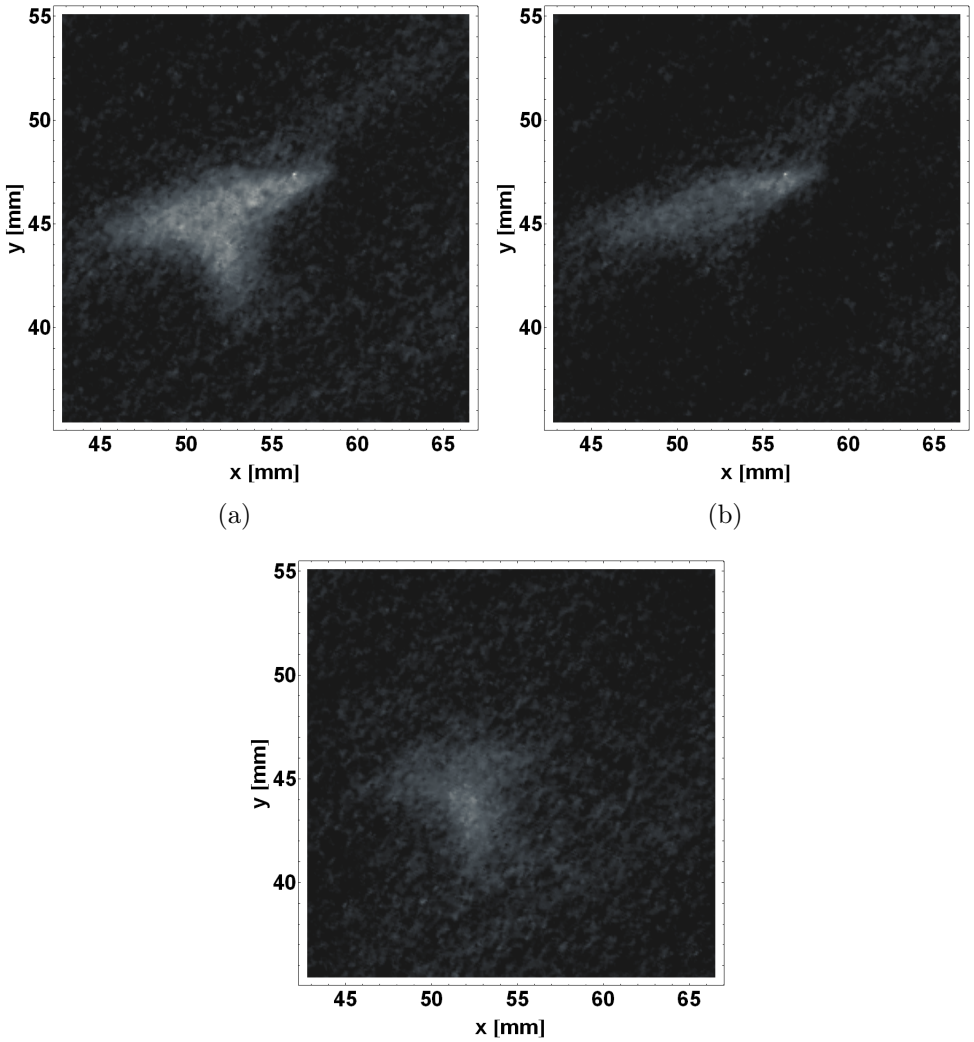

Figure 6.8: Beam spots on screen 2 for 30 ns pulse (a), 15 ns pulse (b) and subtraction of both images (c) are shown. Dispersion occurs in the y-axis.

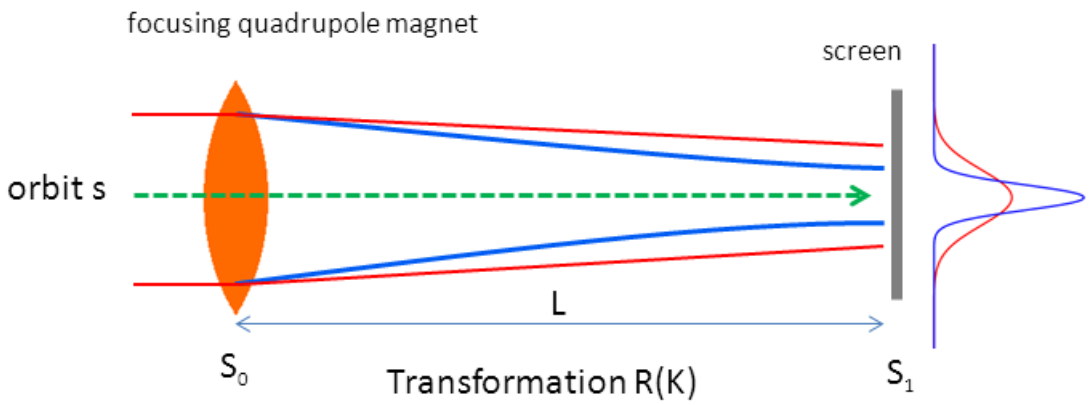

Figure 6.9: Draft of the setup for quadrupole scans. Beam profiles for different K are evaluated.

with

$$\sqrt{\det \boldsymbol{\sigma}} = \epsilon. \tag{6.6}$$

The beam width squared $\sigma_x^2 = \sigma_{11}(s_1, k)$ are measured to determine emittance and twiss parameters for the horizontal and equivalently for the vertical plane. While the distance $L = s_1 - s_0$ of the used quadrupole and screen is fixed, measurements for varying quadrupole strength k are performed. The transfer matrices for the focusing quadrupole magnet and the drift space are

$$\boldsymbol{R}_{\text{drift}} = \begin{pmatrix} 1 & L \\ 0 & 1 \end{pmatrix}, \tag{6.7}$$

$$\boldsymbol{R}_{\text{focus}} = \begin{pmatrix} \cos\sqrt{k}l_Q & \frac{1}{\sqrt{k}}\sin\sqrt{k}l_Q \\ -\sqrt{k}\sin\sqrt{k}l_Q & \cos\sqrt{k}l_Q \end{pmatrix}. \tag{6.8}$$

For focal length much larger than length of the quadrupole magnet $f = \frac{1}{kL} \gg l_Q$ the thin lens approximation can be applied and $\boldsymbol{R}_{\text{focus}}$ simplifies to

$$\boldsymbol{R}_{\text{focus}} = \begin{pmatrix} 1 & 0 \\ -\frac{1}{f} & 1 \end{pmatrix} = \begin{pmatrix} 1 & 0 \\ K & 1 \end{pmatrix}. \tag{6.9}$$

Using $\boldsymbol{R}(K) = \boldsymbol{R}_{\text{drift}} \cdot \boldsymbol{R}_{\text{focus}} = \begin{pmatrix} 1+LK & L \\ K & 1 \end{pmatrix}$ and the relation

$$\sigma(s_1, K) = \boldsymbol{R}(K)\sigma(s_0)\boldsymbol{R}^T(K), \tag{6.10}$$

the beam matrix element $\sigma_{11}(s_1, K)$ at the screen position as a function of $\sigma(s_0)$ can be expressed [69]:

$$\sigma_{11}(s_1, K) = L^2\sigma_{11}(s_0)K^2 + 2(L\sigma_{11}(s_0) + L^2\sigma_{12}(s_0))K \tag{6.11}$$
$$+ L^2\sigma_{22}(s_0) + \sigma_{11}(s_0) \tag{6.12}$$
$$= aK^2 - 2abK + ab^2 + c. \tag{6.13}$$

A parabola fitted to the measured $\sigma^2_{\mathrm{x,y}}$ as a function of K delivers the parameters a, b and c. The beam matrix at the quadrupole position s_0 can be expressed as

$$\sigma_{11}(s_0) = \frac{a}{L^2}, \tag{6.14}$$
$$\sigma_{12}(s_0) = -\frac{a}{L^2}(\frac{1}{L} + b), \tag{6.15}$$
$$\sigma_{22}(s_0) = \frac{1}{L^2}(ab^2 + c + \frac{2ab}{L} + \frac{a}{L^2}) \tag{6.16}$$

and then the emittance can be calculated using equation (6.6) to

$$\epsilon = \sqrt{ac}/L^2 \tag{6.17}$$

6.2.2 Evaluation of beam optics

For determination of the plotted rms beam sizes, a least-squares fit of a Gaussian profile was applied to the individual images taken from the screen, which have a resolution of 640×480 image points. For elimination of the non-zero background and noise, a background image has been subtracted and a median filter with one pixel radius was used. The plotted error bars result from the standard errors of the fit algorithm and the limited resolution of the imaging. Additional systematic errors in the beam profile persist from beam loss on apertures and degrading sensitivity of the YAG coated screen. The parabolas fitted to the measured $\sigma^2_{\mathrm{x,y}}$ vs. K_{q2} data are shown in figures 6.10 and 6.11 for the horizontal and the vertical plane and different settings of the machine. For both planes, the same quadrupole Y2Q1.5 has been used for focusing in the respective plane, wherefore the polarity of both quadrupole magnets behind the buncher has been reversed.
For the two scans shown in figure 6.10, the beam was accelerated using a SLED pulse and with detuned SLED cavity respectively. The parameters calculated from the fitted parabola are presented in table 6.2. Kinetic energy values are calculated from the dipole current, where the maximum charge of the 15 ns pulses reaches screen 2. Because of the widely rotational symmetry of the setup, parameters for

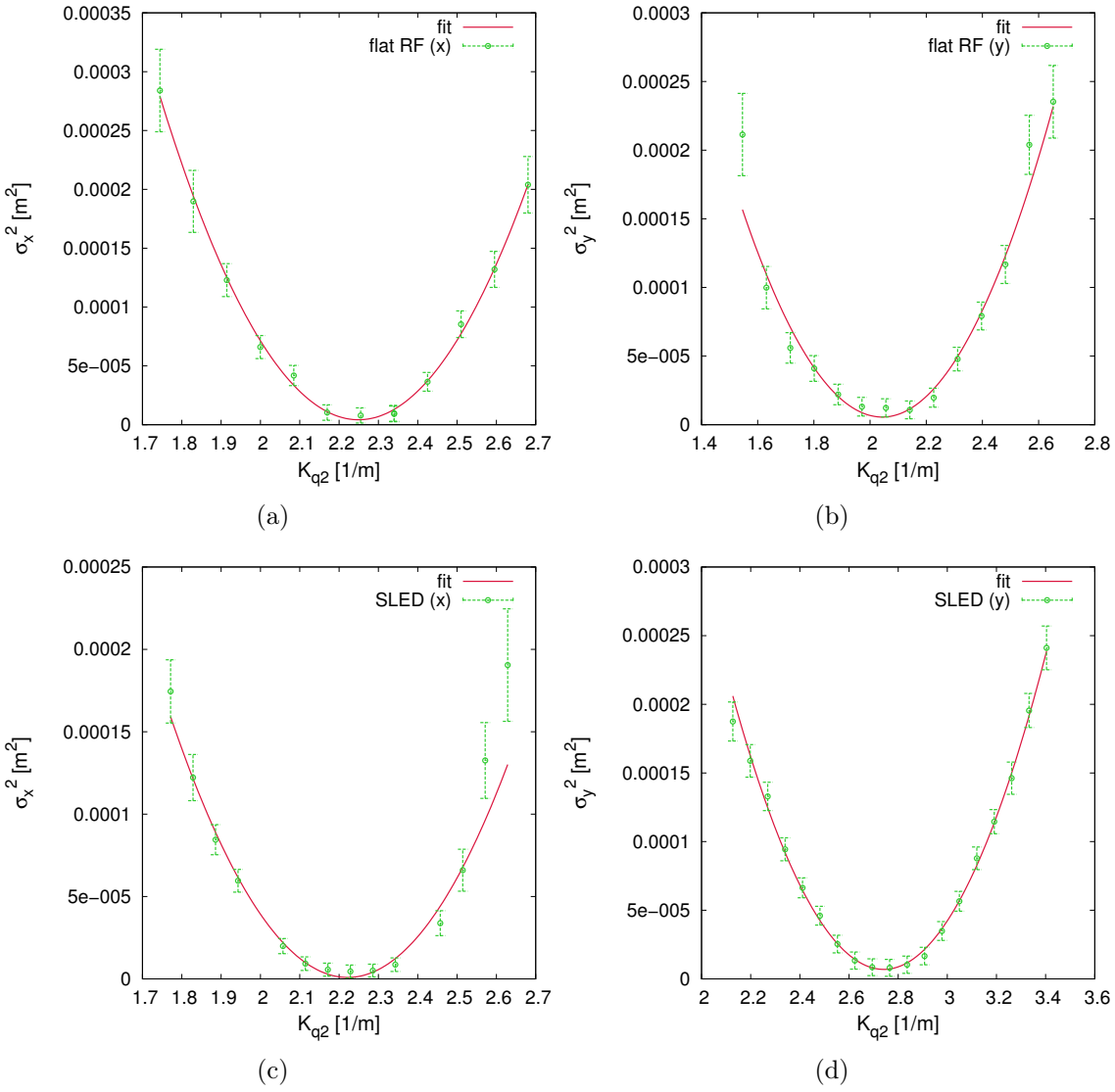

Figure 6.10: Parabola fit to quadrupole scan data with Y2Q1.5 at screen 1. Scans are shown for flat rf pulse in (a) and (b) and SLED pulse in (c) and (d) respectively.

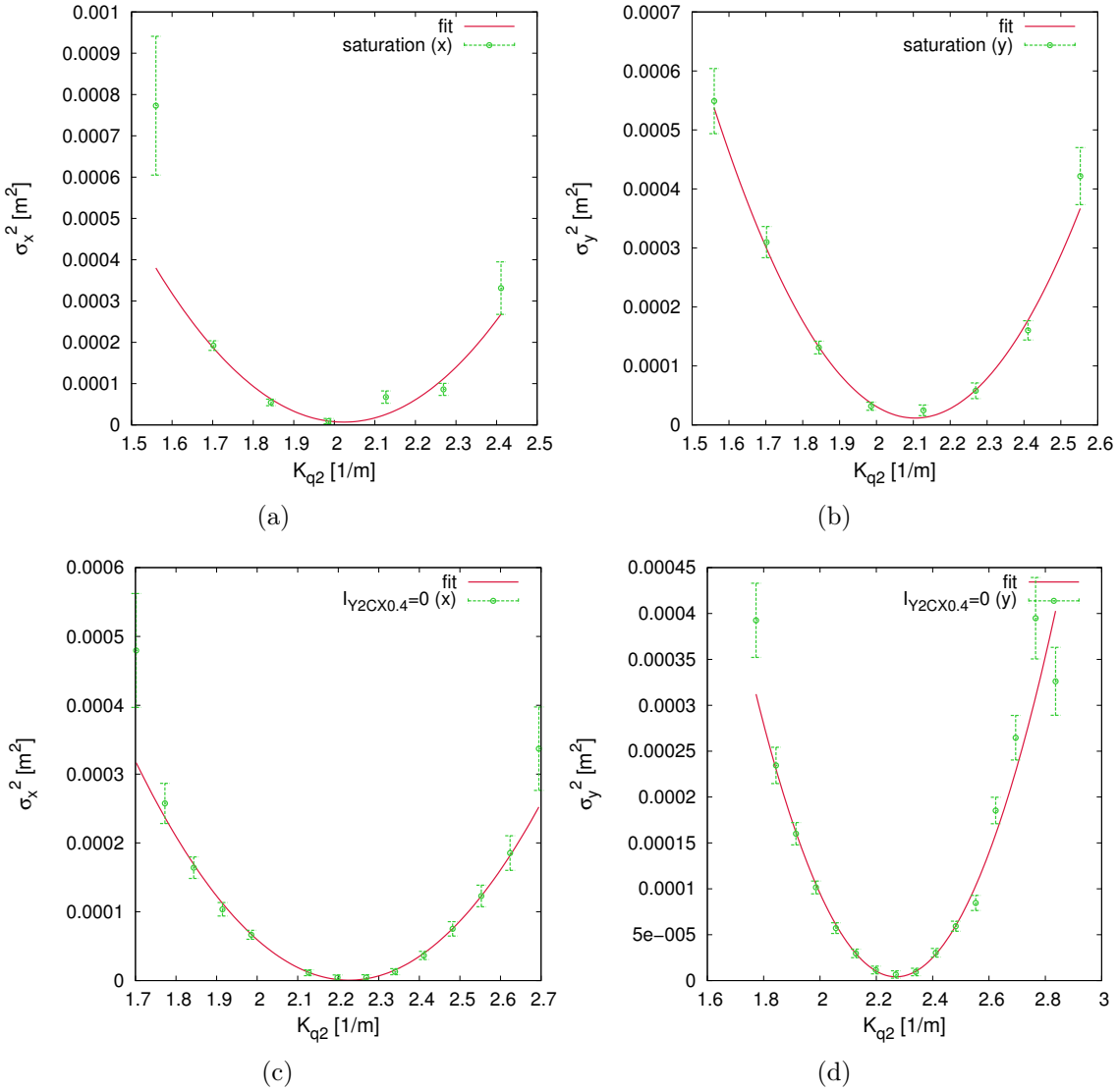

Figure 6.11: Parabola fit to quadrupole scan data with Y2Q1.5 at screen 1. Scans are shown for saturated beam loading effect in (a) and (b) and steerer Y2CX0.4 switched off in (c) and (d) respectively.

beam parameter	hor. (flat rf)	ver. (flat rf)	hor. (SLED)	ver. (SLED)
ϵ/μm	8.56	6.54	3.315	7.679
$\Delta\epsilon/\mu$m	1.68	2.87	3.436	0.676
α	-55.68	-41.06	-103.36	-34.73
$\Delta\alpha$	11.057	18.24	107.33	3.11
β/m	15.98	12.53	29.90	8.73
$\Delta\beta$/m	3.174	5.56	31.05	0.79
σ/mm	11.70	9.05	9.96	8.19
$\Delta\sigma$/mm	3.27	5.65	14.61	1.03
L/m	0.81	0.81	0.81	0.81
E_{kin}/MeV	3.8	3.8	4.8	4.8

Table 6.2: Quadrupole scan results for flat rf pulse and at higher energies using the SLED pulse.

horizontal and vertical plane are expected to be close. While this is true for the beam accelerated with the flat rf pulse, regarding the errors, the obtained parameters differ in the two planes for the beam accelerated with the SLED pulse. In the vertical plane the emittance is more than a factor of two higher, but with significantly lower relative error. Some causes for systematical error add to the given statistical errors and have been investigated with two further quadrupole scans. The first of these errors is caused by dispersion, which was assumed small enough to be neglected in the calculation.

Dispersion might be induced by misaligned solenoids, the steerer coil Y2CX0.4, the slightly rotated prebuncher (vertical plane) and the earth magnetic field. Behind the buncher, misalignment of the quadrupoles and another steering coil can cause dispersion. The earth magnetic field and the horizontal steerer would mainly cause an ϵ_x rising, but no significantly higher ϵ_x was measured. Anyway another scan with the steerer magnet current $I_{\mathrm{Y2CX0.4}} = 0\,\mathrm{A}$ was carried out.

An impact is expected notable because the steerer is located directly behind the prebuncher, where the energy distribution is widened. Thus its deflection adds some dispersion, which was neglected in the calculation. At the used current of 3 A it has an integrated field of $23 \cdot 10^{-6}\,\mathrm{Tm}$ according to the data in [70]. Additionally a scan was done using images of long and short pulses subtracted from each other as shown above. This does not affect one particular plane, but is supposed to reduce chromaticity effects. When the transient accelerating voltage due to beam loading can not be held constant, the resulting wide energy range of the beam causes different focal length for the higher energy front and the lower energy rear of the beam pulse. This effect was approached by partial suppression using the scan with two different pulse lengths and the optics calculated with the respective beam spot

images subtracted from each other. That way only the rear part of the pulse with lower multi-bunch energy spread is regarded.

beam parameter	hor. ($I_{\mathrm{Y2CX0.4}} = 0$)	ver. ($I_{\mathrm{Y2CX0.4}} = 0$)	hor. (sat.)	ver. (sat.)
ϵ/μm	3.92	9.05	13.86	18.23
$\Delta\epsilon/\mu$m	3.97	3.01	12.16	4.35
α	-127.92	-61.13	-51.91	-41.16
$\Delta\alpha$	129.72	20.54	46.34	10.09
β/m	36.95	17.44	15.93	12.32
$\Delta\beta$/m	37.47	5.86	14.22	3.02
σ/mm	12.03	12.57	14.86	14.99
$\Delta\sigma$/mm	17.25	5.94	18.61	5.13
L/m	0.81	0.81	0.81	0.81
E_{kin}/MeV	3.8	3.8	3.8	3.8

Table 6.3: Quadrupole scan results for flat rf pulse with steerer Y2CX0.4 switched off and with saturated beam loading effect respectively.

The results can be seen in figure 6.11 and table 6.3. For both measurements higher emittances have been observed in the vertical plane with relatively small $\Delta\epsilon$.
For a comparison of the emittance with the results from the simulation, the normalized emittance can be calculated using equation (3.19). From the given kinetic energies the Lorentz factor $\gamma = E_{\mathrm{kin}}/E_0 + 1$ and $\beta = v/c$ can be obtained. The Lorentz factor γ is 10.4 for the scan when the SLED pulse is used and 8.4 for the three other scans and β reaches 0.995 and 0.993 respectively.
Even the lowest values of $\epsilon_{\mathrm{n,x}} = 32.9\,\mu$m for the scan with the steerer switched off and $\epsilon_{\mathrm{n,x}} = 34.3\,\mu$m in case of using the SLED pulse are slightly higher than the values of $20\,\mu$m obtained in simulations. The higher values range to $\epsilon_{\mathrm{n,y}} = 79.4\,\mu$m for the SLED pulse setting and above $150\,\mu$m for the setting with beam loading close to saturation. For the latter, few data points were feasible and a low accuracy must be assumed. In case of the other settings, these high ϵ_n values are definitely influenced by the high energy spread, which increases the measured values above the actual normalized emittance.
Even though transmission has been optimized before the scan, the parameter set of the beam when arriving at the first quadrupole is of interest. At that position the beam is beeing focused for the first time after leaving the buncher structure. Because of beam defocusing in one plane (normally horizontal), the rms beam size must be significantly below the inner radius of the vacuum chamber of 16 mm in order to avoid beam loss. Since the calculated beam parameters represent the situation at the second quadrupole Y2Q1.5 behind the buncher structure, a calculation of the the beam size by means of the matrix formalism for beam optics has been carried out. Using equation (3.24) the values shown in table 6.4 have been obtained.

Except for $\sigma_x = 4.52\,\mathrm{mm}$ for the flat rf pulse, the beam hardly fits into the vacuum chamber and reduced transmission is likely. This observation stands in agreement with the beam loss between the buncher and dipole magnet, discussed in section 6.1. However, all calculated values are influenced by chromaticity. Even for the optics of the subtracted images, no lower beam size resulted. Chromaticity can not be excluded even in this measurement, because saturation of the acceleration voltage is not complete after 30 ns and the single bunch energy spread remains. Additionally the obtained errors for beam parameters in this more complex measurement were high.

scan condition	flat rf	SLED	$I_{\mathrm{Y2CX0.4}} = 0$	sat.
σ_x/mm	12.67	12.95	15.64	19.83
σ_y/mm	4.52	9.59	16.22	19.80

Table 6.4: Calculated rms beam size at the first quadrupole (Y2Q1.2) position for the four settings, for which quadrupole scans were carried out. These are a flat rf pulse, a compressed rf pulse, a flat rf pulse with a steerer switched off and a flat rf pulse using the rear part of the beam pulse, for which the beam loading influenced accelerating voltage saturates.

The optimization of the injection system must solve the problem of increased beam size. Furthermore misalignment is to be avoided. Re-installation of the system can take place outside of the Linac II tunnel, where access is generally possible. Hence more diligence during the alignment process is possible. A new water cooled solenoid and along with that a higher magnetic field, which reaches the design value of 0.08 T instead of 0.023 T, for focusing in the buncher structure in combination with reduced energy spread and hence lower chromaticity effects are going to allow higher transmission after the reconstruction of the injection system. The consequences of the test results for commissioning of the new injection system as electron source for the Linac II are discussed in the concluding chapter, which follows.

Chapter 7

Conclusion and outlook

The new injection system is ready for installation in the Linac II. In the following the achievements are briefly summarized and compared to the requirements. Furthermore necessary changes and remaining challenges are discussed.

7.1 Achievements

After optimization in detailed simulations, the new injection system has been fully constructed and commissioned in the Linac II tunnel. This was achieved despite the very lean maintenance schedule and unforeseen technical failures. Finally essential tests were successfully carried out in the short time remaining for test operation. They yielded the indispensable data about the beam and components of the new injection system, which were necessary to make final changes and verify that it suffices as electron source for the Linac II.

Eventually, beam current of up to 2.6 A can be delivered for injection in the main accelerator and operation without interruptions for time periods of several weeks are possible. Thus, longer breaks in operation due to failures of the bombarder gun will no longer be a risk for PETRA III experiments. Beam loading compensation shows promising results using a feed forward at detuned SLED cavity. In the future, the prebuncher rf will be coupled out at the buncher's input coupling cell. Thereby, beam loading compensation using the SLED pulse will be less critical. The problem of presently low transmission behind the buncher structure has been revealed. The loss also occurs in the dispersion free part of the injection system and is caused by an insufficiently focused beam. The new water cooled solenoid offers a 0.08 T field, instead of the max. 0.023 T during tests, and will reduce the beam size of the bunched beam. Achieving both objectives during further tests after installation is realistic.

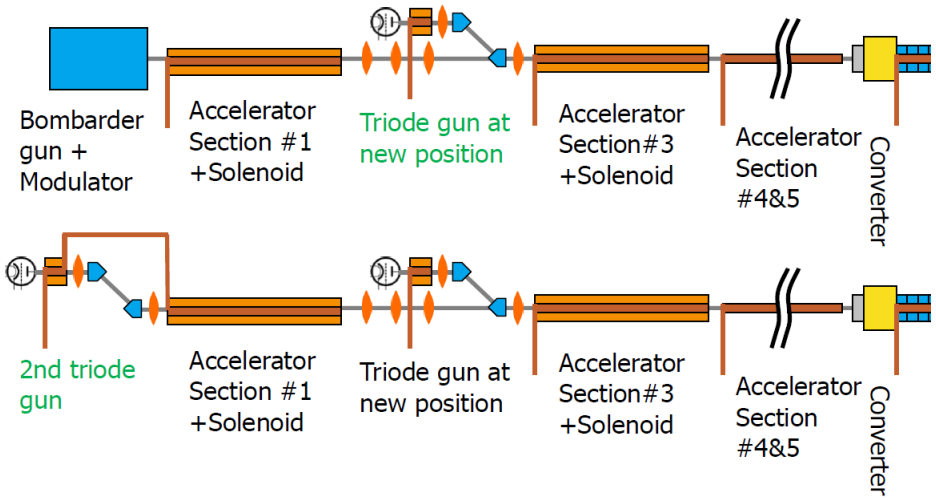

Figure 7.1: Overview of plans to replace section #2 and long-term replacement of the bombarder gun with a second triode gun injection system.

7.2 Alternative section #2 replacement

Despite the promising outlook, the loss behind the buncher structure poses a risk. The requirement to keep the performance of the bombarder gun injection system may at first not be met, if the new solenoid coil does not yield the desired beam size reduction. Another test operation period is not possible, because another shut down long enough to upgrade the Linac II injection system is not planned in the near future. Therefore, the plans for installation of the new injection system have been modified. The new layout is a compromise for which the replacement of accelerator section #2 instead of section #1 is intended. That way, the installation of the second buncher structure for the bombarder gun can be omitted and, as before, the prebunched beam will be injected directly into section #1. The long term replacement of the bombarder gun would be realized as drawn in figure 7.1. In the upper diagram the linac is presented with section #2 replaced by the triode gun injection system and the lower plot shows a future (2017+) design with another triode gun injection system, including a buncher structure and a magnetic chicane, which replaces the bombarder gun and its modulator. It must be noted that for the latter, again operation of a buncher and an accelerator section with one rf station is required. As discussed in section 3.2.2, for such a setup beam loading compensation with a SLED pulse is not feasible and a feed forward must be used as an alternative. Aside from avoiding the risk of lower bombarder gun performance, the replacement of accelerator section #2 has some disadvantages, but also relevant advantages. They are briefly discussed as follows and refer to the medium-term setup, in which the bombarder gun remains:

- In front of section #3, a necessary vacuum valve is placed instead of the vacuum chamber with a ceramic gap for use of an inductive current monitor. In order to not dismiss the current monitoring in front of the accelerator section, its distance to the dipole Y1D2.8 has to be extended by 16 cm for the additional chamber. This modification is included in the ongoing optimization of the beam line below, which was necessary in any case.

- Lower final energy in the primary linac must be tolerated for the triode gun system.

- Bunching without a proper capture cell, i.e. correct phase velocity in the first cell for the beam from the bombarder gun remains a problem.

- The solenoid of section #2 must be removed with the structure and quadrupole magnets will be used to focus. Due to defocusing in one plane, compensation of beam loading in section #1 becomes more important because of chromaticity aspects.

+ The total number of accelerator structures is not raised, hence the full SLED pulse is available for compensation of beam loading when the triode gun delivers beam. With the buncher driven by an rf station independently of the adjacent accelerator structure and the prebuncher rf coupled out at the first buncher coupling cell, full flexibility is granted to further attempts of beam loading compensation.

+ Diagnostics behind section #1 offer the possibility of beam profile and optical beam parameter analysis via quadrupole scans.

+ Attempt of loss less transmission through section #3-5 by variable focusing and steering options.

Some further points are to be considered, i.e. beam optics at the section #2 location must be optimized with additional quadrupole magnets, since electrons of significantly higher energy are to be focused. Constraints other than the field gradient of the magnets, which have a 1.6 T/m limit, are the fixed positions of Y1Q3.5/3.8. A minimum drift space of 1.1 m in front of Y1Q3.5/3.8, due to the junction with the beam line above, and reasonable choice of locations for diagnostics must be considered likewise. The development of the beta function for possible beam optics that satisfies the mentioned constraints, is shown in figure 7.2. The starting point is taken from ASTRA simulations for a single bunch. In order to achieve the necessary integrated field, pairs of quadrupoles will be placed where a single magnet designed for higher energy would have been sufficient.

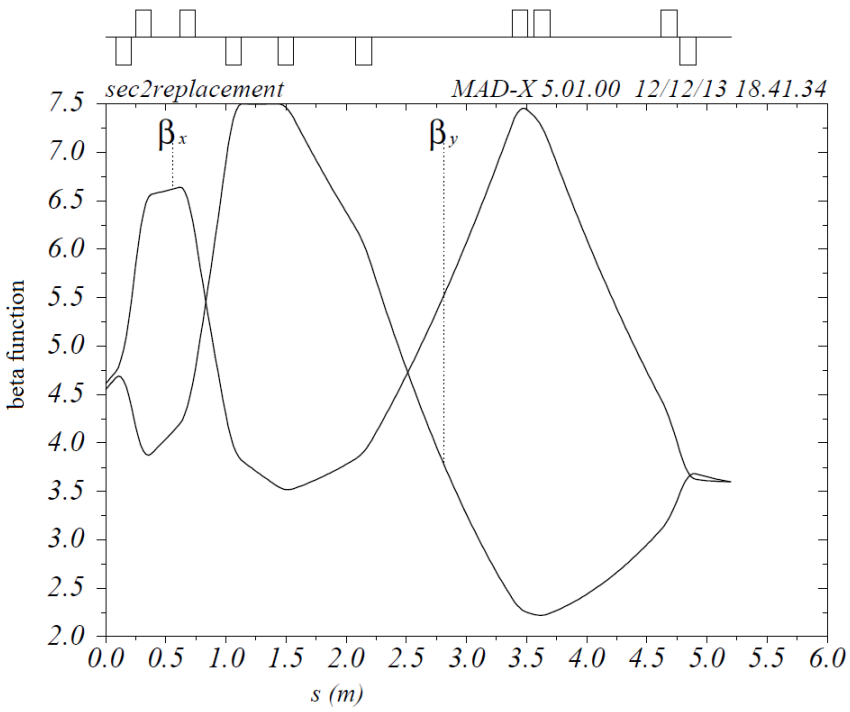

Figure 7.2: Twiss parameter optimization with MADX for replacement of section #2.

In addition the use of the screens at beam power and electron energies such as behind section #1 was not foreseen. The durability of the fluorescent coating will be affected and different reflection, emerging transmission and positron generation must be considered in charge measurement by the screen's Faraday cup.

7.3 Remaining challenges

In the ongoing Linac II shutdown from March 2014, the test stand is upgraded with the second beam line, the new buncher solenoid coil, a wall-current monitor in front of the buncher and an additional quadrupole magnet in the magnetic chicane. The linac's section #2 is replaced by the new injection system. The remaining time of the shutdown is used for commissioning. The main task is to compensate beam loading in the buncher structure using the SLED pulse or a feed forward. In case of bombarder gun operation transmission and injection into section #3 must be optimized. The ten available quadrupole magnets and three steering coils for each plane in the lower beam line offer the necessary flexibility and diagnostics allows specific adaption of beam properties. In the long term, the bombarder gun must be taken out of service once the triode gun system has proven reliable in Linac II operation in order to eliminate the risk of soiling the vacuum system with oil due to damage in the isolating ceramic.

Appendix A

Bombarder gun beam line

A.1 MAD-X result for section #2 replacement

Table A.1 shows the quadrupole positions and strengths for the bombarder gun beam line at the location of accelerator section #2 after its removal. The effective length of the quadrupole magnets is 11.9 cm.

Magnet	position z/m	$k/(1/\mathrm{m}^2)$
1	0.215	-6.899
2	0.38	7.177
3	0.75	5.548
4	1.13	-5.512
5	1.57	-1.387
6	2.21	-1.399
7	3.51	2.645
8	3.70	1.306
9	4.75	2.072
10	4.91	-4.294

Table A.1: Quadrupole strength and positions for $\beta(s)$ optimization in figure 7.2.

A.2 Injection system

A drawing of the unchanged injection system is presented in figure A.1.

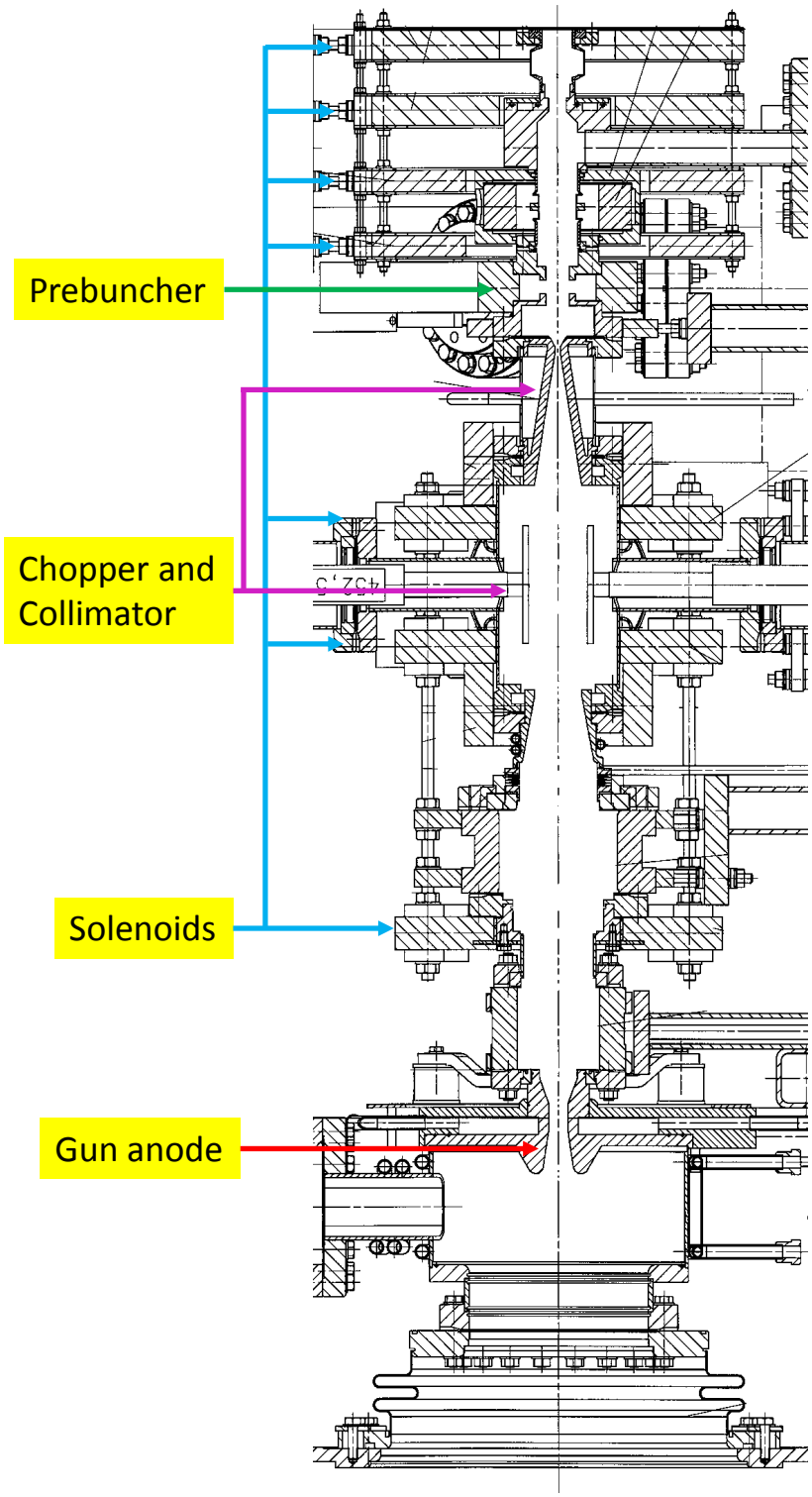

Figure A.1: Drawing of the bombarder gun injections system at the Linac II.

Appendix B

Evaluation of the beam current measurement at the Faraday cup

B.1 Deconvolution Mathematica code

The Mathematica code used to deconvolve the measured beam spectrum from the size of the fluorescent screen is quoted in the following:

```
filestring="spektrum.dat";

st = -15;
en = 15;
de = 0.02;

c = 2.998*10^8;
e0 = 0.5109989;

p[ekin_] := (((ekin + e0)^2 - e0^2)^0.5)
ekin[p_] := (e0^2 + p^2)^0.5 - e0

dat = Import[filestring][[All, 1 ;; 2]];

dat = Append[dat,{dat[[-1, 1]] + 0.1, 0}]; (*Append zeros for interpolation*)
dat = Append[dat,{dat[[-1, 1]] + 0.1, 0}];
dat = Prepend[dat,{dat[[1, 1]] - 0.1, 0}];
dat = Prepend[dat,{dat[[1, 1]] - 0.1, 0}];

specint = Interpolation[dat, InterpolationOrder -> 1]
```

```
scrinterv[pl_] := {
   {-15, 0},
   {p[5.0 - 0.176]/p[5.0]*pl - pl - pl/1000, 0},
   {p[5.0 - 0.176]/p[5.0]*pl - pl, 1}, {p[5.186]/p[5.0]*pl - pl, 1},
   {p[5.186]/p[5.0]*pl - pl + pl/1000, 0},
   {15, 0}
   };

newspec = Table[{(i - 1)*de + st, %[[i]]}, {i, 1, Length[%]}];
ListLinePlot[{%, dat}, PlotRange -> {{2, 8}, All}]

n = (en - st)/de + 1
istart = (1 - st)/de + 1

methods = {"DampedLS", "Wiener", "TotalVariation", "RichardsonLucy"};
methi = 2;

spec = {};
For[i = 1, i < (en - st)/de + 1, i++,
  scrcont =
   Interpolation[scrinterv[st + (i - 1)*de], InterpolationOrder -> 0];
  testscr = Table[scrcont[i]*de, {i, st, en, de}];
  testspec = Table[specint[ekin[i]], {i, st, en, de}];
  decon =
   ListDeconvolve[testscr, testspec, Method -> {methods[[methi]]}];
  spec = Append[spec, decon[[i]]]
  ];


ListLinePlot[%, PlotRange -> All]

newspec = Table[{ekin[(i - 1)*de + st], spec[[i]]}, {i, 1, Length[spec]}];

plotvgl = ListLinePlot[{newspec, dat}, PlotRange -> {{2, 8}, All}]
```

B.2 Scattered electrons on the screens in EGS5

For electrons of various energies incident on the fluorescent screens, simulations using the EGS5 code have been carried out. For simplicity a copper plate of 1.5 cm thickness was assumed and electrons hitting it under an angel of 45°. The results

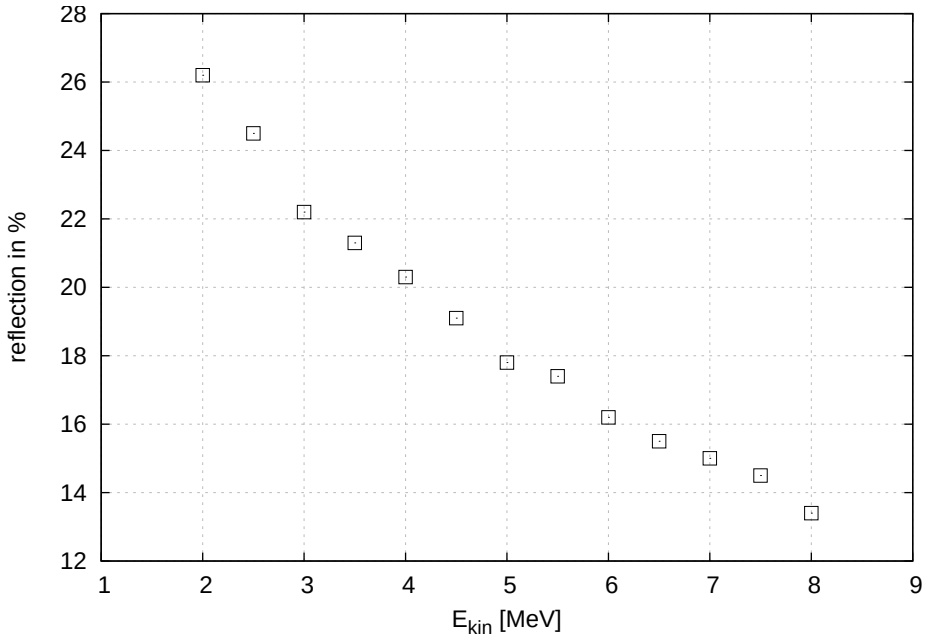

Figure B.1: Energy dependent electron beam reflection on copper resulting from EGS simulations.

are presented in figure B.1. An exact analysis of the incident Linac II beam by simulations would be non-trivial. In operation a calibration by means of the inductive current monitors is reasonable.

List of Figures

List of Tables

Abbreviations

ADC	Analog-to-digital converter
ASTRA	A Space Charge Tracking Algorithm
BPM	Beam position monitor
CST	Computer Simulation Technology
cw	Continuous wave
DC	Direct current
DESY	Deutsches Elektronen-Synchrotron
DORIS	Doppel Ring Speicher
EGS	Electron-Gamma Shower
ERL	Energy recovery linac
FEL	Free-electron laser
FLASH	Freie-Elektronen-Laser in Hamburg
FWHM	Full width at half maximum
HERA	Hadron Elektron Ring Anlage
linac	Linear Accelerator
MAD	Methodical Accelerator Design
NWA	Network analyzer
PCB	Printed circuit board
PETRA	Positron Elektron Tandem Ring Anlage

PIA	Positronen Intensitäts Akkumulator
PWA	Plasma wakefield acceleration
rf	Radio frequency
rms	root mean square
SBTF	S-Band Test Facility
SLAC	Stanford Linear Accelerator Center
SLED	SLAC Energy Doubler
TWS	Traveling Wave Structure
UHV	Ultra-high vacuum
XFEL	European X-ray free electron laser
YAG	Yttrium aluminium garnet

Bibliography

[1] A. Febel et al. *General description and performance measurements on DESY Linac II electron-positron injector*. Proceedings of PAC 1971.

[2] A. Febel, G. Hemmie. *PIA, the positron intensity accumulator for the PETRA injection*. IEEE Transactions on Nuclear Science, Vol. NS-26, No. 3, June 1979.

[3] W. Ebeling et al. *The radiofrequency-system for PIA*. IEEE Transactions on Nuclear Science, Vol. NS-28, No. 3, June 1981.

[4] M. Hüning, R. Jonas, J. Lund-Nielsen, F. Schmidt-Föhre. *A resonant first turn BPM for the positron intensity accumulator (PIA) at DESY*. Proceedings of DIPAC 2009.

[5] G. Fuhs. *Measurements on the electronbeam optic at the Electron-Positron storage ring PIA*. Bachelor thesis, Universität Hamburg, 2012.

[6] `http://www.desy.de`.

[7] K. Balewski. *Commissioning of PETRA III*. Proceedings of IPAC 2010.

[8] K. Balewski. *PETRA III upgrade*. Proceedings of IPAC 2011.

[9] K. Wille. *Physik der Teilchenbeschleuniger und Synchrotronstrahlungsquellen*. Teubner Verlag, 2. Auflage, 1996.

[10] A. Hofmann. *Characteristics of synchrotron radiation*. Proceedings of CERN accelerator school (CAS), 1990.

[11] M. Hüning, M. Schmitz. *Recent changes to the e+/e- injector (Linac II) at DESY*. Proceedings of LINAC 2008.

[12] BKR-Wiki (internal): `http://bkr-wiki.desy.de/`.

[13] J. D. Jackson. *Classical Electrodynamics*. Wiley, 3rd edition, 1998.

[14] T. O. Wangler. *RF Linear Accelerators*. Wiley-vch, 2008.

[15] Z. D. Farkas et al. *SLED: A Method of Doubling SLAC's Energy*. SLAC-PUB-145, 1974.

[16] H. Wiedemann. *Particle Accelerator Physics*. Springer, 3rd edition, 2007.

[17] M. Hüning. *Running the Linac II Structures*. DESY, 2005.

[18] C. D. Nantista. *Radio-Frequency Pulse Compression for Linear Accelerators*. SLAC, 1995.

[19] R. Bossart, P. Brown, J. Mourier, I.V. Syratchev, L. Tanner. *High-power microwave pulse compression of klystrons by phase-modulation of high-Q storage cavities*. CLIC-Note-592, CERN, 2004.

[20] S. H. Shaker, R. Corsini, P. K. Skowronski, I. Syratchev, F. Tecker. *Phase modulator programming to get flat pulses with desired length and power from the CTF3 pulse compressors*. Proceedings of IPAC 2010.

[21] J. W. Wang. *Rf properties of periodic accelerating structures for linear colliders*. SLAC – 339, UC – 28, (A)Stanford University, 1989.

[22] M. Minty. *HERA performance upgrade: Achievements and plans for the future*. Proceedings of EPAC 2004.

[23] C. Diaconu et al. *Physics Accomplishments of HERA*. Annu. Rev. Nucl. Part. Sci. 2010. 60:101–28.

[24] K. Balewski et al. *PETRA III: A Low Emittance Synchrotron Radiation Source*. Technical design report, 2004.

[25] *PETRA III extension project; Beamlines P64 / P65 for X-ray absorption spectroscopy*. Technical design report, 2012.

[26] Y-796 Activation Schedule. Eimac, United Kingdom, 1986.

[27] The OLYMPUS collaboration. *Technical design report for the OLYMPUS experiment*. 2010.

[28] R. Wanzenberg. *Observations of electron cloud phenomena at PETRA III*. Proceedings of ECLOUD 2012.

[29] G. Xia et al. *Ion effect issues in PETRA III*. Proceedings of PAC 2009.

[30] V. Shiltsev. *Colliders - "Quo vadis?": Past 20 years, next 20 years, and beyond*. Proceedings of PAC 2013.

[31] MAD-X user's guide. CERN, 2002.

[32] K. Flöttmann. *A Space Charge Tracking Algorithm*. ASTRA Manual, Version 3.0, 2014.

[33] R. Brinkmann et al. *Conceptual Design Report of a 500 GeV e+e- Linear Collider with Integrated X-ray Laser Facility*. DESY 1997-048.

[34] M. Schmitz. *The S-Band linear collider test facility at DESY*. Proceedings of PAC 1997.

[35] M. Schmitz. *Performance of the first part of the injector for the S-Band test facility at DESY*. Proc. of LINAC 1996.

[36] M. Schmitz. *First tests at injector for the S-Band test facility at DESY*. Proceedings of PAC 1995.

[37] F. Klarner. *Konzeption, Aufbau und Inbetriebnahme eines neuen Vorbeschleunigersystems an ELSA*. Dissertation, Rheinische Friedrich-Wilhelms-Universität Bonn, 2011.

[38] I. Langmuir. *The Effect of Space Charge and Residual Gases on Thermionic Currents in High Vacuum*. Phys. Rev. 2, 450, 1913.

[39] H. Barkhausen. *Lehrbuch der Elektronenröhren*. 1. Band, 8. Auflage, S. Hirzel Verlag Leipzig, 1950.

[40] B. Anderberg et al. *The design of a 3GHz thermionic RF-gun and energy filter for MAX-lab*. Nuclear Instruments and Methods in Physics Research A 491 (2002) 307–313, 2002.

[41] B. Anderberg et al. *A new 3 GHz rf-gun structure for MAX-lab*. Proceedings of EPAC 2000.

[42] G. Blokesch. *e-Source2, LINAC-2, DESY Hamburg - Measurement protocols*. Puls-Plasmatechnik GmbH, 2011.

[43] G. Blokesch. *e-Source2 Manual*. Puls-Plasmatechnik GmbH, 2012.

[44] M. Peiniger, C. Piel, H. Vogel, P. vom Stein. *A 100 MeV injector linac for the Swiss Light Source supplied by industry.* ACCEL Instruments, Proceedings of PAC 1999.

[45] C. Christou, V. Kempson, K. Dunkel, C. Piel. *The pre-injector linac for the Diamond Light Source.* Proceedings of LINAC 2004.

[46] K. Whitham et al. *Design of the e+/e- Frascati linear accelerator for Dafne.* Proceedings of PAC 1993.

[47] S. Lederer et al. *Photocathodes at FLASH.* Proceedings of FEL 2011.

[48] I. V. Bazarov et al. *Thermal emittance and response time measurements of negative electron affinity photocathodes.* Cornell University, J. Appl. Phys. 103, 054901 (2008).

[49] M. Hüning, C. Liebig, M. Schmitz. *An electron linac injector with a hybrid buncher structure.* Proceedings of LINAC 2010.

[50] S. Pei, O. Xiao. *Studies on an S-band bunching system with hybrid buncher.* Proceedings of IPAC 2013.

[51] D. Alesini et al. *The design of a hybrid photoinjector for high brightness beam applications.* Proceedings of EPAC 2006.

[52] Bergoz Instrumentation, France: `http://www.bergoz.com/`

[53] Fischer Custom Communications, Inc.: `http://www.fischercc.com`.

[54] CST Computer Simulation Technology AG: `http://www.cst.com`.

[55] J. H. Billen. *Poisson Superfish.* Poisson Superfish Documentation, LANL, 2006.

[56] K. Flöttmann. *Some basic features of the beam emittance.* Physical review special topics - Accerlerators and beams, Volume 6, 2003.

[57] H. Hirayama, Y. Namito, A.F. Bielajew, S.J. Wilderman, W.R. Nelson. *The EGS5 Code System.* KEK Report 2005-8 (2005).

[58] B. E. O'Rourke et al. *Simulations of slow positron production using a low energy electron accelerator.* Rev. Sci. Instrum. 82, 063302 (2011).

[59] A. Mikhailichenko. *CESR's positron source.* SLAC LC02, 2002.

[60] Y. Nie, C. Liebig, M. Hüning, M. Schmitz. *Tuning of 2.998 GHz S-band hybrid buncher for injector upgrade of LINAC II at DESY*. Nuclear Instruments and Methods in Physics Research A 761 (2014) 69–78.

[61] Charles W. Steele. *A nonresonant perturbation theory*. IEEE Transactions on Microwave Theory and Techniques, Vol. MTT 14, No. 2, 1966.

[62] T. Khabiboulline et al. *A new Tuning Method for Traveling Wave Structures*. Proceedings of PAC 1995.

[63] J. Shi et al. *Tuning of X-band traveling-wave accelerating structures*. Nuclear Instruments and Methods in Physics Research A, CERN, 2012.

[64] T. Khabiboulline et al. *Tuning of a 50-cell constant gradient S-band traveling wave accelerating structure by using a nonresonant perturbation method*. Internal report, DESY M-95-02, 1995.

[65] K. Flöttmann, H. Delsim-Hashemi. DESY, private communication, 2013.

[66] D. Lipka et al. *Dark current monitor for the European XFEL*. Proceedings of DIPAC 2011

[67] Proceedings of CERN accelerator school (CAS), 2008.

[68] Wolfram Mathematica 9 Documentation Center: `http://reference.wolfram.com`.

[69] P. Forck. *Lecture Notes on Beam Instrumentation and Diagnostics*. Joint University Accelerator School 2011

[70] K. Flöttmann. *Design and Performance of printed circuit steering Magnets for the FLASH Injector*. Proceedings of IPAC 2010.

Danksagung

An dieser Stelle möchte ich mich bei allen bedanken, die zum Erfolg dieser Arbeit beigetragen haben und ohne deren Hilfe ihre Durchführung kaum möglich gewesen wäre.
Als erstes danke ich Jörg Roßbach, der sich bereit erklärte die Betreuung der Arbeit zu übernehmen. Seine direkte Art und Neugier habe ich als sehr förderlich empfunden, ebenso wie die offenen Diskussionen in Seminaren.
Des Weiteren gilt mein Dank Markus Hüning, der als Gruppenleiter den größten Teil der fachlichen Unterstützung übernommen hat. Seine Hilfsbereitschaft und sein großer technischer Sachverstand erleichterten das Bewältigen vieler Herausforderungen erheblich.
Ich danke Hans Weise für das Vermitteln des Themas, zu dem ich meine Dissertation angefertigt habe. Über ihn konnte ich erste Kontakte zu DESY herstellen.
Ein großer Dank geht an die gesamte Linac II Mannschaft, die tatkräftig an der Umsetzung des Projekts mitgearbeitet hat. Meinen Dank schulde ich insbesondere Rolf Jonas für den Aufbau der HF-Technik, Yuancun Nie für die gute Zusammenarbeit beim Tuning und sein großes Interesse an meiner Arbeit, Ingo Peperkorn für die Unterstützung mit der Gunelektronik sowie bei vielen technischen Fragen, Horst Poggensee für Konstruktion und Montage des Teststands und Michael Schmitz für die vielen aufschlussreichen Diskussionen.
Weitere Kollegen, denen ich für ihre Unterstützung danken möchte sind Michael Seebach für die Hilfe mit Archiv und Kontrollsystem, Frank Schmidt-Föhre, Silke Vilcins-Czvitkovits und Jorgen Lund-Nielsen für die Bereitstellung der BPMs und Reinhard Neumann und Norbert Wentowski für die Unterstützung bezüglich der Strommonitore. Rolf Zahn und Alfred Affeldt sei gedankt für die Infrastruktur der Schirmmonitore und Klaus Flöttmann danke ich für seinen Rat bezüglich der Schirmmonitore, Astra und EGS.
Für die Möglichkeit, als Operateur für FLASH zu arbeiten, danke ich Bart Faatz und Siegfried Schreiber.
Ich danke Felix Schlander, der sich neben dem Korrektur Lesen auch die Zeit genommen hat, als Fragesteller trotz der mit Abstand längsten Anfahrt an meiner Disputation teilzunehmen. Ebenfalls sei allen weiteren Korrekturlesern und Fragestellern herzlich gedankt.
Weitere Kollegen und Freunde, die sich auch nach Feierabend durch die Schaffung eines geselligen Umfelds verdient gemacht haben sind Sebastian Aderhold, Shima Bayesteh, Wolf Behrenhoff, Dirk Damann, Steffen Hauf, Timon Mehrling, Niladri Sen, Marc Wenskat und Claudia Zacholl.
Abschließend danke ich meinen Eltern Christiane und Siegfried Liebig für ihre anhaltende Unterstützung während des gesamten Studiums.